

GRANT NUMBER AFOSR- 88 0319

DTIC FILE COPY

②

MICROSTRUCTURE OF THIN FILMS

AD-A219 262

E. Pelletier
Ecole Nationale Supérieure de Physique de Marseille
Laboratoire d'Optique des Surfaces et des Couches Minces
Domaine Universitaire de St Jérôme
13397 Marseille Cedex 13, France

Tel: (33) 91 28 83 28

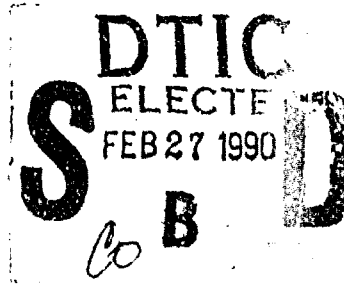
and

H.A. Macleod
Optical Sciences Center
University of Arizona
Tucson, AZ 85721, USA

Tel: (1) 602 621 2449

Final report: 30 September, 1988 - 30 September, 1989

Approved for public release;
distribution unlimited



Prepared for

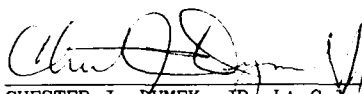
EUROPEAN OFFICE OF AEROSPACE RESEARCH AND DEVELOPMENT
223/231 Old Marylebone Road
London, NW1 5TH, UK


90 02 26 007

EOARD TR-90-03

This report has been reviewed and is releasable to the National Technical Information Service (NTIS). At NTIS it will be releasable to the general public, including foreign nations.

This technical report has been reviewed and is approved for publication.


CHESTER J. DYMEK, JR., Lt Col, USAF
Chief, Chemistry


FRED T. GILLIAM, Lt. Col, USAF
Chief Scientist

UNCLASSIFIED

SECURITY CLASSIFICATION OF THIS PAGE

REPORT DOCUMENTATION PAGE				Form Approved OMB No. 0704-0188	
1a. REPORT SECURITY CLASSIFICATION <u>Unclassified</u>			1b. RESTRICTIVE MARKINGS		
2a. SECURITY CLASSIFICATION AUTHORITY			3. DISTRIBUTION / AVAILABILITY OF REPORT Approved for public release; Distribution unlimited		
2b. DECLASSIFICATION / DOWNGRADING SCHEDULE					
4. PERFORMING ORGANIZATION REPORT NUMBER(S)			5. MONITORING ORGANIZATION REPORT NUMBER(S) EOARD TR-90-03		
6a. NAME OF PERFORMING ORGANIZATION <u>E. N. S. P. M.</u>		6b. OFFICE SYMBOL (If applicable)	7a. NAME OF MONITORING ORGANIZATION European Office of Aerospace Research and Development		
6c. ADDRESS (City, State, and ZIP Code) <u>Domaine Universitaire de St Jérôme 13397 Marseille Cedex 13 - France</u>			7b. ADDRESS (City, State, and ZIP Code) Box 14 FPO New York 09510-0200		
8a. NAME OF FUNDING / SPONSORING ORGANIZATION <u>European Office of Aerospace Research and Development</u>		8b. OFFICE SYMBOL (If applicable) LRC	9. PROCUREMENT INSTRUMENT IDENTIFICATION NUMBER AFOSR 88-0319		
8c. ADDRESS (City, State, and ZIP Code) Box 14 FPO New York 09510-0200			10. SOURCE OF FUNDING NUMBERS		
			PROGRAM ELEMENT NO. 61102F	PROJECT NO. 2301	TASK NO. D1
11. TITLE (Include Security Classification) <u>Microstructure of thin films</u>					
12. PERSONAL AUTHOR(S) <u>Dr. Emile Pelletier and Dr. H. A. Macleod.</u>					
13a. TYPE OF REPORT <u>Final Scientific</u>		13b. TIME COVERED FROM <u>30 Sept 88</u> TO <u>30 Sept 89</u>		14. DATE OF REPORT (Year, Month, Day) <u>7 February 1990</u>	
15. PAGE COUNT					
16. SUPPLEMENTARY NOTATION					
17. COSATI CODES			18. SUBJECT TERMS (Continue on reverse if necessary and identify by block number)		
FIELD	GROUP	SUB-GROUP	Optical Surface Scattering; Optical constants for TiO ₂ , Ta ₂ O ₅ , LaF ₃ , Al, Ag; Growth modeling; Optical surface measurements; Optical coatings;		
19. ABSTRACT (Continue on reverse if necessary and identify by block number)					
<p>A lot of work is devoted to the study of Ion Assisted deposition (IAD) with different materials: metals, Al, Ag, and dielectrics, nitrides, fluorides and oxides. Some additional results concern oxides produced by Ion Plating</p> <p>Concerning the photothermal deflection, which is used for measurement of absorption losses, the results of characterization obtained on the OSA samples of TiO₂ are given; instabilities versus time are observed when the samples are illuminated.</p> <p>The theory and experiments performed on scattering are applied to coatings of special designs produced by Balzers, OCLI, OJAI and Spectra Physics to determine the correlation between interfaces of the multilayers. These results which were presented at the OSA 1989 meeting in Florida are summarized here.</p>					
20. DISTRIBUTION / AVAILABILITY OF ABSTRACT <input type="checkbox"/> UNCLASSIFIED/UNLIMITED <input type="checkbox"/> SAME AS RPT. <input type="checkbox"/> DTIC USERS			21. ABSTRACT SECURITY CLASSIFICATION <u>Unclassified</u>		
22a. NAME OF RESPONSIBLE INDIVIDUAL <u>Chester J. Dymek</u>			22b. TELEPHONE (Include Area Code) <u>44 1 409 4505</u>		22c. OFFICE SYMBOL EOARD/LRC

DO Form 1473, JUN 86

Previous editions are obsolete.

SECURITY CLASSIFICATION OF THIS PAGE

UNCLASSIFIED

GRANT NUMBER AFOSR- 88 0319

MICROSTRUCTURE OF THIN FILMS

E. Pelletier
Ecole Nationale Supérieure de Physique de Marseille
Laboratoire d'Optique des Surfaces et des Couches Minces
Domaine Universitaire de St Jérôme
13397 Marseille Cedex 13, France

Tel: (33) 91 28 83 28

and

H.A. Macleod
Optical Sciences Center
University of Arizona
Tucson, AZ 85721, USA

Tel: (1) 602 621 2449

Final report: 30 September, 1988 - 30 September, 1989

Approved for public release;
distribution unlimited

Prepared for

EUROPEAN OFFICE OF AEROSPACE RESEARCH AND DEVELOPMENT
223/231 Old Marylebone Road
London, NW1 5TH, UK

Abstract

A lot of work is devoted to the study of Ion Assisted deposition (IAD) with different materials: metals, Al, Ag, and dielectrics, nitrides, fluorides and oxides.

Concerning oxides, a comparison between IAD and Ion Plating techniques is in progress.

For the characterization, we describe the two techniques used for determination of optical losses which are photothermal deflection and measurements of angular scattering distribution.

Concerning photothermal deflection, the results of characterization obtained on the OSA samples of TiO_2 are given; instabilities versus time are observed when the samples are illuminated.

The theory and experiments performed on scattering are applied to coatings of special designs produced by Balzers, OCLI, OJAI and Spectra Physics to determine the correlation between interfaces of the multilayers.

These results, which were presented at the OSA 1989 meeting in Florida are summarized here. This work leads indirectly to the measurement of the grain size of the materials in thin film form. A completely different approach is given by growth modeling, but it remains to link the two techniques for a better understanding of the process of growth.

DTIC
COPY
INSPECTED
5

Accession For	
NTIS GRA&I	<input checked="checked" type="checkbox"/>
DTIC TAB	<input type="checkbox"/>
Unannounced	<input type="checkbox"/>
Justification	
By	
Distribution/	
Availability Codes	
Dist	Avail and/or Special
A-1	

INTRODUCTION

For several years, and due to US Air Force grants, the two laboratories of Prof H.A. Macleod at the Optical Sciences Center - Tucson- and E. Pelletier at the Ecole Nationale Supérieure de Physique - Marseilles- have coordinated their work of research, playing in this way complementary roles.

The distance between Tucson and Marseilles brings obviously some difficulties because the number of meetings between the members of the two groups is necessarily limited. This year we should have waited for the end of the annual OSA meeting in Orlando (oct 89) to take stock of the situation for the works as part of the cooperative program and to draw the future prospects.

The present report shows first the evolution of the work in each of the two labs:

- the Tucson group is interested in the development of Ion Assisted Deposition (IAD) techniques, and more particularly for metals (Al, Ag) and dielectrics (nitrides, lanthanides trifluorides) interesting for their potential application to infrared optical components. The results obtained on IAD induced the group to deal with film growth modeling to understand in detail the growth mechanisms effectively involved.

- with a complementary but totally different approach, the group of Marseilles is also interested in this same problem.

In comparison with the Tucson group, we bring few results on the IAD technique because our activity is limited on the study of very classical materials such as TiO_2 , SiO_2 and Ta_2O_5 . However, in Marseilles, we began a comparative study of different deposition techniques since we have at our disposal a Balzers Ion Plating plant. To this we can add important attempts in the development of optical characterization techniques. Here we will deal particularly with two subjects that seem to be more prominent for this year and that are respectively

- measurement of absorption losses by photothermal technique

- and mainly, measurement of the scattering curve to look into the question of correlation between successive interfaces of a layer stack. On this last question, we will made a rapid evaluation of the progresses made and we will especially present the results obtained with the active cooperation of the OSA Technical Group of Thin Films led by J. Apfel (O.C.L.I.). We meet the concern of Tucson on the study of layer growth mechanism, where we will have to combine our efforts to progress.

ION ASSISTED DEPOSITION AND MODELING AT THE UNIVERSITY OF ARIZONA

Relevant work at the University of Arizona during the period of this contract has been supported by the USAF under the URI program. This has placed emphasis on the investigation of the use of ion-assisted deposition for modification of film structure and determining its utility for improving the performance in optical thin films. The materials studied by ion-assisted deposition has ranged over metals, especially silver and aluminum, and dielectrics, especially aluminum oxide, nitride and oxynitride and the fluorides of the lanthanide series. In modeling, some progress has been made with the Monte Carlo model of film growth. Much of the Arizona work reported here is also the subject of reports to the USAF from the URI-supported Center for Thin Film studies.

Ion-assisted deposition of metals

It was of interest to us to determine if the great benefits of io-assisted deposition in the fabrication of dielectric coatings would also be realised in the deposition of metals of high optical performance, such as silver and aluminum. The results were disappointing in that the optical properties were found to be degraded in the sense that the real part of refractive index rose with bombardment while the extinction coefficient fell. Typical results for silver are shown in figures 1 and 2. Note that the changes in the optical constants accompany increases in the implanted argon of the films. Broadly similar results were obtained for aluminum although the changes for very small bombardment were not as pronounced, figures 3 and 4, making it possible that very light bombardment might be acceptable for aluminum. Although the changes are not large, nevertheless they are in a negative sense. Similar changes were found in other aspects of film performance, the DC resistivity for example (which rose with bombardment). Implanted argon also correlated well with the other changes. The conclusion was that straightforward ion-assisted deposition was not as favorable a process for metal film deposition as it is for dielectrics.

The experiments up to this stage were all involving ion energies in the range 200 to 500 eV. Before leaving the question of metal films we thought that experiments using lower bombardment energies should be carried out. Furthermore, although the optical property changes appear disappointingly negative, there are aspects of ion-assisted deposition of metals that are useful, particularly the improvement in adhesion that affects both metals and dielectrics. The bombardment that takes place before and during the early stages of film growth is particularly effective in this respect. A series of experiments were therefore undertaken to investigate the use of lower energies in bombardment, 20 to 50 eV, and also the effect of limiting the bombardment to the growth of the first part of the films only.

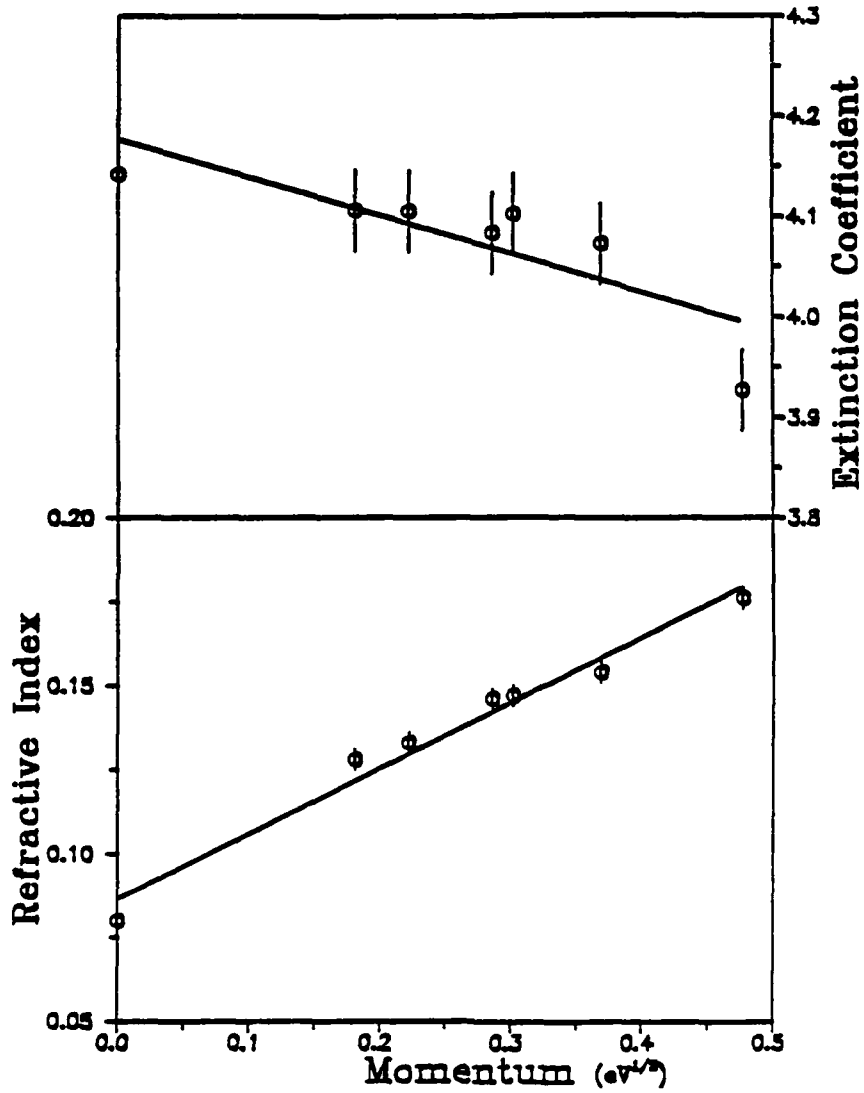


Figure 1

Variation of n and k at 632.8 nm of Ag films measured by the SPR as a function of P , where $P = \gamma \sqrt{E}$ and γ is the ratio of arrival rates of ions and evaporant atoms. (Hwangbo)

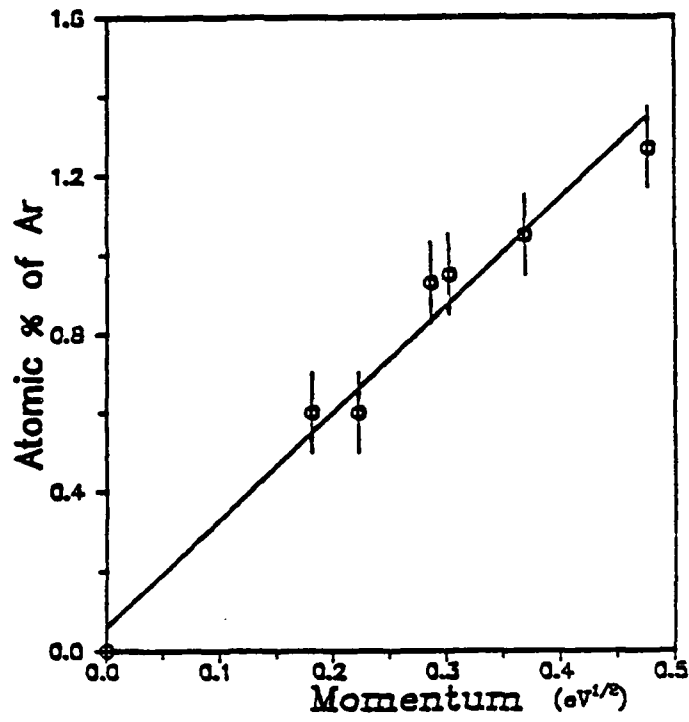


figure 2:

Ar concentration in Ag films as a function of P (Hwangbo)

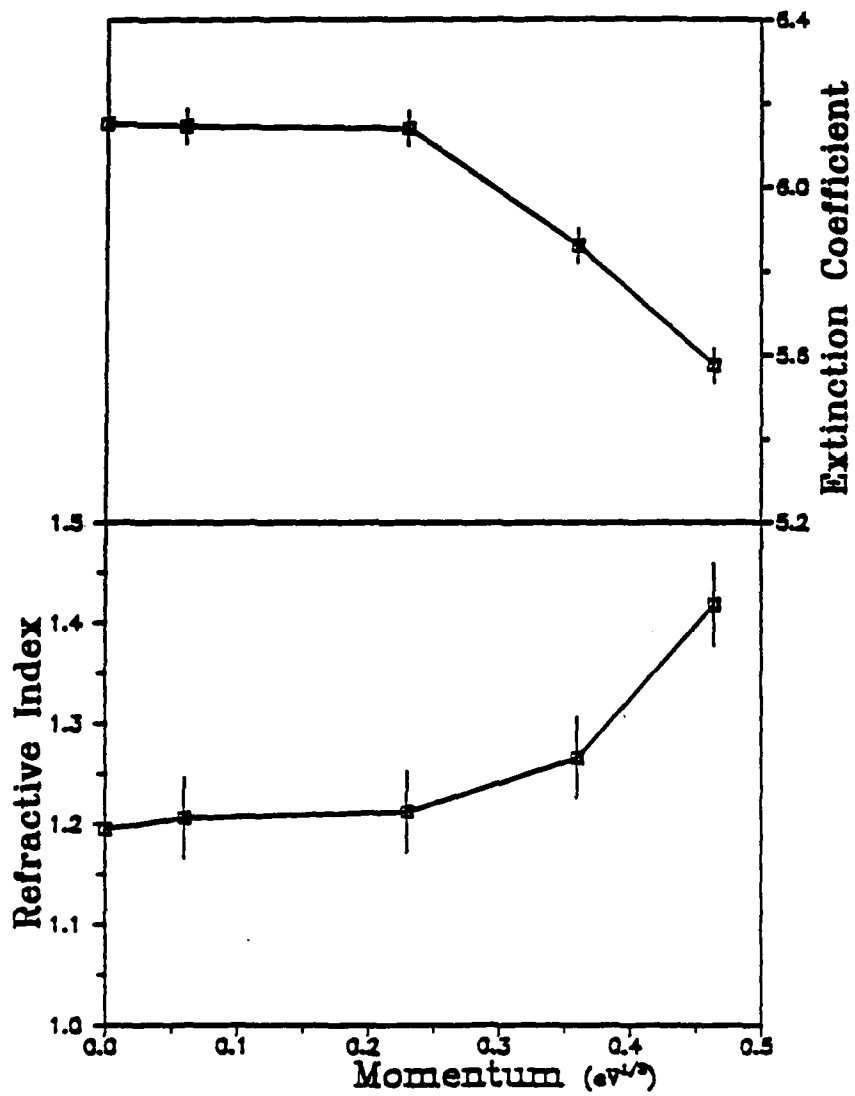


Figure 3:

Variation of n and k at 632.8 nm of Al films measured by the SPR as a function of P . (Hwangbo)

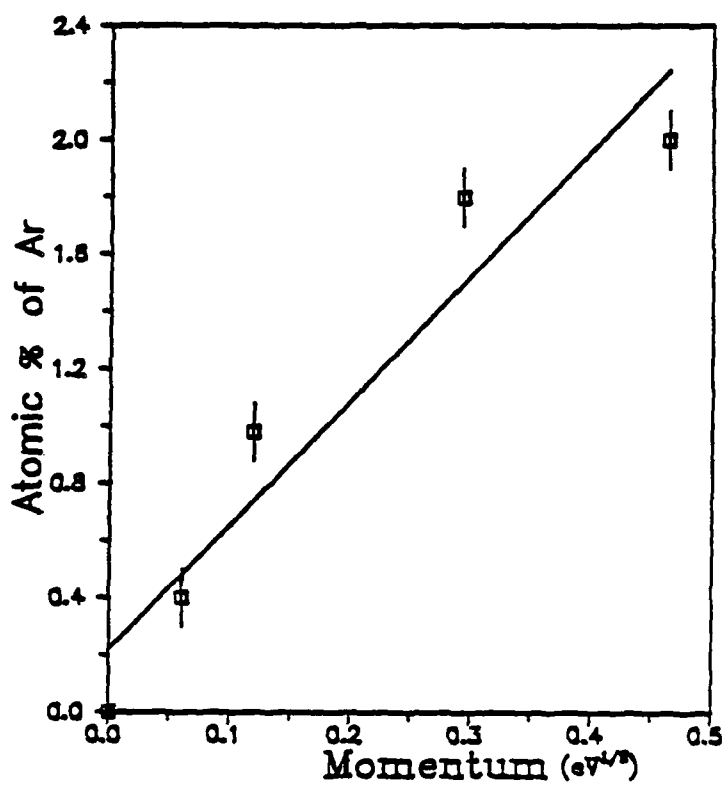


Figure 4:

Ar concentration in Al films as a function of P (Hwangbo)

Since we found, in the higher energy series of experiments, that the DC resistivity of the films was a good indicator of film quality, this was the measured parameter in this new series.

Results are shown in figure 5. All films had the same total thickness of 55 nm. The vertical scale is the measured resistivity of the films after deposition. The horizontal scale is the thickness of film that was subjected to bombardment after which the bombardment ceased and the remainder of the film was deposited without interruption by conventional evaporation without bombardment. The results were not very consistent, although the error bars calculated for the experiment (shown against only one set of results for clarity) were very much less than the variations exhibited. Zero bombardment gave consistently the value of resistivity that had been established before. Bombardment of the entire film thickness led, as might be expected to resistivities that increase both with the energy and current of bombarding ion beam. For bombardment of the initial stages of film growth only, however, there is a tendency for the resistivity to show a slight decrease compared with the unbombarded film. The decrease is unfortunately not well marked, and beyond a 5 nm thickness of bombarded material the scatter in the results increases considerably, bombardment at 50 eV and low ion current actually showing a substantial decrease. This particular result might be worth further investigation. At this stage we can conclude from the results of ion-assisted deposition of the early stages of a metal film appears acceptable and that this should make it possible to obtain some of the benefits of the ion-assisted process without suffering the degradation that can also accompany it.

Ion-assisted deposition of nitrides

The usefulness of aluminum oxide-nitride materials was illustrated by the construction of a simple coating of the rugate type where the index contrast was approximately 1.83 to 1.66. The control of the process was only semiautomatic and therefore instead of a continuous variation of refractive index a 10-step approximation, figure 6, was used. The resulting filter characteristic curve is shown in figure 7. In the construction of this filter the only variable was the background pressure of oxygen in the coating plant. The evaporant material was aluminum, evaporated at a constant rate. The bombarding ions were nitrogen. Since oxygen is much more reactive than nitrogen, the composition of the resultant film could be varied right up to virtually pure aluminum oxide simply by varying the background oxygen pressure.

More recently we have been investigating the nature of the aluminum-oxygen-nitrogen material with the primary objective of determining whether the material produced by our ion-assisted deposition is simply a mixture of aluminum oxide and aluminum nitride or a true aluminum oxinitride compound. If it were a

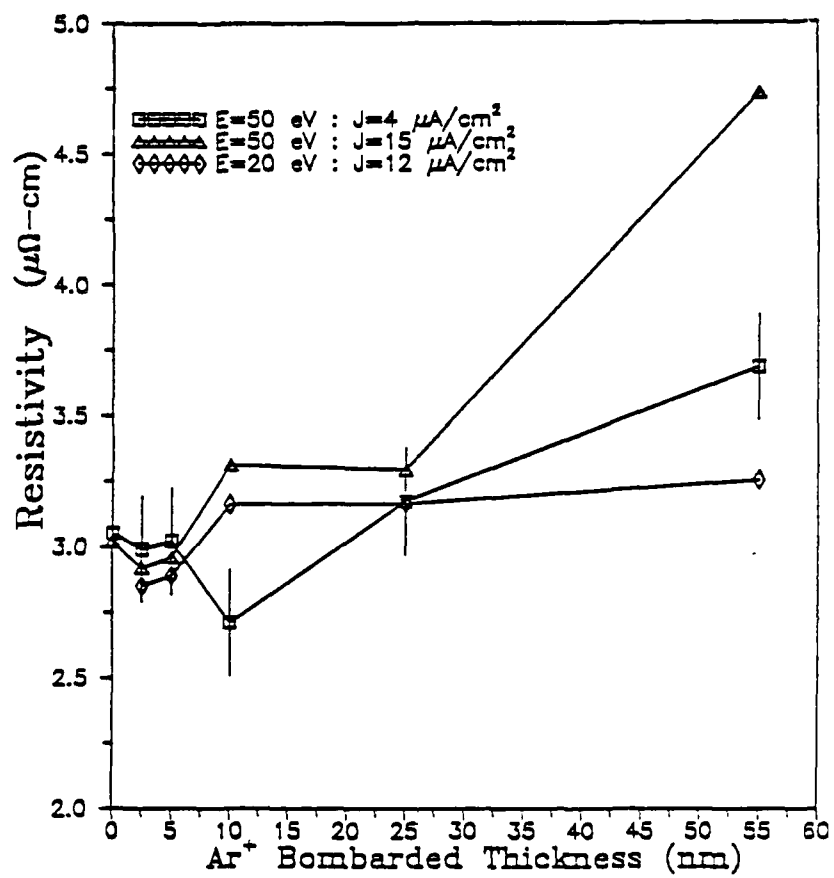


Figure 5:

Resistivity of low energy IAD silver films as a function of the thickness of the bombarded portion. All films were 55 nm in total thickness. (Hwangbo)

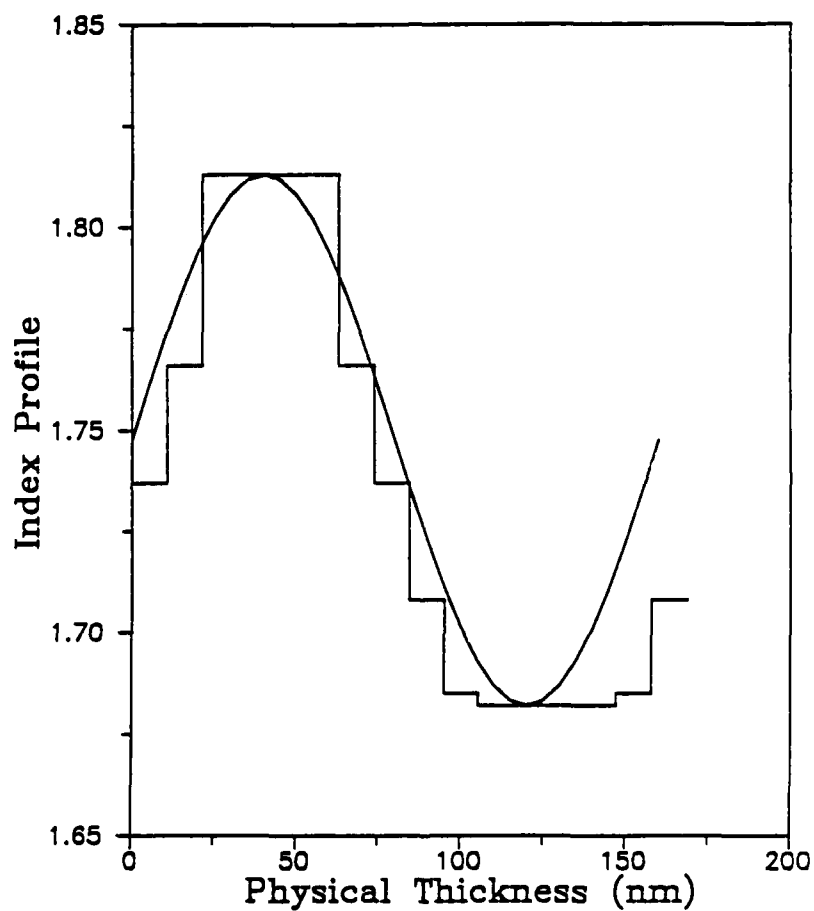


Figure 6:

A step-index profile of AlO_xN_y films from Fig. 1 for a rugate filter. One cycle consists of 10 homogeneous step-index layers and has a 168.6 nm physical index. A sinusoidal curve is fitted to the step-index profile. (Hwangbo)

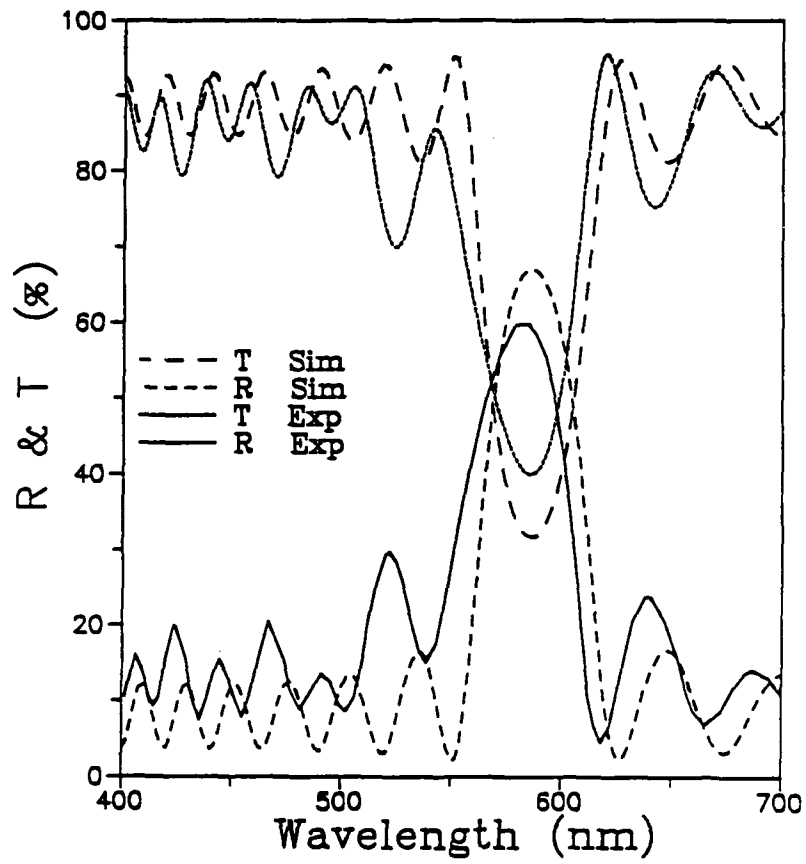


Figure 7:

Reflectance (R) and transmittance (T) of the real and simulated rugate filters. 15 cycles were employed. (Hwangbo)

mixture then we might expect the x-ray photoelectron spectra to show evidence of this. The aluminum 2p peaks of the compound film show no evidence of two separate compounds involving aluminum. The same appears true of the oxygen 1s peaks but the nitrogen spectrum, figure 8, is more complicated. At low nitrogen content, there is an extra nitrogen peak at a somewhat higher energy than the main peak. This peak has been seen by other workers when aluminum nitride was baked at elevated temperatures and attributed to aluminum oxynitride. Since we see the peak only when the nitrogen content is low and the oxygen content high, we believe it may be rather an interaction between nitrogen and oxygen directly. The aluminum and oxygen peaks at this composition tend to show the same energy as Al_2O_3 . At higher nitrogen concentrations the small second peak disappears and we appear to have true aluminum oxynitride. A fuller discussion of these interesting results, including the complete set of spectra, is to be found in Hwangbo's dissertation.

Lanthanide trifluorides

The lanthanide trifluorides have been the subject of investigation by the Thin Film Group at the University of Arizona for some time. They are materials with great promise for optical coating applications because of their wide range of transparency from the extreme UV through to the far IR. They are of low refractive index in the infrared and this increase still further their potential usefulness. Unfortunately they suffer from exceedingly high intrinsic tensile stress when conventionally deposited, stress that is sufficiently high to lead to tensile failure when layers are thick enough to be useful in the infrared, or when they are used in multilayers. Ion-assisted deposition is the only process that promises complete stress control in coatings and therefore it was of interest to investigate the use of ion-assisted deposition in studying the lanthanide fluorides. Briefly, some of the series are polymorphic and in their deposition the predominant crystalline form which we obtained at low substrate temperatures was the high-temperature structure, while at high substrate temperatures we found a predominance of the low temperature form. This result is a consequence of the nonequilibrium nature of the process and especially the rapid quenching. Particular attention was paid in the ion-assisted experiments to samarium fluoride. Figure 9 shows the infrared transmittance of both conventionally deposited and ion assisted samarium fluoride. Conventional deposition of samarium trifluoride at room temperature gives the high temperature hexagonal phase with the (111) orientation stronger than the (110). Increasing the substrate temperature to 200°C and above led to the appearance of the low temperature orthorhombic phase which tended to show a (111) orientation. Ion-assisted deposition at low temperature should, if the mechanism is the same as that of substrate heating, tend to produce the orthorhombic phase. No such tendency was

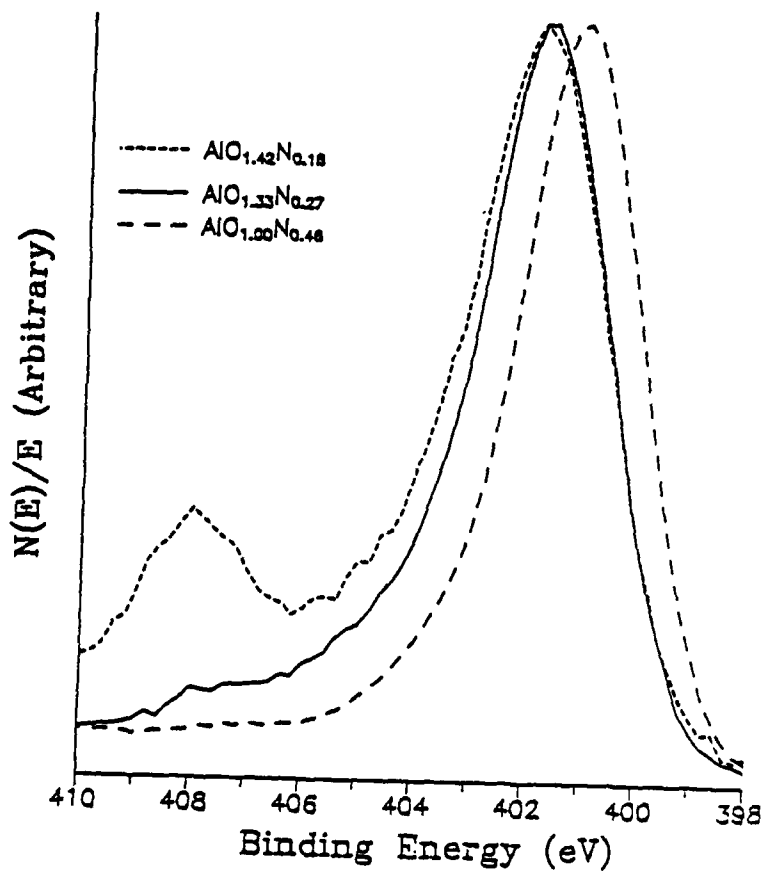


Figure 8:

XPS measurements of the main N1s peaks of AlO_xN_y and the appearance of new peaks at higher energy for (a) and (b).

- (a) $AlO_{1.42}N_{0.18}$
- (b) $AlO_{1.33}N_{0.27}$
- (c) $AlO_{1.00}N_{0.46}$
- (d) $AlO_{0.84}N_{0.60}$
- (e) $AlN_{1.23}$

(Hwangbo)

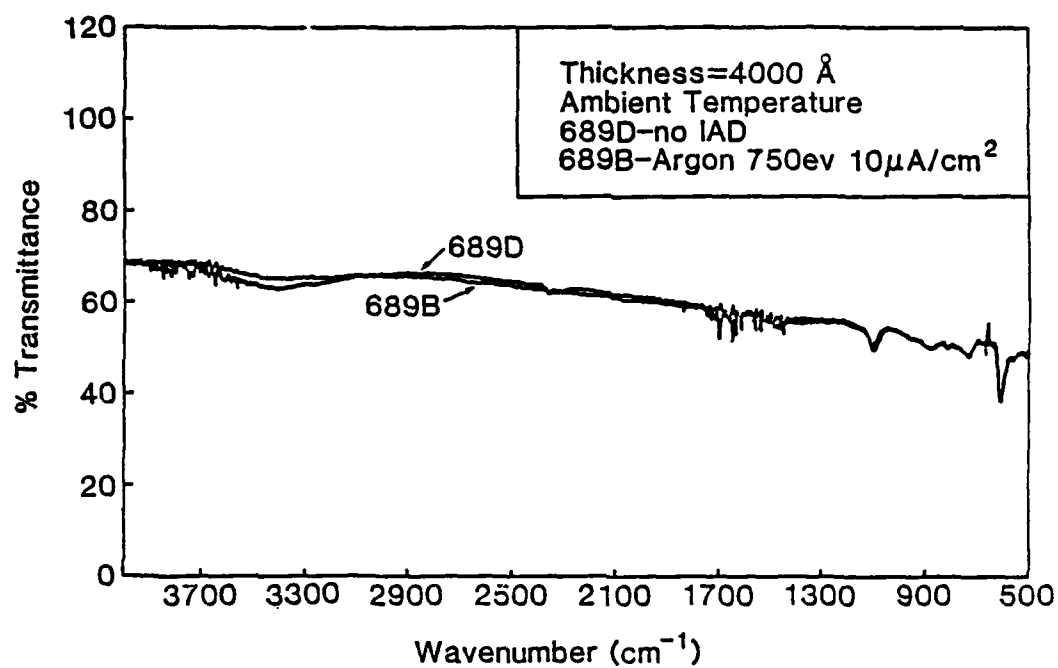


Figure 9:

The infrared transmittance of films of samarium fluoride (Lingg)

observed. Low temperature ion-assisted deposition gave the hexagonal phase but the strong orientation was (110) with some evidence of (111). Increasing the degree of bombardment still did not lead to the orthorhombic phase but eventually resulted in the appearance of x-ray diffraction peaks characteristic of a number of samarium-fluorine compounds with F to Sm ratios less than three together with a further reduction in the hexagonal (111) intensity. Thus ion-assisted deposition leads to a change in the preferred orientation of the crystalline structure rather than a complete change in structure and the mechanism does not appear to be simply thermal. In fact in our previous reports we have described the evidence that leads us to believe that a principal mechanism in the compaction of the growing film is transfer of momentum. We are not, however, in a position to state unequivocally that it is this same momentum transfer that is responsible for the changes in crystalline orientation, but just that the mechanism is not a straightforward thermal one. The investigation of the lanthanide series is described in Lingg's dissertation.

FILM GROWTH MODELING

The statistical properties of surfaces of films grown using a Monte Carlo model where the adatoms have a certain mobility on the surface after arrival. This is a good approximation to the more realistic case of thermally activated hopping. The atoms that take part in thermally activated hopping are confined largely to the surface and are inhibited from further hopping when they are buried under freshly arrived material. Thus the mobility in the Monte Carlo model is to be considered to be the permitted amount of movement of the adatom before it becomes pinned under further material and is an increasing function of deposition temperature and decreasing function of deposition rate. Larger scale deposition models become possible with the scheme than could be achieved by the thermally activated hopping model. It then becomes interesting to examine the surface statistics and eventually to compare them with measurements on real films. Figure 10 onwards illustrate some of the results and a summary is given in Table 1. The conclusions that we can draw from this study so far is that over several orders of magnitude the simple ballistic deposition model predicts that thin film surface have a fractal nature, that the low-frequency cut-off of the fractal behaviour appears to decrease as film thickness increases and that increasing adatom mobility appears to decrease the fractal dimension. Just as an information, figures 11 to 16 give an idea of the results given by our model of film growth. We will find the problems of surface statistics at the scale of optical defects in the section devoted to scattering studies in Marseilles. More information on this topic will eventually be published in Sargent's PhD dissertation, in preparation at present.

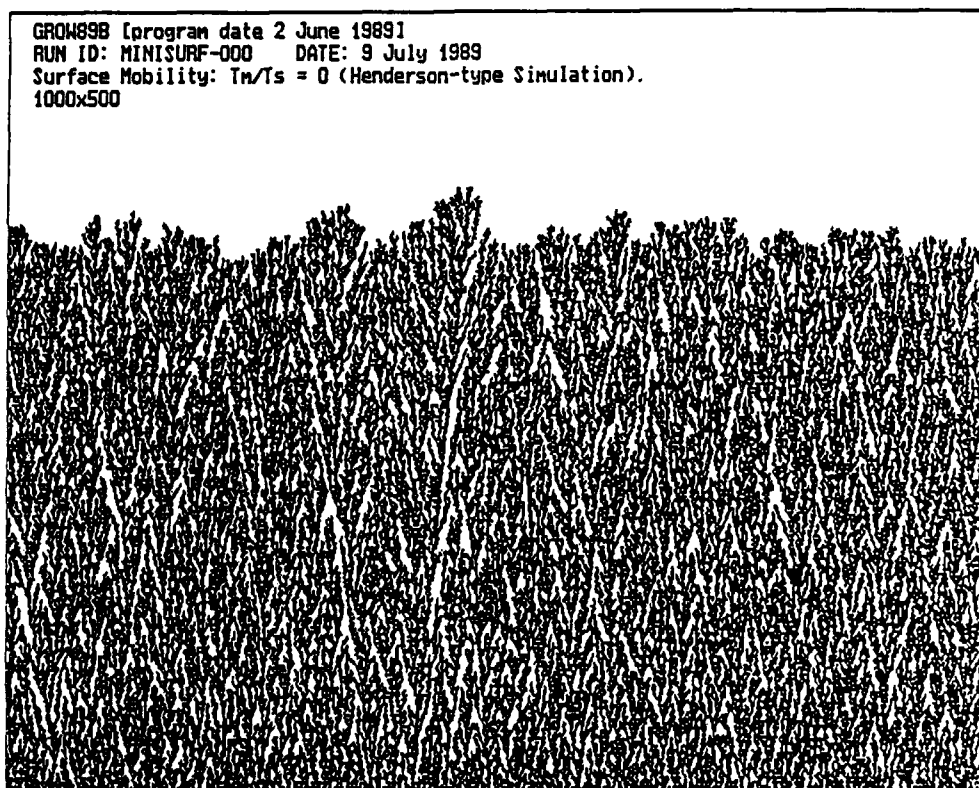


Figure 10:

Simulation of film grown under conditions of zero mobility. (Sargent)

Properties as a function of adatom mobility

Mobility τ_m/τ_d	chi	n	K	D	dens	avg	rms
0	0.59	1.88	.68	1.56	.63	463	12.19
1	1.10	1.93	.48	1.54	.72	463	11.50
2	1.19	1.90	.67	1.55	.74	465	11.45
4	1.44	1.99	.40	1.51	.77	465	12.73
8	1.92	2.03	.18	1.49	.82	479	7.29
16	2.41	2.08	.14	1.46	.84	481	6.07
32	2.77	2.10	.15	1.45	.87	482	6.63
64	2.98	2.05	.20	1.48	.90	480	8.67

chi: average surface diffusion length in
adatom diameters.
n: value of power in inverse power law
spectrum.
K: value of constant in inverse power law
spectrum.
D: Hausdorff fractal dimension.
dens: density of structure relative to 2D hcp
close-packed.
avg: average height of surface (in cells).
rms: rms deviation of surface (in cells).

Table 1:

Results of a number of film growth simulations.

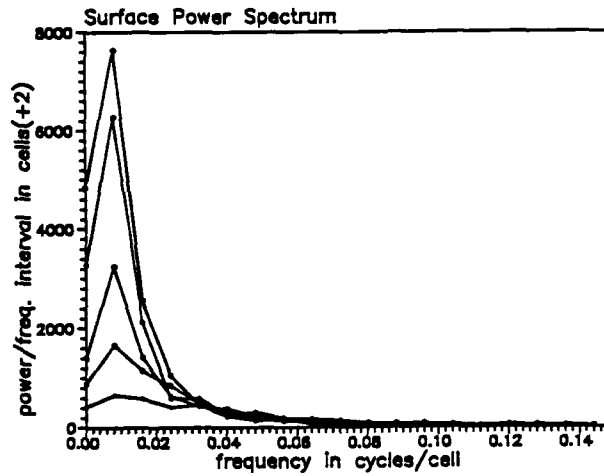


Figure: Surface power spectra of run minisurf-000 for nominal thicknesses of 100, 200, 300, 400, and 500 cells.

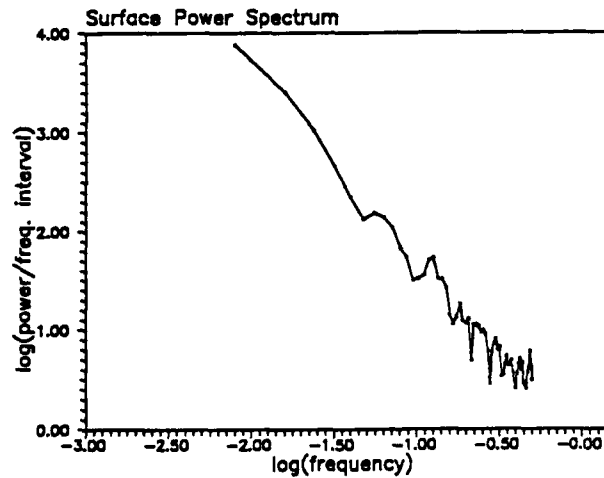


Figure: Surface power spectrum of run minisurf-000 plotted on a log-log scale for a nominal thickness of 500 cells.

Figure 11:

Statistics of the film surface in figure 10. (Sargent)

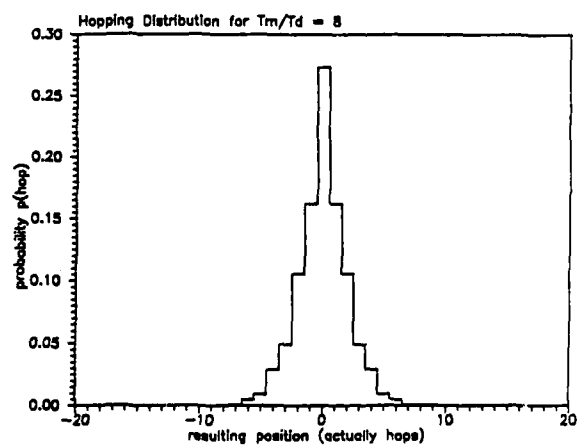
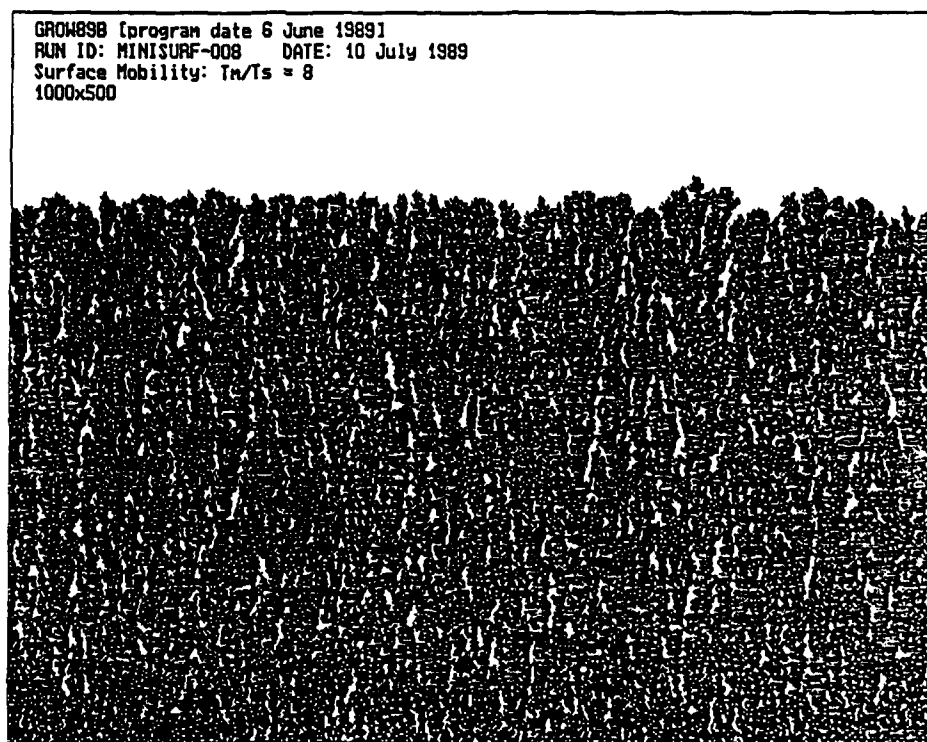


Figure 12:

Film grown under conditions of high mobility. (Sargent)

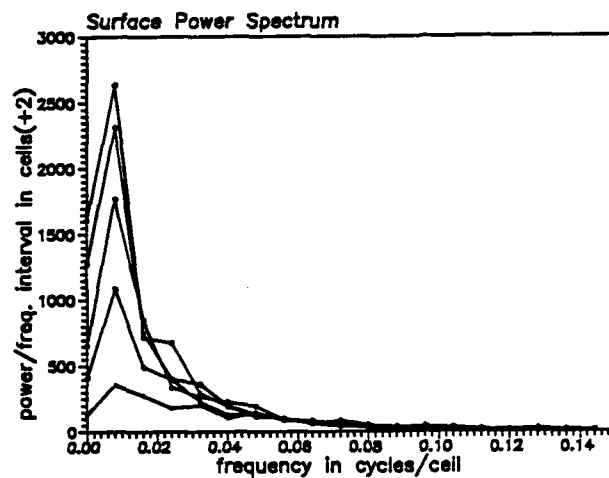


Figure: Surface power spectra of run minisurf-008 for nominal thicknesses of 100, 200, 300, 400, and 500 cells.

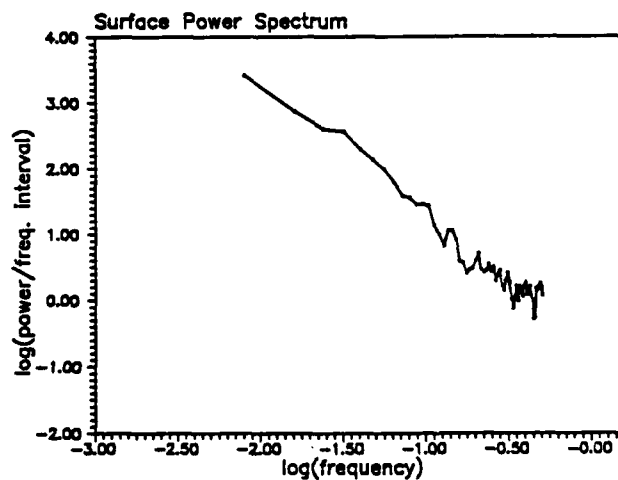


Figure: Surface power spectrum of run minisurf-008 plotted on a log-log scale for a nominal thickness of 500 cells.

Figure 13:

Statistics of film surface in figure 12. (Sargent)

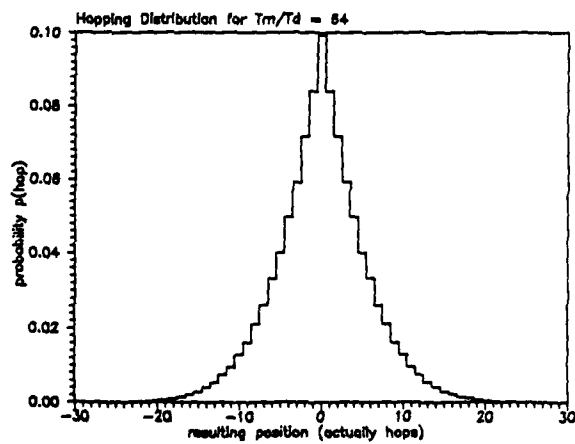
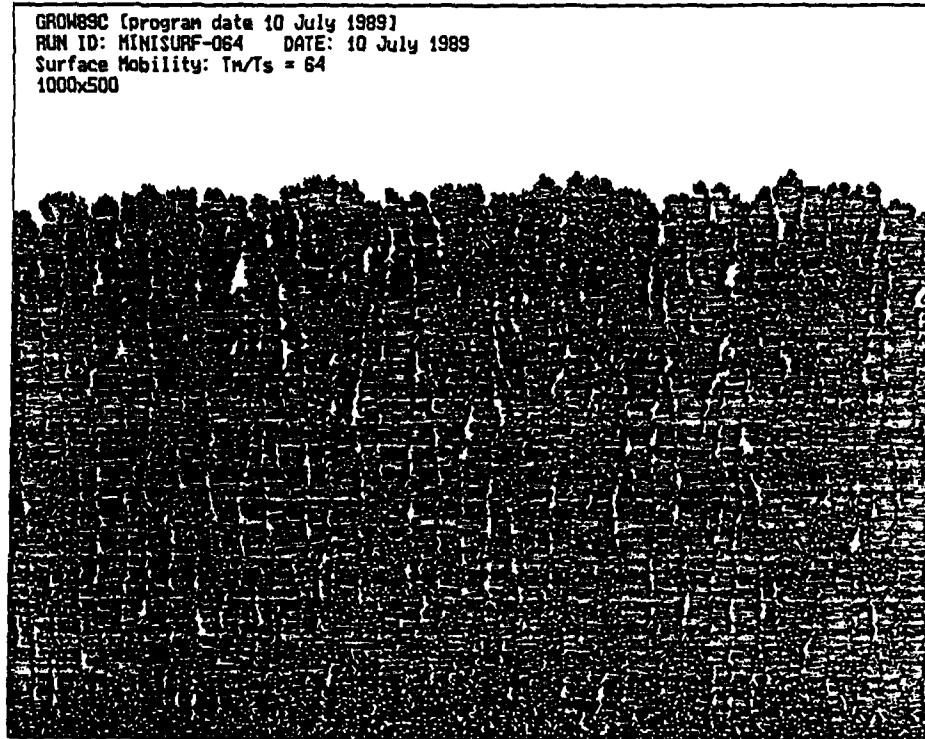


Figure 14:

Film grown under conditions of very high mobility. (Sargent)

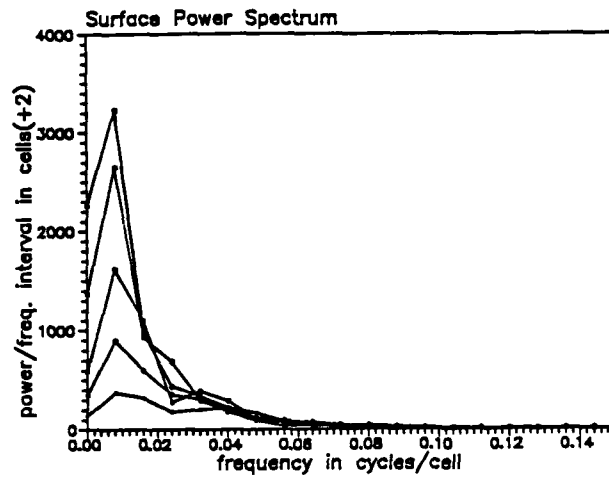


Figure: Surface power spectra of run minisurf-064 for nominal thicknesses of 100, 200, 300, 400, and 500 cells.

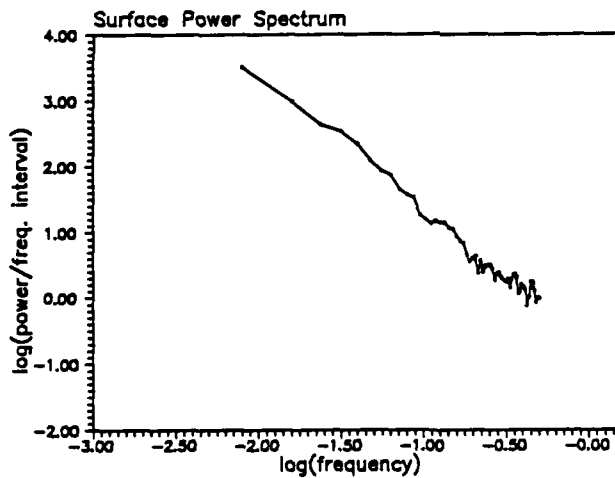


Figure: Surface power spectrum of run minisurf-064 plotted on a log-log scale for a nominal thickness of 500 cells.

Figure 15:

Statistics of the surface in figure 14. (Sargent)

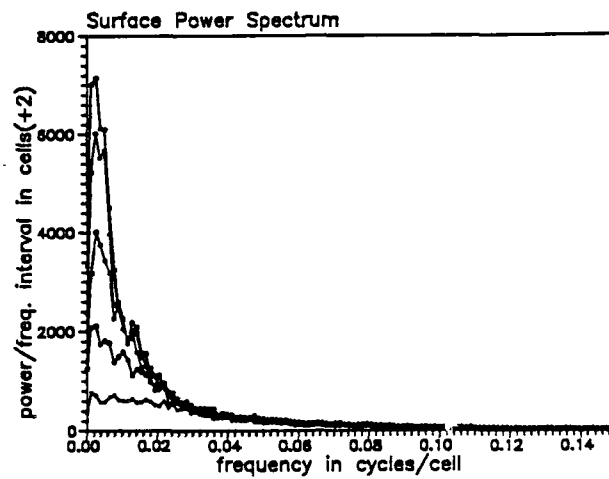


Figure: Surface power spectra of run surf-002 for nominal thicknesses of 100, 200, 300, 400, and 500 cells.

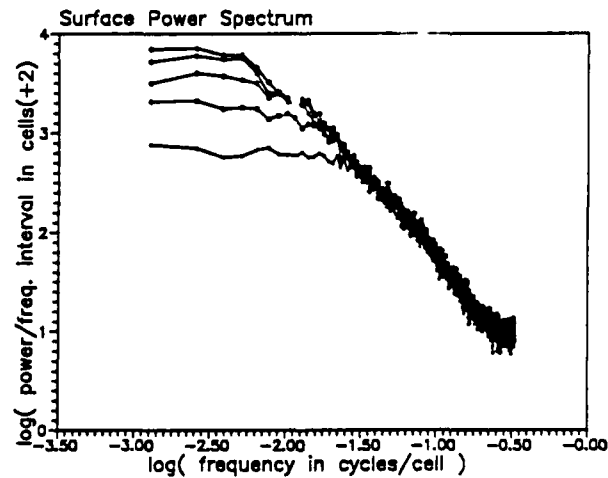


Figure: Surface power spectra of run surf-002 plotted on a log-log scale for nominal thicknesses of 100, 200, 300, 400, and 500 cells.

Figure 16:

Statistics of a very large simulation showing the variation of the statistical parameters with film thickness. (Sargent)

COMPARATIVE STUDY OF ION-ASSISTED DEPOSITION (IAD) AND REACTIVE ION PLATING (RIP) TECHNIQUES FOR PRODUCTION OF TiO_2 , Ta_2O_5 , SiO_2

At the present time IAD and RIP techniques are currently used in many optical laboratories; we give here only a short review concerning these two techniques before the analysis of the optical characterization concerning the layers produced in Marseilles Laboratory.

Ion Assisted Deposition (IAD)

As in the case of classical reactive evaporation, the deposition is made by evaporation of materials with an electron gun. The relative position of the electron gun with respect to the substrates has been adjusted to obtain the best deposition uniformity. The control and the regulation of the deposition rate is obtained with a quartz microbalance. For the deposition of metallic oxides as TiO_2 or SiO_2 it is necessary to operate in oxygen reactive pressure servo controlled on the O_2 partial pressure (with a quadripolar mass spectrometer) or on the total pressure. In the case of a ion beam assistance, it is not necessary to heat the substrates; the layer in formation is bombarded with a beam of Argon and Oxygen ions with energies of some hundreds of eV.

The hot cathode ion gun we use includes a 8 cm in diameter output grid and is 40 cm apart from the monitoring substrate center (fig 17).

We can consider that the ions exchange their energy with the condensing material by transfer of momentum. The effect obtained depends mainly on the ion mass, the ion energy and on the ion current density on the coated surface. Electrons are coupled to the ion beam with a filament in such a way to neutralize the total space charge. We use defocused grids to obtain a slightly open ion beam.

Reactive Ion Plating (RIP)

The Reactive Ion Plating processus is a combination of evaporation and pulverization (fig 18). The coating apparatus is a BAK 800 IP from Balzers.

The setting of the different elements in the vacuum chamber is practically the same as for evaporation techniques, but the substrate holder is electrically isolated. The electron guns are isolated from ground and a potential of about 40 V is established between a heated filament, emitting electrons, and the evaporation crucible in process. The argon gas is introduced close to the filament; the oxygen gas is introduced close to the crucible and the discharge is established between filament and crucible.

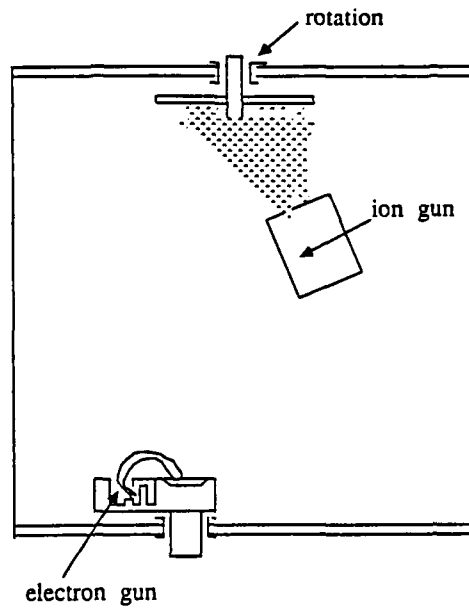


Figure 17:
Ion Assisted Deposition

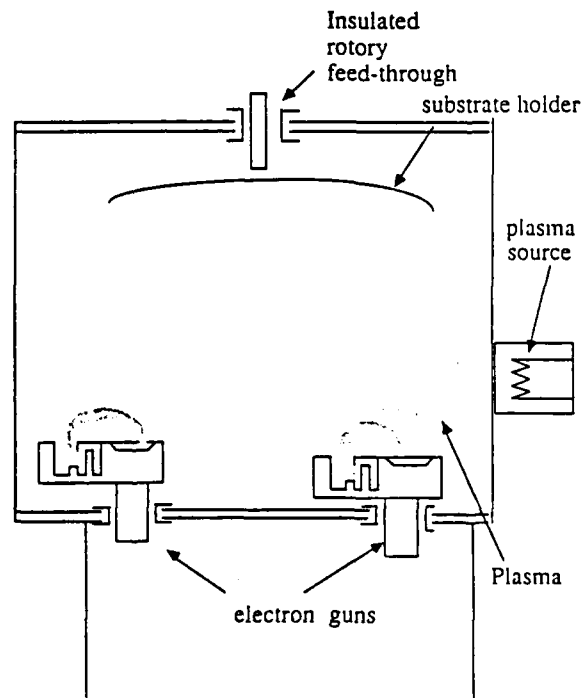


Figure 18:
Reactive Ion Plating

The evaporation is performed in the presence of the gas discharge. In collisions and electron impact reactions, coating material ions are formed and accelerated in the electric field so that condensation and film formation take place under the influence of ion bombardment. This complex process is not well defined but has numerous advantages: in addition with acceleration of coating material in the plasma collisions, charge effects make the reaction between materials easier. This process is especially efficient for the formation of oxides and nitrides. The relatively high gas pressure in the evaporation chamber (10^{-3} Torr) and the large size of the crucibles give uniform coatings on a large area.

Characterization of optical performances

The main interest of the IAD and RIP techniques in comparison with classical reactive evaporation is that the layers produced are not sensitive to hygrometry when the parameters of deposition have been well adjusted. One can demonstrate that the index shift during air admission is completely negligible.

For these layers we will present our results concerning characterization and obtained in the study of three widely used materials: TiO_2 , Ta_2O_5 and SiO_2 .

For each deposition technique, we tried systematically to adjust the parameters to obtain a good repeatability in layer production. Concerning IAD, we show that the quality of vacuum is a preponderant parameter, by comparing results obtained on layers realized with cryogenic pumping and with classical diffusion pump. The results are given in Table II.

- the refractive index is represented as the development

$$n = A + \frac{B}{\lambda^2} + \frac{C}{\lambda^4} \quad \text{where } \lambda \text{ is expressed in } \mu\text{m}$$

For an easy comparison, we give also the value of n obtained for $\lambda = 0.63 \mu\text{m}$.

Inhomogeneity defects are very low. With our notations, Δn represents the global variation in the volume of the layer and the ratio $\Delta n/n$ is also given.

Concerning the extinction coefficients measured with photothermal methods, we can observe that IAD leads to values lower than Ion Plating. At the present time we make some attempts to see in what extent it is possible to reduce absorption losses with this Ion Plating technique.

	TiO ₂				Ta ₂ O ₅				SiO ₂			
	e ⁻ beam évap. (1)	IAD diff. pump	IAD cryo. pump	RIP	e ⁻ beam (1)	IAD	RIP	e ⁻ beam (1)	IAD	RIP		
Cauchy μm^2		2.2327	2.2973	2.3802		2.0365	2.1558		1.48	1.4779		
coeff μm^4		2.5622x10 ⁻²	2.3915x10 ⁻²	3.0424x10 ⁻²		2.6655x10 ⁻²	2.3685x10 ⁻²		0.46x10 ⁻²	0.4045x10 ⁻²		
		5.3153x10 ⁻³	4.9546x10 ⁻³	6.12x10 ⁻³		0.1263x10 ⁻³	1.0978x10 ⁻³		-0.088x10 ⁻³	-0.0545x10 ⁻³		
refractive index (633 nm)	2 → 2.3	2.33	2.39	2.49	≡ 2.10	2.11	2.22	≡ 1.46	1.49	1.49		
extinction coefficient (633 nm)	4 x 10 ⁻⁵	2 x 10 ⁻⁴	1 x 10 ⁻⁵	5 x 10 ⁻⁴	< 10 ⁻⁵	3 x 10 ⁻⁵	≡ 10 ⁻⁵	< 10 ⁻⁵	2 x 10 ⁻⁴	(2)		
inhomogeneity $\Delta n/h$	10% → 1%	< 1%	< 1%	< 1%	< 1%	< 1%	< 1%	< 1%	< 1%	< 1%		
grain size (rms)	11Å → 3Å	≡ 3Å	< 5Å	< 5Å	≡ 8Å	≡ 8Å	< 5Å	< 5Å	< 5Å	< 5Å		

(1) Depends on deposition conditions

(2) Under investigation

(3) ≤ 10⁻⁶ after baking in air (24 h. at 400°C)

Table II:

Comparison of results obtained with classical evaporation, Ion Assisted Deposition and Ion Plating

The grain size measured on IAD layers is interesting because it is much lower than in TiO_2 layers obtained by classical evaporation. On this subject we have not yet got any result with Ion Plating.

To conclude, for TiO_2 layers, we have shown that both IAD and Reactive Ion Plating exhibit numerous advantages compared with classical evaporation: first, spontaneous moisture adsorption is completely eliminated. Furthermore, the repeatability of the index value is easily obtained with the additional advantage of a negligible defect of homogeneity.

A detailed comparison of IAD and RIP methods must also concern the problems of uniformity of deposition. As soon as great dimensioned surfaces are involved (several tens of centimeters in diameter) Ion Plating seems to be best fitted. With IAD we are limited by the dimensions of the ion beam. It can be deduced from this study that, to obtain minimal losses, the IAD technique with a cryogenic pumping can lead to the best results. Obviously, we cannot be sure that the performances given here for RIP techniques cannot be improved.

It would be interesting to develop all these studies to other materials to produce optical layers, but it is impossible to perform all this work without an extensive cooperation between several laboratories. The exchange of results between Tucson and Marseille is very useful to help this study of the techniques of deposition.

MEASUREMENTS OF ABSORPTION LOSSES BY COLLINEAR PHOTOTHERMAL DEFLECTION TECHNIQUE

Our technique of measurement of absorption losses in a layer by photothermal deflection spectroscopy has been improved in order to have a good calibration of the measurements. From them by calculation we can deduce the value of the extinction coefficient k , knowing the value of the real part of the refractive index and thickness (determined both by spectrophotometric measurements).

In this report we will not recall the detail of the principle of the collinear photothermal apparatus we used; it has been described elsewhere in the literature.

Extinction coefficients of titanium dioxide films prepared using different techniques.

We have applied this collinear photothermal deflection method to the determination of extinction coefficients of single layer TiO_2 films. The results presented concern the samples prepared for the 1986 OSA annual meeting. All these TiO_2 layers have been deposited by different techniques on identical silica substrates. Table III gives the list of the 19 samples we have measured, with the

Number	Technique	Supplier
003	E.B.	Spectra Physics, CA
006	E.B.	Spectra Physics, CA
025	E.B.	Leybold Heraeus, Hanau
138	E.B.	Optical Sciences Center, AZ
052	E.B.	Indian Inst. of Science
094	E.B.	Martin Marietta Aerospace, NM
036	E.B.	Opto Mechanik, FL
024	I.A.D.	Leybold Heraeus, Hanau
137	I.A.D.	Optical Sciences Center, AZ
143	I.A.D.	Optical Sciences Center, AZ
013	I.A.D.	Univ. of New Mexico
011	I.A.D.	Univ. of New Mexico
135	I.B.S.D.	Rockwell, CA
078	I.B.S.D.	Colorado State, Univ. CO
120	I.B.S.D.	O.C.L.I.
057	A.R.E.	Indian Inst. of Science
093	R.F.S.	Battelle - N.W.L., WA
165	I.P.	Balzars
114	I.P.	O.C.L.I.
026		bare substrate
124		bare substrate
125		bare substrate

E.B. Electrom Beam Evaporation
 I.A.D. Ion Assisted Deposition
 I.B.S.D. Ion Beam Sputter Deposition
 A.R.E. Activated Reactive Evaporation
 R.F.S. RF Diode Sputtering
 I.P. Ion (or Plasma) Plating

Table III:

Suppliers of Titania films
 (OSA meeting 1989 - published in: "Comparison of the properties of Titanium dioxide films prepared using various techniques," J.M. Bennert, E. Pelletier, G. Albrand, J.P. Borgogno, B. Lazarides, C.K. Carniglia, R.A. Schmell; T.H. Allen, T. Tuttle-Hart, K.H. Guenther, A. Saxer, Applied Optics, 28, 3303-3317 (1989))

preparation methods used and suppliers name. Table IV gives, for each sample, the values of refractive index n for $\lambda = 600$ nm and of thickness e , values determined at ENSPM by spectrophotometry, together with the absorption losses A measured by the photothermal method. Finally, the values of the extinction coefficient k of the material constituting the layer calculated from those of A , n and e are given. We can state that the k values determined by the photothermal technique are consistent with those determined at ENSPM by spectrophotometry (not given here).

Sample N°	Technique	n^* ($\lambda=600\text{nm}$)	$e(\text{nm})^*$	$A(t=0) \times 10^5^{**}$ ($I=30^\circ$ -Pol S)	$k \times 10^5^{**}$ extinction coef.	ΔA A
003	EB	2,292	308	22	4,1	-0,14
006		2,279	315	53	10	-0,05
025		2,338	345	122	23	-0,04
138		2,280	310	60	11	+0,48
052		2,181	386	30	4,4	-0,12
094	IAD	2,222	333	43	8	-0,05
036		2,330	299	83	15	-0,17
024		2,472	300	2	0,4	0
137		2,401	283	30	5,5	+0,55
143		2,393	267	200	33	+0,09
013	IBSD	2,318	238	52	12	-0,15
011		2,438	314	70	16	-0,22
135		2,446	285	24	4,8	0
078		2,386	209	120	39	-0,04
120		2,508	266	98	18	0
057	ARE	2,172	374	32	5,3	-0,03
093	RFS	2,500	264	28	5,1	0
165	IP	2,483	272	20	3,6	0
114		2,575	261	21	4,1	0

Table IV:

OSA samples. Measurements of n , e , A performed in Marseilles by:

*Spectrophotometric measurements (6 - 7)

** Photothermal deflection measurement.

Absorption has been measured at different points of the sample surface. The uniformity is rather good on a diameter of 5 mm since the relative deviations are smaller than 20%; the only exception is sample 078 (IBSD) which possesses a very poor uniformity (deviations of more than 40%).

The first question we can ask is: does the value of k depend on the deposition technique used? The results concerning the statistics of the values of the extinction coefficient are given in the form of 4 histograms (fig. 19). The values of the extinction coefficient are given on the abscissa in logarithmic scale. Each of the histograms a, b, c, d, is related to a deposition technique: respectively Electron Beam samples (2-a), Ion Assisted Deposition samples (2-b), Ion Beam Sputter Deposition samples (2-c) and samples from other techniques (2-d) are pictured as striped columns. In each histogram the k values for all the other samples (dotted columns) are also given.

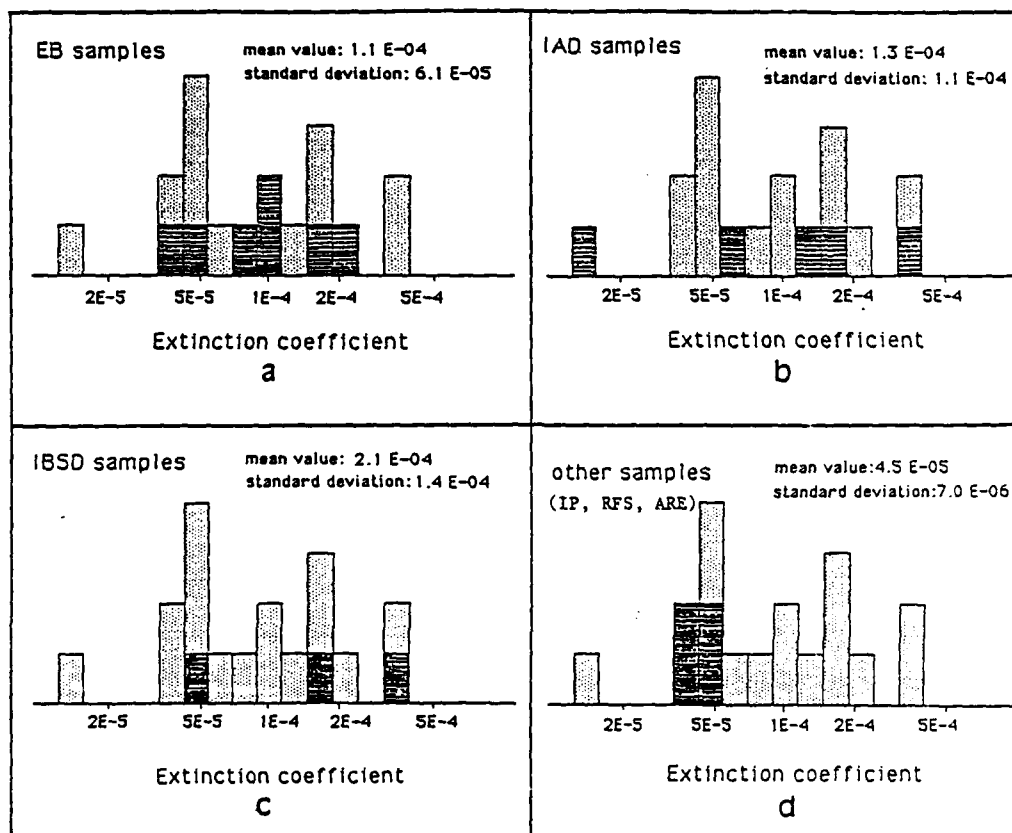


Figure 19:

Histograms of extinction coefficients. Each figure is related to a deposition technique - a: EB samples; b: IAD samples; c: IBSD samples; d: other samples (ARE, RFS, IP)

If we take a mean value of the extinction coefficient on the whole set of samples, we obtain $1.2 \cdot 10^{-4}$.

- we find the same mean value for the EB samples ($1.1 \cdot 10^{-4}$) and for the IAD samples ($1.3 \cdot 10^{-4}$).

- this mean value is higher for the IBSD samples ($2.1 \cdot 10^{-4}$). However this set consists of only three samples. Among them the n° 078 which is non uniform and highly absorbing ($k \approx 4 \cdot 10^{-4}$). This leads us to ignore it.

- the mean value of k is lower ($0.4 \cdot 10^{-4}$) for the four samples of the last group, corresponding to other different techniques (ARE, RFS, IP).

We must note that, in each set of samples, the standard deviations are very high except for the last one (ARE, RFS, IP). These very high values seem to be a consequence of the fact that the samples have been produced by different laboratories, with different deposition conditions.

For all these 19 samples measured there is no obvious correlation between the value of the extinction coefficient of the deposited material and the technique of film deposition. EB, IAD or IBSD give high as well as low absorbing layers. RFS and IP samples have somewhat lower values of k but we don't have enough samples of these techniques to reach any conclusion.

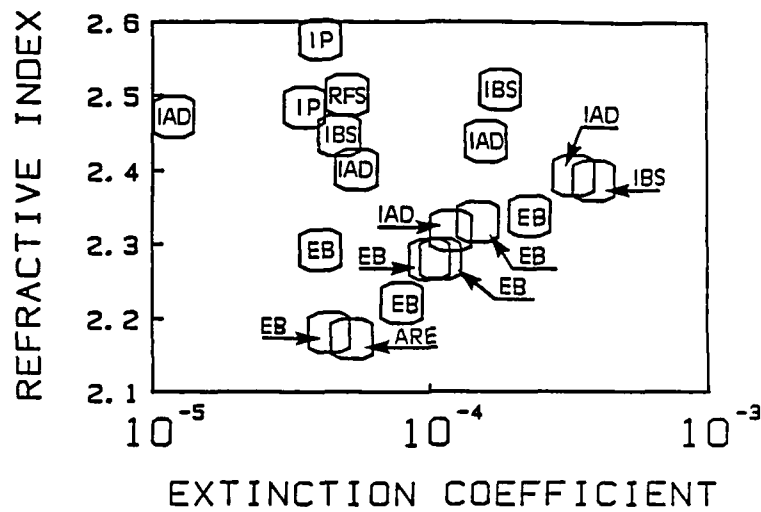
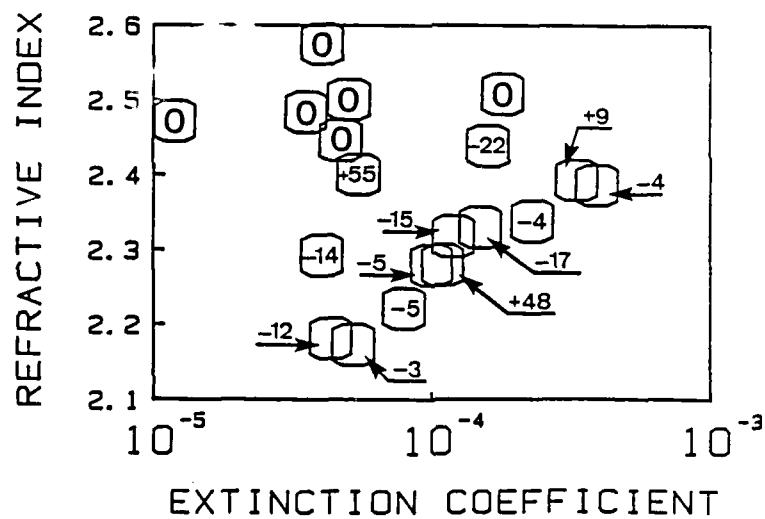
The refractive index n is plotted versus k in figure 20a (for all samples (Table III). We already know that the n values are related to the deposition technique: EB samples have the lowest n values, IAD samples have higher n values and IBSD samples or IP samples have the highest n values. Furthermore, from figure 20a we can see that the five layers with both high refractive index and low extinction coefficient (upper left part of the figure 3) are produced by IP (2 samples/2), RFS (1 sample/1), IBSD (1 sample/3) and even IAD (1 sample/5). If we consider only the mean values of n and k , for each technique, we find that IP and RFS produce titania films with both the highest n value and the lowest k value. Further experiments with more samples prepared by each technique seem necessary to confirm these results.

Photo-induced absorption change in titania layers

Evolution of illuminated layers

The values of absorption coefficient given in Table II are initial values: the first photothermal measurement is performed about 1 minute after beginning illumination of the sample (the measurement itself takes a few seconds). For each sample, the photothermal signal is recorded over at least half an hour.

When the samples are illuminated by the dye laser for several hours, an evolution in the photothermal signal is often observed. It is the case for 13 of the 19

**a****b****Figure 20:**

Refractive index versus extinction coefficient. Each sample is pictured as a square. In figure (a), the deposition technique is indicated inside the square. In figure (b), the $\Delta A/A$ values, expressed as a percentage, are given inside the squares.

TiO₂ samples from OSA. It is strange to observe that for ten of them absorption decreases with time while it increases for the three other samples. The six remaining samples were perfectly stable during laser exposure, even after several hours.

It is interesting to study more carefully this phenomenon and to display the law of absorption variation with time t . In fig. 21 are plotted the curves giving $A(t)/A(t=0)$ for some of the OSA samples compared with samples from our laboratory.

a - TiO₂ n° 11 - OSA (Univ. of New Mexico - IAD)

b - TiO₂ (Marseille - IAD)

c - TiO₂ n° 137 - OSA (OSC - IAD)

d - TiO₂ n° 120 OSA (OCLI - IBSD)

If we consider the curve 21a, we observe a rapid decrease of absorption during the first ten minutes of illumination, then the change of absorption becomes nearly constant with time. Some films manufactured in Marseille present the same evolution (curve 21b).

Curve 21c gives the other kind of evolution of absorption; it corresponds to one of the three OSA samples in which the absorption increases with exposure time (TiO₂ n° 137, n° 138 and n° 143, all of them produced at OSC). It is interesting to note the effect of annealing. These three samples were heated for 48 hours at 200°C. After this, the evolution of $A(t)$ is completely different, since we now observe a decrease versus time. Thus after annealing, the 3 samples have reached a "standard" behavior that is similar to that of most of TiO₂ layers.

Curve 21d concerns a TiO₂ sample whose stability is excellent.

We can verify that absorption has changed only in the illuminated area of the surface: if the sample is moved, the same phenomenon is observed at this other point. We have also noticed that the relative variation of absorption does not depend on the power of the exciting beam, at least in the range 30 mW - 300 mW

Let us now give a brief analysis of the reasons of this evolution. The power density received by the sample being rather high (about 400 W/cm²), we could think that it gives rise to a local overheating. This is why we have observed the surface with a high sensitivity infrared camera. No temperature increase greater than 0.2°C (which is the thermal resolution of the camera) can be detected for samples with absorption coefficient lower than $5 \cdot 10^{-2}$. The phenomenon of absorption change observed is thus not connected with an increase in temperature, but is a photoinduced effect. The photothermal deflection method permits the study, in real time, of the problems of instability of illuminated materials in thin film form.

We can wonder to what extent there is a correlation between temporal instability of TiO₂ layers and other characteristic parameters: refractive index n , extinction coefficient k , and obviously, the deposition technique. For that we have

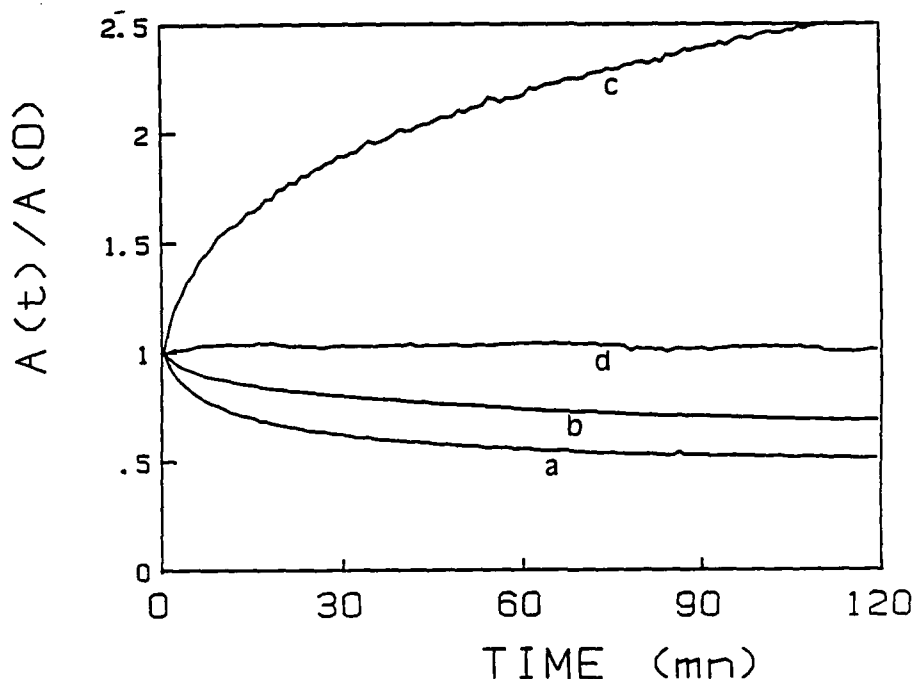


Figure 21:

Relative variations of absorption versus time for 4 illuminated single layer titania films. a: n° 11 (OSA); b: TiO₂ (ENSPM); c: n° 137 (OSA); d: n° 120 (OSA).

given in the last column of table IV the algebraic relative variation after ten minutes of illumination:

$$\frac{\Delta A}{A} = \frac{A(t=10mn) - A(t=0)}{A(t=0)}$$

Figure 20b gives a cartography of the samples in the n, k plane. The figures, inside the square representing each sample, correspond to $\frac{\Delta A}{A}$ expressed as a percentage. The 6 stable samples are marked with a 0. It clearly appears that the only stable samples are those whose index is greater than 2.45. Concerning the extinction coefficient, the situation is more complex: we can find both unstable samples with low k and very stable samples with high extinction coefficients.

However, in figure 3 it is obvious that five of the six stable samples are grouped together in the upper left part of the figure, that is they have both high refractive index and low extinction coefficient. On the other hand, it is interesting to note that these six stable samples correspond to the following techniques: 2 IP (out of 2), 1 RFS (out of 1), 2 IBS (out of 3), 1 IAD (out of 5). None of the 7 samples obtained by EB is stable when illuminated.

Experiments carried out in our laboratory show that it is very difficult to deposit TiO_2 films with high stability, even by IAD. We have observed that IAD films have generally a better stability than EB films. However, IAD technique allows a systematic fabrication of stable Ta_2O_5 layers.

Intermittent illumination

As indicated above, for most of single TiO_2 layers, absorption under illumination decreases. When illumination is stopped, we can observe a partial reversibility of the phenomenon. An example (sample 11) is given in figure 22. Curve a corresponds to a first illumination of 20 min. Between curves a and b, the sample was unilluminated for 20 hours, in the same conditions of temperature and moisture ($T = 20^\circ\text{C}$; 60% moisture). During this time, absorption has partially recovered. The same experiment can be repeated several times with similar evolution under the laser beam, followed by a partial reversibility. The unillumination times are: 24 hours between curves b and c, then 96 hours between c and d and one hour between d and e. The regenerating times are thus rather large with respect to the illumination times.

Figure 22 shows that:

- the mean evolution rate is slower out of the beam than under the beam;
- these two rates are high at the beginning and then rapidly stabilize.

On the other hand, the reversible part of the absorption change depends in a great part on the sample, but we have not found, for this set of samples, an obvious relation between instability under illumination and reversibility.

Influence of the hygrometric degree of atmosphere

It is well known that the moisture content of air modifies optical properties of thin layers. We will show now that it modifies also their stability under and out of the flux. For that a single layer TiO_2 film has been submitted to the following cycle (figure 23):

moisture degree	60 %	→	(point A)	95 %	→	60 %
temperature				20°C		

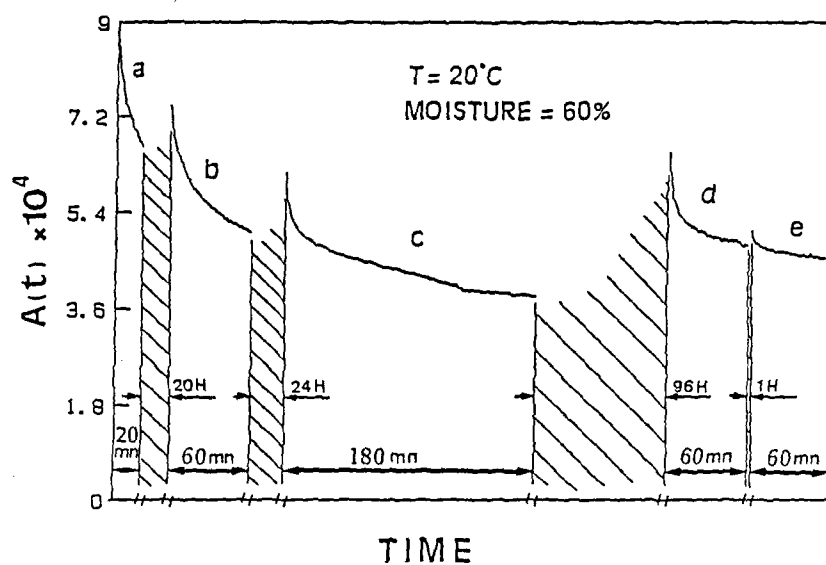


Figure 22:

Intermittent illumination of a single layer titania film.

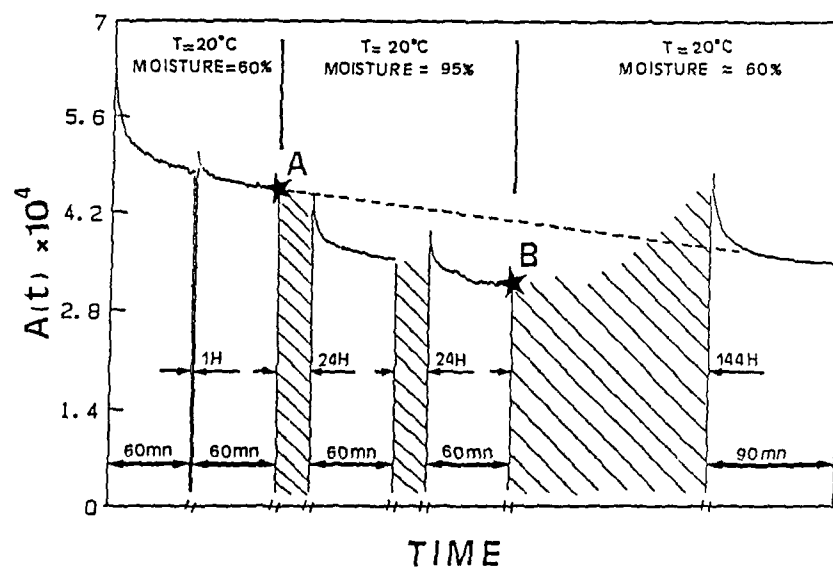


Figure 23:

Influence of hygrometric degree of atmosphere on time dependent absorption change.

Figure 23 shows first that an increase in moisture leads to a decrease in absorption and that this phenomenon is reversible. Then it appears that water saturation prevents the regeneration (point A indicated in the figure 6). We have observed these two phenomena on other samples of a TiO_2 layer.

Conclusion

We have used the very sensitive collinear photothermal deflection method to measure the extinction coefficients $k(\lambda)$ of materials deposited in thin layers on transparent substrates. The limit of detectivity of our apparatus corresponds, for a TiO_2 layer on fused silica substrate, to an extinction coefficient k of some 10^{-7} .

Measurements made on the 19 TiO_2 films manufactured by different techniques (EB, IAD, IBS, RFS, IP) do not display an obvious correlation between the value of k (extreme values: 4×10^{-6} and 390×10^{-6} for $\lambda = 600$ nm) and the deposition technique. However, if we consider both n and k , we find that high values of n and low losses can be obtained with the RFS, IP, IBSD, and even IAD techniques.

In addition we demonstrate that the PDS method is a good means to observe a photoinduced absorption change in some of the layers placed in a laser beam. Most of the TiO_2 layers have decreasing absorption during half an hour of exposure to a beam of irradiance of 400 W/cm^2 .

The relative change of absorption depends in a great part on the sample; it can be very high (55% after ten minutes of illumination), but it is null for the six higher refractive index samples. The IP, RFS and IBSD techniques seem to be the methods of layer production that lead to the highest index values and to the best stability under flux.

MEASUREMENT OF SCATTERING CURVES: STUDY OF THE CORRELATION STATE BETWEEN INTERFACES IN A LAYER STACK

Studies of light scattering from optical coatings are a good mean to characterize materials in thin film form. We have at our disposal in Marseilles experiments and theoretical methods that are both very powerful. Our main attempt was to show how we can obtain results on layer microstructure by using simultaneously theory and experiment. It is of interest to review here the main steps of the reasoning leading to these results. Calculations are not given here. More information about this can be found in the published papers or thesis (in French) from C. Amra and P. Roche.

We know that, in multilayer coatings, the relation giving the energy balance is:

$$1 = R + T + A + D$$

where A and D represent respectively absorption and scattering losses.

These losses A and D are very often extremely low and do not exceed some thousandths. Nevertheless these two values must be perfectly controlled for high performance optical coatings. For this, we must go further in the details of this equation and take account of external scattering directly accessible by measurement and of internal scattering which is practically added to intrinsic absorption of materials in thin films. With our notations, D represents the integral in all the space of the amount of light scattered in each direction: it is the external global scattering.

Many work has been devoted to the study of scattering and particularly on the the law of dependence of D with wavelength. A simple example is given here in figure 24. It concerns a single layer of optical thickness $\lambda_0/2$ and of index $n_c = 2.3$. In this calculation; the roughnesses of interfaces substrate-layer and layer-air are assumed to be identical and α represents the correlation between interfaces. We have considered here only the two extreme cases: $\alpha = 0$ and $\alpha = 1$ which correspond respectively to a perfect correlation and to a complete uncorrelation. Compared with scattering of the bare substrate, it can be seen that the law of variation of D versus λ depends considerably on α .

Numerous studies deal with scattering in multilayer coatings but, due to the high number of parameters involved, the conclusions are very difficult since there are always many solutions to explain the experimental results.

Even in the case of a single layer, if we have acces to the measurement of angular distribution of scattering between 0 and 90°, one can explain the value of scattering by reflection by considering one or the other of the two extreme hypothesis of correlated roughness ($\alpha = 1$) or uncorrelated roughness ($\alpha = 0$).

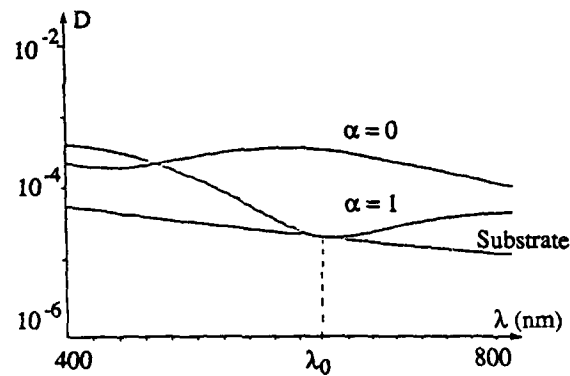


Figure 24:

External global scattering versus λ . The results of the calculation are given for a $\lambda/2$ layer of $n_c = 2.30$. The roughnesses are identical for the two cases: correlated interfaces $\alpha = 1$ and uncorrelated interfaces $\alpha = 0$.

It is obvious that this ambiguity will be very difficult to solve in the case of a stack of many layers since we can vary independently the roughnesses of different interfaces and the states of correlation. We will see here how the use of a causal model together with the measurements of anisotropy variation of scattering permits an easy investigation of microroughness and leads to obvious conclusions to solve this problem.

We want to give a response to this question: what are the key parameters of scattering and what information do they give us on material microstructure at the scale of optical frequencies?

The apparatus intended for the plotting of scattering curve for the wavelength $\lambda = 0.6328 \mu\text{m}$ has been described elsewhere. In the same way, the theory has been given in the literature (Elson, Amra, Bousquet)..

With this vector theory, we can write that the amount of light scattered in the direction (θ, ϕ) is given by the expression:

$$I(\theta, \phi) = \sum_{i,j}^p C_{ij}(\theta, \phi) \alpha_{ij}(\theta, \phi) \gamma_{jj}(\theta, \phi) \quad (1)$$

where

- C_{ij} are called ideal coefficients since they depend only on the perfect stack supposed free of roughness: they depend on the coating design and on the illumination and observation conditions.

- γ_{jj} is the roughness spectrum of the interface j and contains all the information relative to the surface defects. it is the Fourier Transform of the autocorrelation function of the interface profile.

- α_{ij} is the correlation between the interfaces i and j . It can be considered as the degree of coherence between the scattering sources at the interfaces i and j or as the degree of similarity of the surface profiles i and j . Usually, the roughness spectrum is assumed to be the sum of the Hankel Transform of an exponential and a gaussian function; so 4 parameters are used for each spectrum. For a multilayer, this leads to many parameters: $5p+4$ parameters for a p -layer stack.

Certainly the key parameter of scattering is the correlation between interfaces. Indeed, if we have uncorrelated surfaces, scattering is always increasing with an increasing number of layers and decreasing in the case of identical surfaces. We will have interferences between the scattering waves, and providing that these interferences are destructive, we can reduce the scattering.

This phenomenon has been observed on a single layer and described as "antiscattering effect" and it is also the case of Fabry-Perot filters since we know that scattering can vary by a factor 100 according to the state of correlation between interfaces.

Usually, the correlation is assumed to be a constant value between zero and unity. In fact, we must consider a more realistic model ; for instance, we must admit that the surface defect at interface j is due to the total or partial reproduction of the defects of interface i added with residual roughness due to the grain size that characterizes the microstructure of the material. First we will consider here the model where the Fourier Transform of residual roughness is negligible in the range of spatial frequencies responsible for optical scattering, since we know that columnar microstructure of materials is not responsible for optical scattering. Anyway, we will first consider coatings produced on very rough substrates to be sure that the residual roughness will be negligible compared with the reproduction of substrate defects. Therefore the consequence is that the material acts as a linear filter on the interface and the correlation is the Fourier Transform of a filtering function characterizing the action of the material. The advantage of this model is that we have only few parameters since cross-correlation laws and roughness spectra are connected by the following relationship: $\gamma_{ii} = \gamma_{jj} |\alpha_{ij}|^2$

The scattered intensity is: $I(\theta) = \sum C_{ij} \alpha_{ij} \gamma_{jj}$

So, instead of $(5p+4)$, we now need only two parameters to predict scattering introduced by the multilayer. The roughness of the substrate is given by 4 parameters and can be measured before coating.

C_{ij} is given by theory (connected with the design)

γ_{jj} is the interface roughness and is deduced from the roughness spectrum of the substrate if the correlation law is given: $\gamma_{jj} = f(\gamma_s)$

γ_s must be measured before coating and the correlation between i and j is given as a function of two filtering functions that characterize the two materials H and L of the stack:

$$\alpha_{ij} = f(\alpha_{i,i+1}, \dots, \alpha_{j-1,j})$$

With two alternate materials, we write:

$$\alpha_{2k,2k+1} = \alpha_H(\sigma)$$

and

$$\alpha_{2k+1,2k+2} = \alpha_L(\sigma)$$

which are the two functions to be determined for prediction of scattering.

Moreover, if we consider the material microstructure, it is obvious that large period defects are perfectly reproduced ($\alpha(\sigma) \equiv 1$) while small period defects are only partially reproduced. Practically, we can consider that $\alpha(\sigma)$ will behave as a low-pass filter.

Briefly, provided that the substrate was measured before coating, prediction of scattering for a p-layer stack requires only the knowledge of two cut-off frequencies σ_H and σ_L . Figure 25 concerns a layer of index $n = 2.3$; it shows an example calculated of the scattering curve in the case of normal incidence illumination, for wavelength $0.6 \mu\text{m}$ and for a series of cut-off frequencies from $\sigma_c = 1 \mu\text{m}^{-1}$ to $\sigma_c = \infty$.

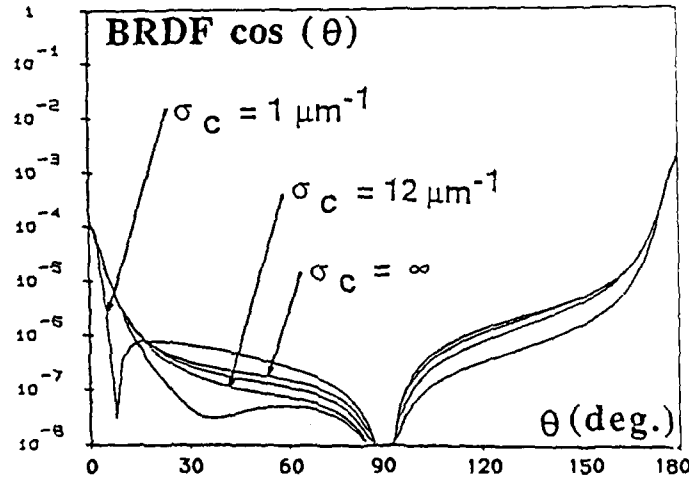


Figure 25:

Layer of index 2.3, optical thickness $\lambda/2$ for $\lambda = 0.6 \mu\text{m}$. Scattering curves calculated with different values of cut off frequency. $\sigma_c = \infty$ corresponds to a perfect correlation between the two interfaces of the layer.

To go further in our investigation, we can use the maps of anisotropy before and after coating. It is possible to work with an angular autocorrelation function and to demonstrate how the isotropy degree depends on spatial frequency.

The process of investigation of optical microroughness with the fit between prediction and experiment is summarized in figure 26.

In this presentation, we will show some results concerning the study of the mean plane section of angular scattering on a particular design.

With the Thin Film technical Group of OSA (meeting on October 16, 1989) we have presented the results of an experiment that gathers works done by several laboratories.

According to the theory of scattering in multilayers (Claude Amra - Marseille), one can determine the correlation of interface roughness in multilayer by a simple test. The test consists in measuring the scattering of a design composed of alternating high and low index layers at the wavelength where the layers are one halfwave thick. Four laboratories (Bazers, OCLI, Spectra Physics, OJAI) have prepared coatings of design: Glass 2H 2L 2H for 633 nm and have sent them to Marseille for examination. Each laboratory used a different deposition process or material combination.

The curves (figure 27) show how the scattering curve is theoretically a function of the value of the correlation coefficient α between the interfaces of this stack. If we compare these curves with the angular scattering of the substrate, we can also demonstrate that the angular scattering of the substrate before coating is very close from the angular scattering after coating if the surfaces are perfectly correlated (only a slight difference at large angles θ).

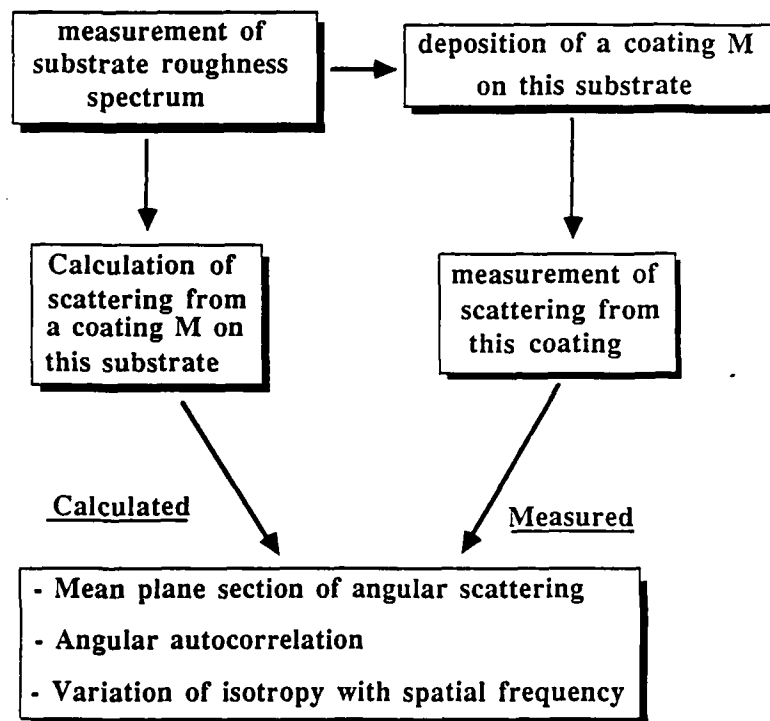
The ratio η of global scattering after coating to global scattering before coating is, for a roughness of 0.5 nm.

$$\eta = \frac{7.0 \text{ ppm}}{6.6 \text{ ppm}} = 1.06 \text{ for } \alpha = 1 \qquad \eta = \frac{186 \text{ ppm}}{6.6 \text{ ppm}} = 28.2 \text{ for } \alpha = 0$$

Table V gives the values D of scattering losses measured for all coatings together with the ratio $\eta = \frac{D(\text{after coating})}{D(\text{before coating})}$. The asterisk (*) indicates that the corresponding sample was kept uncoated. It appears from this table that all techniques lead to good correlation: η is much lower than the value 28 calculated for uncorrelated surfaces.

The measured angular scattering for the 4 samples are given before and after coating on figures 28, 29, 30, 31. We can see that the correlation is not completely perfect for the coatings since the two curves before and after coating are not superimposed.

Investigation of optical microroughness



and complementary information with Al layer technique

Figure 26:

Optimum approach for progress in study of optical microroughness.

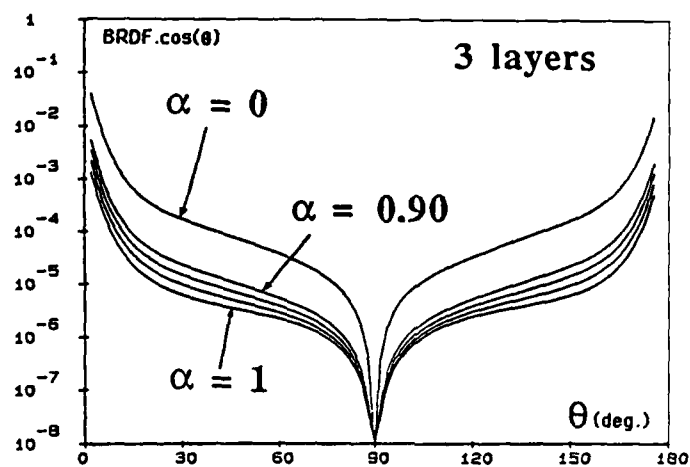


Figure 27:

Glass 2H 2L 2H for 633 nm. Scattering diagrams calculated for different values of the correlation coefficient α between interfaces.

	Technique	Materials	re-cleaning	Scattering D(ppm) from bare subst.			scattering D from 2H2L2H (ppm)	η
				N°	1st clean	2nd clean		
Spectra- ϕ	React-evap.	TiO ₂ /SiO ₂	Y	30	7.0		10.2	1.46
				35	6.0		9.5	1.58
				37*	6.6	6.0		
OCLI	Plasma Pl.	ZrO ₂ /SiO ₂	Y	13*	7.7	7.4		
				15	7.3		35.5	4.86
				17	6.1		25.7	4.21
Balzers	Ion pl.	Ta ₂ O ₅ /SiO ₂	Y	02*	6.5	5.5		
				03	6.2		8.4	1.35
				08	?		9.8	
OJAI	IBS	TiO ₂ /SiO ₂	N	21	6.9		12.6	1.83
				22	6.9		11.0	1.59

Table V:

Results obtained on the OSA samples. D is given before and after coating.

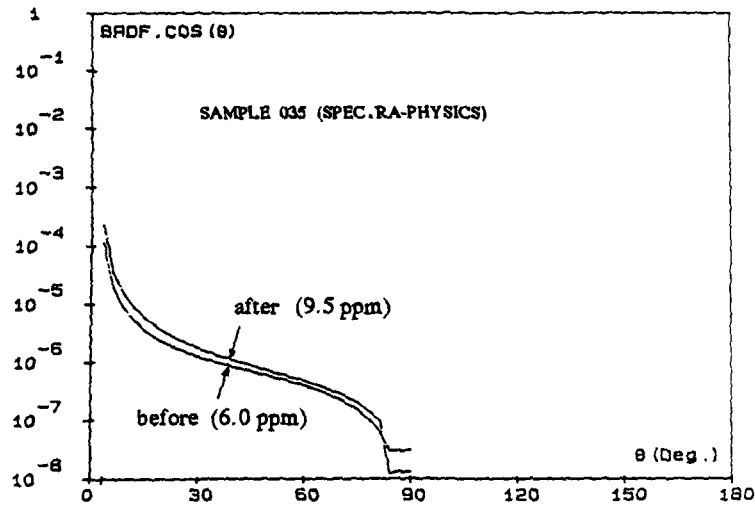


Figure 28:

Measured scattering diagrams before and after coating 2H 2L 2H
Coating manufactured by Spectra Physics - Global scattering losses are given on the curves

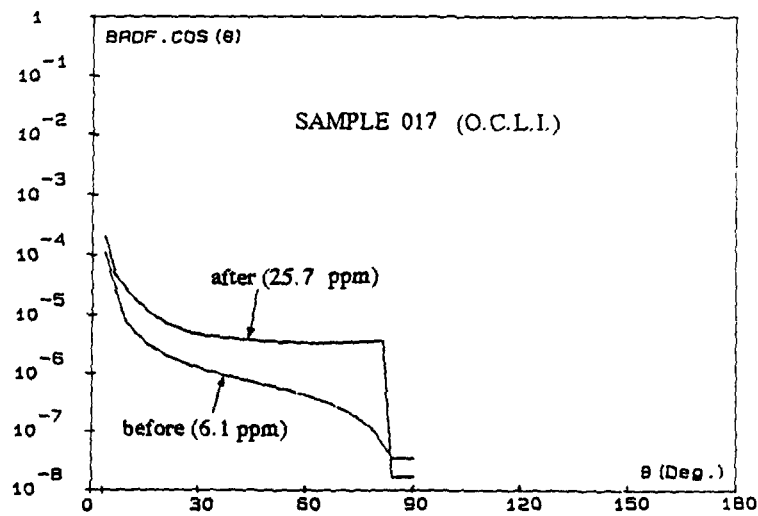


Figure 29:

Measured scattering diagrams before and after coating 2H 2L 2H
Coating manufactured by O.C.L.I. - Global scattering losses are given on the curves

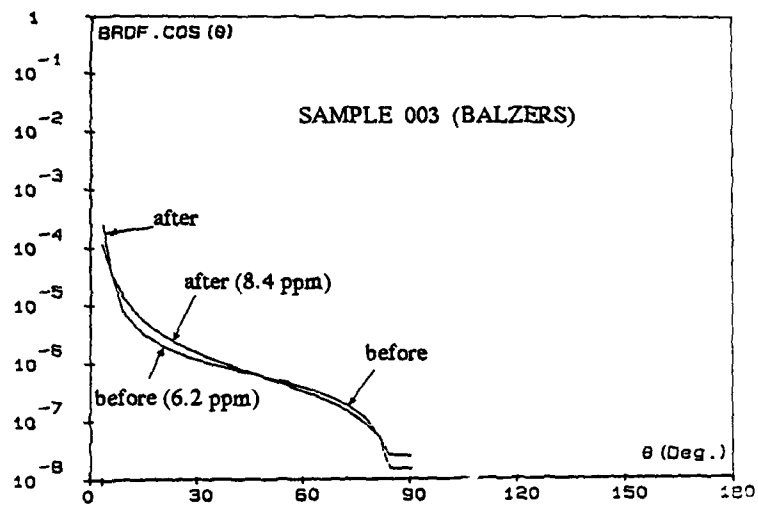


Figure 30:

Measured scattering diagrams before and after coating 2H 2L 2H
Coating manufactured by Balzers - Global scattering losses are given on the curves

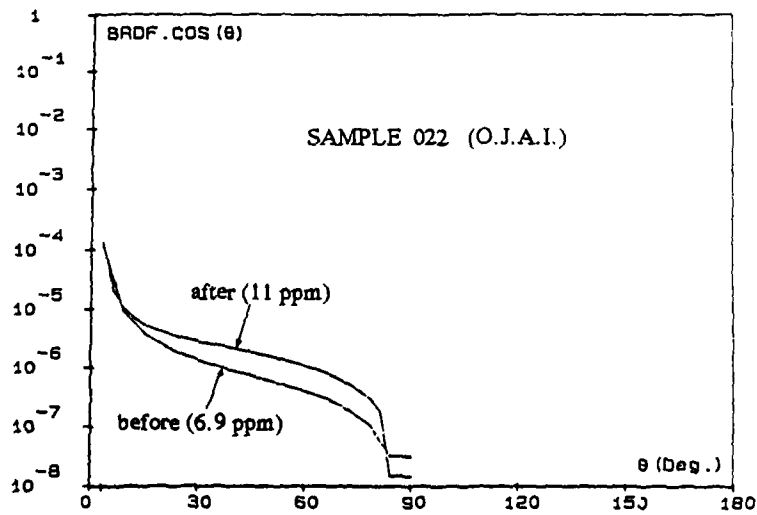


Figure 31:

Measured scattering diagrams before and after coating 2H 2L 2H
Coating manufactured by OJAI - Global scattering losses are given on the curves

For the coatings of OSA experiments, we can explain the better values of η by a correlation of 0.990 (for Balzers sample 003), of 0.986 (for Spectra Physics sample 030), of 0.981 (for OJAI sample 022) and of 0.885 (for OCLI sample 017).

Some complementary experiments have been performed in our Laboratory for a better understanding of this problem. We used $\text{TiO}_2\text{-SiO}_2$ layers produced by Ion Assisted Deposition. The different figures 32 show that the agreement between the angular curves before and after coating depends strongly of the roughness of the bare substrate: it is obvious that the correlation is easy to obtain with rough substrates. Moreover, whatever the substrate roughness, we observe a perfect correlation at small angles and the disagreement is obvious at large angles.

To give a more complete conclusion on this work, we have been induced to study the consequences of thickness errors on the layers of the stack: 2H 2L 2H. We will present later the measurements of reflectance versus wavelength performed on the OSA coatings; the centering on $\lambda_0 = 0.633 \mu\text{m}$ is not always perfect. We try to apply synthesis methods for determining the effective designs of the multilayers and we will then have the possibility to study theoretically the consequences of these thickness errors on angular scattering curve.

This whole work must be the subject of a publication in common with Marseille and OCLI (J. Apfel) and the coating manufacturers. The main question which will be interesting for us in the future is the law of dependence of scattering with wavelength. This law depends strongly on the correlation between interfaces and it should be a further verification of our conclusion.

Publications and participation in conferences

The grant AFOSR-88-0139 is of considerable help to link the laboratory of Marseilles with Macleod's group and allowed the participation to conferences in the United States.

C. Amra, M. Commandré and E. Pelletier attended the OSA Conference in November 88. 2 papers were presented.

C. Amra and E. Pelletier participated in the Boulder Damage Symposium - Nov. 88 and Nov. 89 - 2 papers were presented.

C. Amra and E. Pelletier participated in the OSA Conference - Nov. 89 in Orlando. One paper and Technical Meeting group.

One post-doc. (C. Hickey) and one student (R. Sprague) from Tucson spent two years in Marseille (1988 - 1990). R. Sprague's thesis will be a work common to Tucson and Marseille (April 90).

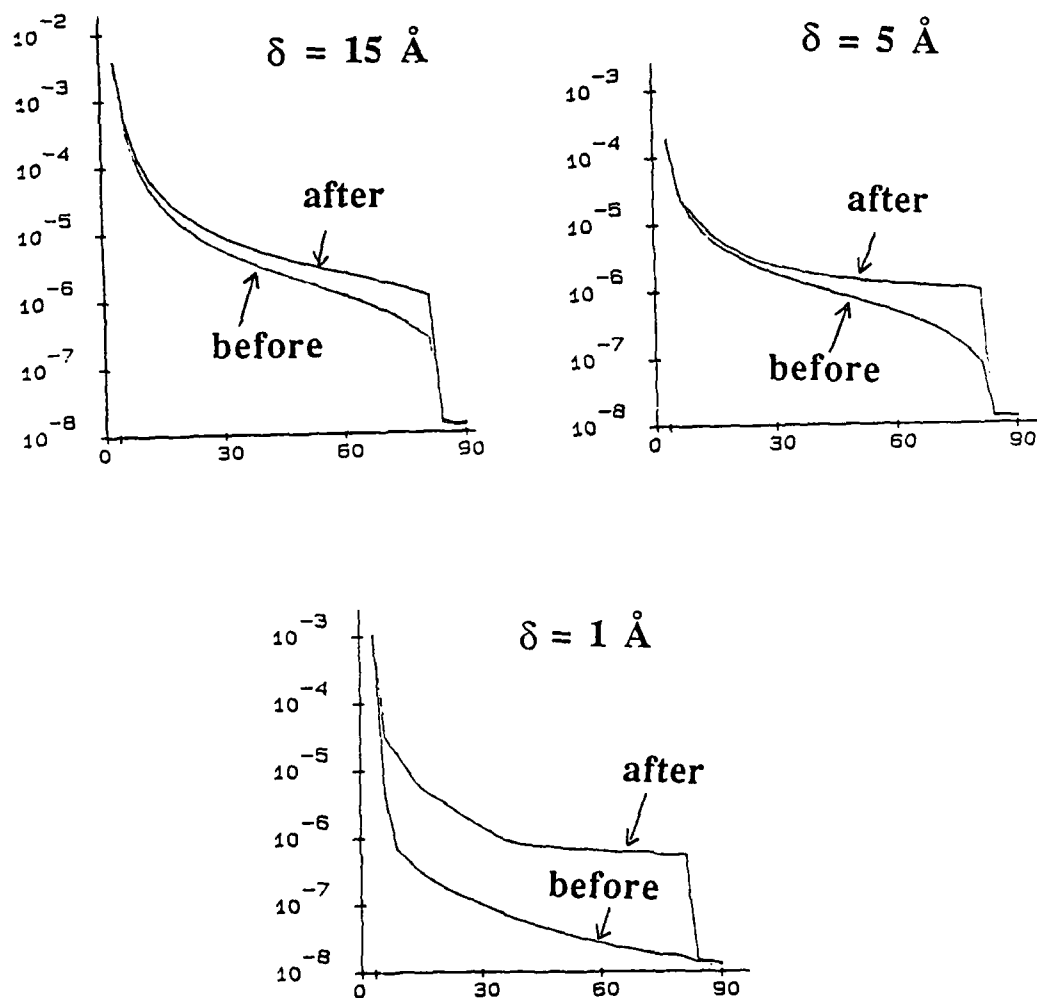


figure 32:

Measured scattering diagrams, before and after coating 2H 2L 2H on the three samples produced in Marseilles Laboratory. The state of correlation between interfaces strongly depends on the roughness δ of the sample considered.

Further information

Ion Assisted Deposition and Modeling

Many of the above topics will be found in the following dissertations:

- C.K. Hwangbo, "Optical thin films prepared by ion-assisted and ultrasound-assisted deposition."
- L. Lingg, "Study of thin films of the lanthanide trifluorides with emphasis on the optical properties." (Final text in preparation).
- John Lehan, "Microstructural analysis of thin films by Rutherford Backscattering Spectrometry, electron diffraction and spectrophotometry." (In preparation).
- Rober Sargent ..., "The modeling of thin film growth (tentative title)." (In preparation).

Recent publications

- C.K. Hwangbo, L.J. Lingg, J.P. Lehan, H.A. Macleod, J.L. Makous and S.Y. Kim, "Ion-assisted deposition of thermally evaporated Ag and Al films," *Applied Optics*, **28**, 2769-2778, (1989)
- C.K. Hwangbo, L.J. Lingg, J.P. Lehan, H.A. Macleod and F. Suits, "Reactive ion-assisted deposition of aluminum oxynitride thin films," *Applied Optics*, **28**, 2779-2784 (1989)
- J.D. Targove, L.J. Lingg, J.P. Lehan and H.A. Macleod, "Effect of oxygen incorporation on the structure of ion-beam-assisted LaF₃ films," *Applied Optics*, **27**, 213-215 (1988)
- B.G. Bovard and H.A. Macleod, "Thermal model of a switching Fabry-Perot etalon," *Proc. SPIE*, **821**, 187-197 (1988)
- R.B. Sargent and H.A. Macleod, "Computer simulation of the growth of two-element films," *Proc. SPIE*, **821**, 113-119 (1988)
- R.B. Sargent, D.Y. Song and H.A. Macleod, "Computer simulation of substrate defect propagation in thin films," *Proc. SPIE*, **821**, 133-140 (1988)
- J.D. Targove, B.G. Bovard, L.J. Lingg and H.A. Macleod, "Densification of aluminum fluoride thin films by ion-assisted deposition," *Thin Solid Films*, **159**, L57-L59 (1988)
- B.G. Bovard and H.A. Macleod, "Nonlinear behavior of optical coatings subjected to intense laser irradiation," *J. Mod. Opt.*, **35**, 1151-1168 (1988)
- J.D. Targove and H.A. Macleod, "Verification of momentum transfer as the dominant densifying mechanism in ion-assisted deposition," *Applied Optics*, **27**, 3779-3781 (1988)
- C.K. Hwangbo, "Optical thin films prepared by ion-assisted and ultrasound-assisted deposition." PhD, University of Arizona, 1988
- P.J. Martin, R.P. Netterfield and W.G. Santy, *J. Appl. Phys.*, **55**, 235 (1984)
- H.K. Pulker, *Coatings on Glass*, Elsevier, Amsterdam (1984)
- J.P. Borgogno, B. Lazarides, E. Pelletier, "Automatic determination of the optical constants of inhomogeneous thin films," *Applied Optics*, **21**, 4020 (1982)
- M. Commandré, E. Pelletier, "Measurements of absorption losses in TiO₂ films by collinear photothermal deflection technique," Conf. presented at "OSA Annual Meeting", Santa Clara, California - Oct. 31 - Nov. 1, 1988 - Submitted to *Applied Optics*.

Photothermal Deflection Spectroscopy

- A.C. Boccara and D. Fournier, W. Jackson and N.M. Amer, "Sensitive photothermal deflection technique for measuring absorption in optically thin media," *Optics letters*, **5**, 377 (1980)
- W.B. Jackson, N.M. Amer, A.C. Boccara and D. Fournier, "Photothermal deflection spectroscopy and detection," *Appl. Opt.*, **20**, 1333 (1981)

- M. Commandré, L. Bertrand, G. Albrand, E. Pelletier, "Measurement of absorption losses of optical thin film components by Photothermal Deflection Spectroscopy," SPIE PROCEEDINGS, "Optical Components and Systems", 805, 128 (1987)
- J.P. Borgogno, B. Lazaridès, E. Pelletier, "Automatic determination of the optical constants of inhomogeneous thin films." - Applied Optics, 21, 4020 (1982)
- J.P. Borgogno, B. Lazaridès, P. Roche, "An improved method for the determination of the extinction coefficient of thin film materials," Thin Solid Films, 102, 209 (1983)
- C. Carniglia, chairperson; Optical Materials and Thin Films technical group meeting at the 1986 Optical Society of America Annual Meeting.(Unpublished)
U.J. Gibson, chairperson; Optical Materials and Thin Films technical group meeting at the 1987 Optical Society of America Annual Meeting.(Unpublished)
- J.M. Bennett, C. Carniglia, K.M. Guenther, E. Pelletier, et al., "Comparison of the properties of titanium dioxide films prepared using different techniques," To be published.
- H.A. Macleod, "Microstructure of Optical Thin Films," Proc. SPIE, 325, 21 (1982)
- H.A. Macleod, D. Richmond, "Moisture penetration patterns in thin films," Thin Solid Films, 37, 163 (1976)

Scattering

- C. Grèzes-Besset, R. Richier, E. Pelletier, "Layer uniformity obtained by vacuum evaporation. Application to Fabry-Perot filters.," Applied Optics, 28, 2960-2964(1989)
- A. S. Galerneau, A. Fornier, A. Hamel, "Mesure des taux de réjection élevés dans les filtres interférentiels. Application au démultiplexage optique," Ann. Télécommun., 43, 123-134 (1988)
- P. Roche, C. Amra, E. Pelletier, "Measurement of scattering distribution for characterization of the roughness of coated or uncoated substrates," SPIE Proceedings, Thin film Technologies II, 652, 256-263, (1986)
- B. Schmitt, J.P. Borgogno, G. Albrand and E. Pelletier, "In situ and air index measurements: influence of the deposition parameters on the shift of $\text{TiO}_2/\text{SiO}_2$ Fabry-Perot filters," Appl. Opt. 25, 3909 (1986)
- J.P. Borgogno, F. Flory, P. Roche, B. Schmitt, G. Albrand, E. Pelletier, H.A. Macleod, "Refractive index and inhomogeneity of thin films.," Appl. Opt., 23, 3567-3570 (1984)
- E. Pelletier, F. Flory, Y. Hu, "Optical characterization of thin films by guided waves. Applied Optics, 28, 2918-2924 (1989)
- C. Grèzes-Besset, C. Amra, B. Cousin, G. Otrio, E. Pelletier, R. Richier, "Etude de la diaphonie d'un système de démultiplexage par filtres interférentiels. Conséquences de la diffusion de la lumière par les irrégularités des surfaces optiques," Ann. Télécommun., 43, 135-141 (1988)
- C. Amra C. Grèzes-Besset, P. Roche, E. Pelletier, "Description of a scattering apparatus- Application to the problems of characterization of opaque surfaces," Applied Optics, 28, 2723-2730(1989)
- J.M. Elson, "Angle resolved light scattering from composite optical surfaces," Proc. Soc. Photo. Opt. Instrum. Eng. 240, 296 (1980)
- P. Bousquet, F. Flory, P. Roche, "Scattering from multilayer thin films: theory and experiment.," J. Opt. Soc. Am., 71, 1115-1123 (1981)
- C. Amra, P. Bousquet, "Scattering from surfaces and multilayer coatings: recent advances for a better investigation of experiment", SPIE Proceedings, vol 1009 "Surface Measurement and Characterization" p. 82-97 (1988)
- F.E. Nicodemus, "Directional Reflectance and Emissivity of an opaque Surface," Appl. Opt., 4, 767-773 (1965)
- C. Amra, G. Albrand and P. Roche, "Theory and application of antiscattering single layers; antiscattering antireflection coatings," Appl. Opt. 25, 2695-3915 (1986)

- P. Giacomo, "Les couches réfléchissantes multidiélectriques appliquées à l'interférométrie de Fabry-Perot. Etude théorique et expérimentale des couches réelles," Thèse de Doctorat d'Etat, Faculté des sciences de Paris (1955). *Rev. Opt.*, **35**, 317-354 et 442-467 (1956)
- P. Roche, E. Pelletier, "Characterization of optical surfaces by measurement of scattering distribution," *App. Opt.*, **23**, 3561-3566 (1984)
- P. Croce, L. Prod'homme, "Ecart observé dans l'interprétation des indicatrices de diffusion optique par des théories vectorielles simples", *J. Optics*, **16**, 143-151 (1985)
- J.M. Bennett, "Scattering and surface evaluation techniques for the optics of the future," *Optics News*, July 1985
- J.P. Borgogno, E. Pelletier, "Determination of the extinction coefficient of dielectric thin films from spectrophotometric measurements," *Applied Optics*, **28**, 2895-2901 (1989)
- C. Amra, "Scattering distribution from multilayer mirrors - Theoretical research of a design for minimum losses," *Laser induced damage in optical materials* **752**, 594-602 (1986)
- J.H. Apfel, "Optical coating design with reduced electric field intensity," *Appl. Opt.*, **16**, 1880-1885 (1977)
- C. Amra, "Minimizing scattering in multilayers: technique for searching optimal realization conditions," *"Laser induced damage in optical materials"*, **756**, 265-271 (1987)
- F. Flory, G. Albrand, C. Montelymard, E. Pelletier, "Optical study of the growth of Ta₂O₅ and SiO₂ layers obtained by Ion Assisted Deposition," *SPIE Proceedings, Thin Film Technologies II*, **652**, 248-253, (1986)
- C. Amra, C. Grèzes-Besset, E. Pelletier, "Investigation of the Origin of Microroughness in Multilayer Coatings through Variation in the degree of Isotropy," *Conf. presented at "OSA Annual Meeting"*, Orlando, Florida - Oct. 15-20, 1989
- C. Amra, "Scattering characterization of materials in thin film form," *Conf. presented at "21st Annual Boulder Damage Symposium"* - Nov. 1-3, 1989, Boulder, Colorado, To be published in *"Laser induced damage in optical materials"*

Annexe I

Some recent publications

The Journal of Applied Optics (15 July 1989 issue) gives 9 papers of the laboratories of Tucson and Marseilles. We give here two of the articles of Macleod's group.

Ion assisted deposition of thermally evaporated Ag and Al films

Chang Kwon Hwangbo, Linda J. Lingg, John P. Lehan, H. Angus Macleod, John L. Makous, and Sang Yeol Kim

Optical, electrical, and microstructural effects of Ar-ion bombardment and Ar incorporation on thermally evaporated Ag and Al thin films are investigated. The results show that as the momentum supplied to the growing films by the bombarding ions per arriving metal atom increases, the refractive index at 632.8 nm increases and the extinction coefficient decreases, lattice spacing expands, grain size decreases, electrical resistivity increases, and trapped Ar increases slightly. In Ag films, stress reverses from tensile to compressive and in Al films compressive stress increases. In the Al films the change in optical constants can be explained by the variation in void volume. The reversal of stress from tensile to compressive in Ag films requires a threshold level of momentum. The increase in electrical resistivity is related to the decrease in grain size and increase in trapped Ar in both types of film. Many of these properties correlate well with the momentum transferred, suggesting that the momentum is an important physical parameter in describing the influence of ion beam on growing thin films and determining the characteristics of thin metal films prepared by ion assisted deposition.

I. Introduction

Ion assisted deposition (IAD) is known to produce thin films with characteristics that conventionally deposited thin films do not have.¹⁻³ For example, the IAD of dielectric thin films has shown that it increases the packing density and refractive index, reduces the moisture adsorption, and improves the adhesion in certain material dependent conditions.⁴⁻⁹ IAD can also alter the stoichiometry and crystallinity of dielectric thin films.^{10,11} For metal thin films, IAD enhanced adhesion in Au, Ag, and Al films on glass substrates.¹²⁻¹⁵ IAD of Cr thin films resulted in an increase in reflectance and reversal of stress from tensile to compressive when the ion flux exceeded a critical value.¹⁶ In addition, the nonbulklike optical density, reduction of optical scatter, and control of microstructure in Cu films under ion bombardment were reported.¹⁷⁻¹⁹

The correlation of optical properties and microstructure of IAD thin films with ion beam parameters is very important because it provides insights for understanding and producing these films. It is known that the ion energy and current density are two ion beam parameters which alter the microstructure of naturally growing thin films and their optical properties. It is not clear, however, what physical parameter (energy, momentum, or some function of the two) of the ion beam affects the growth of thin films.¹ Parmigiani *et al.*²⁰ related the normalized energy, defined as the energy delivered by the bombarding ions per arriving metal atom, to the optical, electrical, and microstructural changes of metal films in dual ion beam sputtering.²¹ On the other hand, Windischmann²² derived a model, based on the linear cascade theory of forward scattering, so that the intrinsic stress of ion beam sputtered films depends on the imparted momentum rather than energy.

In this paper, we investigate the optical, electrical, and microstructural effects of Ar-ion bombardment and Ar incorporation on thermally evaporated Ag and Al thin films. These effects and incorporated Ar are presented in terms of the momentum supplied to the growing thin film by the bombarding ions per arriving metal atom. We define the momentum P normalized by the Ar mass as $\gamma\sqrt{E}$, where γ is the (Ar ion)-to-(metal atom) arrival rate at the substrate and E is the Ar-ion energy.

II. Deposition Conditions

Ag was evaporated from a Mo boat, and Al was electron beam evaporated from an intermetallic cruci-

John Makous was with the University of Arizona, Physics Department, Tucson, Arizona 85721 when this work was done and is now with U.S. Naval Research Laboratory, Washington, DC 20375-5000. When this work was done Sang Yeol Kim was with Pennsylvania State University, Materials Research Laboratory, University Park, Pennsylvania 16802 and is now with Aju University, Physics Department, Suwon, Korea. The other authors are with University of Arizona, Optical Sciences Center, Tucson, Arizona 85721.

Received 8 August 1988.

0003-6935/89/142769-10\$02.00/0.

© 1989 Optical Society of America.

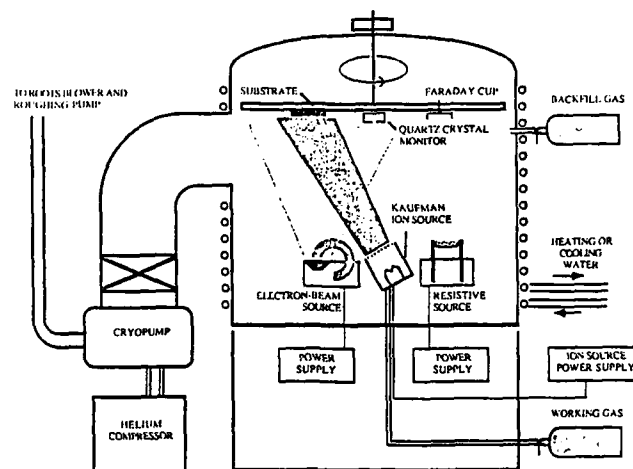


Fig. 1. Experimental configuration of a Balzers 760 coating plant.

ble in a Balzers 760 box coater, as shown in Fig. 1. The base pressure was 1×10^{-6} mbar. The chamber temperature was ambient, and its variation during a single layer deposition was $<5^\circ\text{C}$. The deposition rates of Ag and Al films were 0.5 and 1.0 nm/s, respectively, as measured by a quartz crystal oscillator. Prisms, glass slides, and graphite slabs were used as substrates for the various postdeposition measurements. Just prior to deposition, substrates were sputter cleaned *in vacuo* by the Ar-ion beam for 5–60 s, depending on the type of substrate used.

We employed a 3-cm aperture Kaufman hot-cathode ion source with Ar gas as the bombarding species. Ar gas was admitted through the ion gun until a pressure of 8×10^{-5} mbar in the chamber was obtained. The Ar-ion energies investigated were 200, 300, and 500 eV, while the Ar-ion current density was varied from 0 to $20 \mu\text{A}/\text{cm}^2$. These parameters resulted in the mass normalized momentum P being varied from 0 to $0.48 \sqrt{\text{eV}}$ for Ag films and 0 to $0.46 \sqrt{\text{eV}}$ for Al films, respectively. The non-IAD (conventional) thin film has zero P by definition.

III. Optical Measurements

A. Surface Plasmon Resonance

Optical constants at 632.8-nm wavelength and thickness of Ag and Al films were obtained using the surface plasmon resonance (SPR) technique.²³ In the Kretschmann configuration of the SPR, a thin metal film is deposited on the hypotenuse of a right angle prism.²⁴ When the angle of incidence of a TM wave inside the prism is larger than the critical angle, the incident wave is totally reflected and an evanescent wave is absorbed by the metal film. At a certain incident angle and film thickness, the component of the wave vector of the electric field parallel to the film

plane equals that of surface plasmon propagating along the metal-air interface and is thus coupled to this surface plasmon mode. When this occurs, the energy of the incident wave is absorbed by the surface plasmon, and no wave is reflected by the metal film. This results in the reflectance showing a sharp resonant minimum as the incident angle varies above the critical angle. The resonant angle and thickness which yields zero reflectance depend on the optical constants of the metal film.²⁵ Optimization software employing admittance matching between the incident medium and metal film was used to calculate the resonant angle and thickness.²⁶ Optimum thicknesses of ~ 50 and 15 nm were chosen for Ag and Al films, respectively. From the measured reflectance with respect to the incident angle, the optical constants and thickness were calculated using a nonlinear least-squares method.²⁷ Reflectance calculated from the optical constants and thickness found by the program was in good agreement with the experimental reflectance profile. Measurements were performed within 5 h after the films were taken out of the vacuum chamber because the SPR technique is sensitive to the oxidation of the metal-air interface.²⁸

Refractive index n and extinction coefficient k of Ag films at 632.8 nm are plotted in Fig. 2 in terms of P . As P increases, n increases and k decreases. Reflectance of Ag films of 100-nm thickness at normal incidence is calculated from these optical constants and listed in Table I. At the highest P ($0.48 \sqrt{\text{eV}}$), reflectance drops by 2.5% compared to the non-IAD film. In other words, IAD Ag films become lossy when bombarded with Ar ions.

The n and k of Al films at 632.8 nm shown in Fig. 3 are scattered from a line. Reflectance of Al films of 100-nm thickness at normal incidence is also listed in Table I. When P is small, reflectance does not change much from that of non-IAD film. However, when P

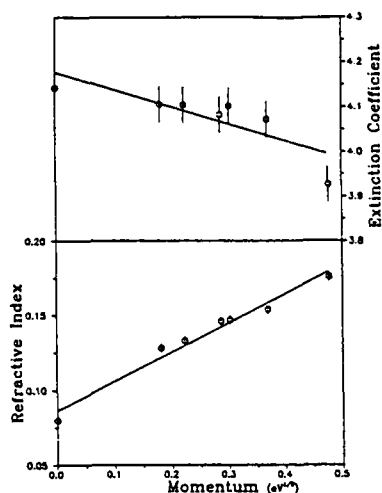


Fig. 2. Refractive index and extinction coefficient at 632.8 nm of Ag films measured by the SPR plotted as a function of P.

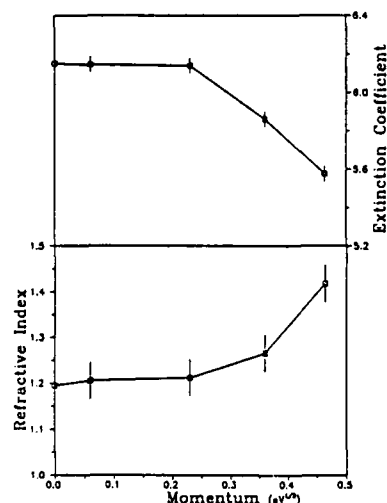


Fig. 3. Refractive index and extinction coefficient at 632.8 nm of Al films measured by the SPR plotted as a function of P.

Table 1. Reflectance of Ag and Al Films of 100-nm Thickness at 632.8 nm at Normal Incidence Is Calculated from the Optical Constants Obtained from the SPR Measurements

Ag films		Al films	
P (eV)	R (%)	P (eV)	R (%)
0	98.3	0	88.8
0.18	97.1	0.06	88.7
0.22	97.0	0.23	88.6
0.29	96.7	0.36	87.2
0.30	96.7	0.46	84.6
0.37	96.5		
0.48	95.8		

exceeds $0.23 \sqrt{eV}$, the reflectance of IAD films decreases.

B. Spectroscopic Ellipsometry

Recently, spectroscopic ellipsometry (SE) has been used as a nondestructive tool to depth profile multilayer structures and void fractions in thin films in addition to its traditional role, measuring the optical constants, dispersion, and thickness of thin films. The void fraction in Au and amorphous IAD Ge thin films and depth profiling Si, ZnS, MgO, and ThF₄ thin films have recently been studied.²⁹⁻³³ In this work SE was used to measure the optical constants, dispersion, and thickness of metal thin films on glass substrates at an angle of incidence of 70° in the 1.5–4.5-eV spectral range in steps of 0.05 eV. The void fraction in Al films and its oxide layer thickness were calculated by applying the Bruggeman effective medium approximation and linear regression analysis to the SE data.^{34,35}

Pseudorefractive index n_p and pseudoeextinction coefficient k_p , the effective refractive index and effective extinction coefficient of the film-substrate assembly, for some Ag films are plotted in Figs. 4(a) and (b) in terms of photon energy. n_p of the IAD Ag films is larger than that of the non-IAD Ag film below the plasma frequency near 3.8 eV (at which n_p equals k_p).³⁶ But in the 2.5–3.0-eV spectral region, n_p of the IAD films is almost the same as the non-IAD film. In the interband transitions above the plasma frequency, n_p of the IAD films is lower than that of the non-IAD film. k_p of the IAD Ag films is smaller than that of the non-IAD film except in the vicinity of the plasma frequency. Also, the high P film shows larger n_p and smaller k_p than the low P film, which is consistent with the SPR results. Reflectance of Ag films at normal incidence is calculated from n_p and k_p and plotted in Fig. 5. Reflectance of these IAD films drops by ~1% in the intraband transitions, while it drops by ~3% in the interband transitions. Around the plasma frequency, surprisingly, the reflectance (interband absorption) increases (decreases) by ~3% for IAD films.

n_p and k_p of Al films are plotted in Figs. 6(a) and (b). Near the 1.5-eV interband absorption, n_p of the IAD Al films is smaller than that of the non-IAD Al film. In the rest of the measured spectral region (from ~1.8 to 4.5 eV), the high P film shows larger n_p than the non-IAD film, while the small P film behaves like the non-IAD film. k_p of the IAD films is smaller than that of the non-IAD film in the whole measured spectral region. Reflectance calculated from n_p and k_p at normal incidence for 100 nm thick films is plotted in Fig. 7. Reflectance of the IAD films drops by ~2% except at the 1.5-eV interband absorption.

Optical properties of metal thin films in the spectral range of intraband transitions can be described phenomenologically by the Drude free-electron model.¹⁷ At near IR frequencies ($\omega \gg 1/\tau$),³⁶ the real and imaginary parts of complex dielectric constants can be written as follows:

$$\epsilon_1 \approx \epsilon_0 - \omega_p^2/\omega^2 = \epsilon_0 - E_p^2/E^2, \quad (1)$$

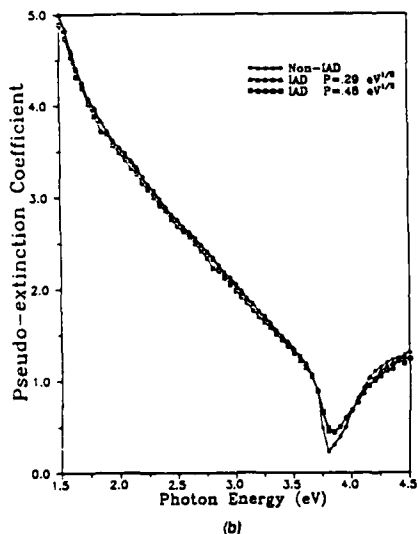
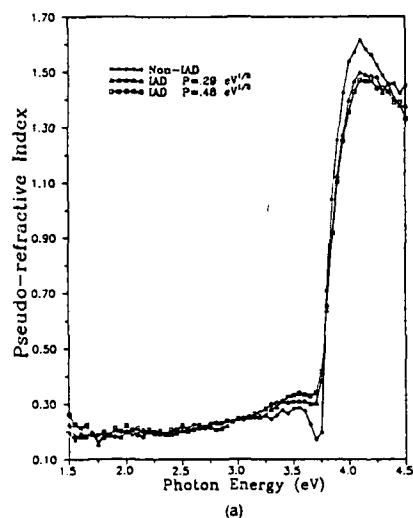


Fig. 4. (a) Pseudorefractive index and (b) pseudoextinction coefficient of Ag films measured by the SE plotted as a function of incident photon energy.

$$\epsilon_2 \approx \omega_p^2 / (\omega^2 \tau), \quad (2)$$

where ϵ_0 represents core interband transitions, ω_p is the plasma angular frequency for intraband transitions, τ is the intraband relaxation time, and ω is the angular frequency of the light. E_p and E are the energies of the plasma frequency and incident wave, respectively. The intraband plasma frequency of the conduction electrons ω_p is given by

$$\omega_p = \sqrt{4\pi N e^2 / m}, \quad (3)$$

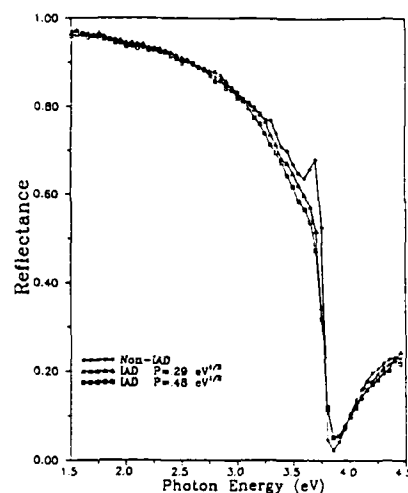


Fig. 5. Reflectance of Ag films calculated from the pseudorefractive index and pseudoextinction coefficient plotted as a function of incident photon energy.

where N is the effective number density of electrons participating in the intraband transitions, and m and e are the free-electron mass and charge, respectively. Also, the dc conductivity σ in the Drude free-electron model is expressed by

$$\sigma = \omega_p^2 \tau / 4\pi. \quad (4)$$

Using Eq. (1), we can determine ω_p of a metal film from the slope of a plot of $-\epsilon_1$ vs $(1/E^2)$. From ω_p and Eq. (3), N can be obtained.

The plots of $-\epsilon_1$ vs $(1/E^2)$ calculated from the pseudodielectric constants for Ag and Al films in the intraband transitions are shown in Figs. 8(a) and (b), respectively. E_p of the IAD Ag film at $P = 0.48 \text{ eV}/\mu$ is 7.6 eV, while that of the non-IAD film is 7.7 eV. For the Al films, E_p drops from 10.7 eV of the non-IAD film to 10.1 eV of the IAD film at $P = 0.46 \text{ eV}/\mu$. The slope for the IAD films decreases as P increases. The decrease of E_p means a reduction in N , which has to do with changes in the microstructure of the metal film.^{20,29} The fraction of voids in the Al films is calculated by using the effective medium approximation and linear regression analysis,^{34,35} and the results are shown in Table II. Because the Al films had been exposed to the atmosphere for a few months before the SE measurement was performed, a thin Al_2O_3 layer on top of the Al film was taken into account.³⁸ Since the 100-nm thickness of Al film is much larger than the skin depth of Al ($\sim 10 \text{ nm}$), the incident wave does not see the glass substrate. Hence bulk Al plus voids is assumed as the substrate. In Fig. 9, the measured dielectric constants of the non-IAD Al film are in good agreement with those calculated from the data modeled in Table II. The fraction of voids increases as P increases, while the thickness of the oxide layer does not seem to correlate with P .

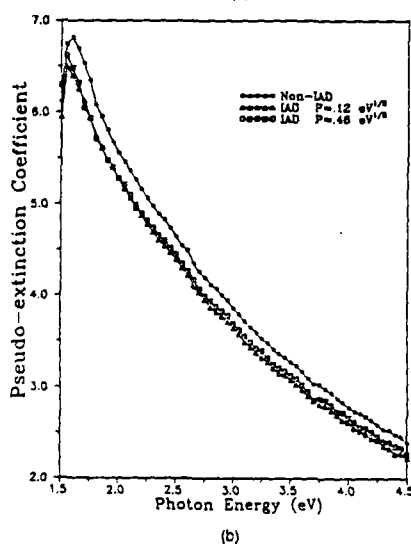
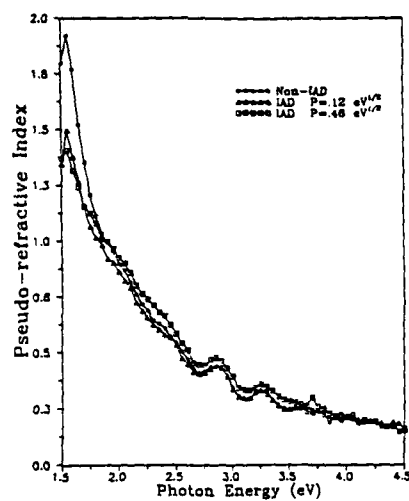


Fig. 6. (a) Pseudo-refractive index and (b) pseudoextinction coefficient of Al films measured by the SE plotted as a function of incident photon energy.

Analogous to the reduction of interband absorption in the IAD Ag films, the 1.5-eV interband absorption of the IAD Al films decreases. Interestingly, the 1.5-eV interband absorption in the Al films tends to disappear as P increases. Similar observations for Al films on cold substrates were reported by Bernland.³⁹ In his work, as the substrate temperature decreased from 198 to 25 K, the 1.5-eV interband absorption decreased and finally disappeared at 25 K. Possible explanations were a lack of [200] translational symmetry at 25 K and an intermediate state between a crystalline and

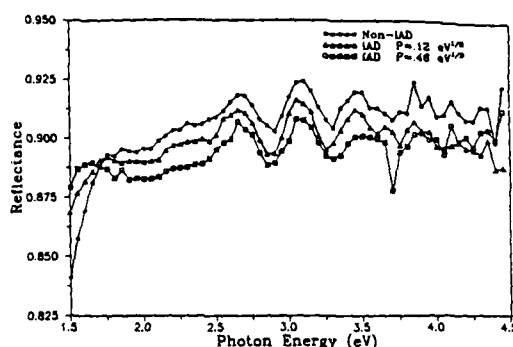


Fig. 7. Reflectance of Al films calculated from the pseudorefractive index and pseudoextinction coefficient plotted as a function of incident photon energy.

an amorphous state in the Al film on the cold substrate.^{39,40} When we investigated our Al films with x-ray diffraction (XRD), we did not observe a [200] orientation for both non-IAD and IAD Al films. Thus these explanations do not seem applicable to our films. If we assume the reflectance drop for the intraband transitions due to the fraction of voids is extended to the interband transitions, the reduction of the 1.5-eV interband absorption in the IAD Al films should also be due to these voids. Generally, the presence of voids in a thin film means that the characteristics of the film deviate from the bulk.^{29,34} Since the 1.5-eV interband absorption is a characteristic of the bulk, the presence of voids may influence it so that the 1.5-eV interband absorption decreases as the void fraction increases.

Given that the fraction of voids correlates well with P , we believe that the presence of voids in the film induced by Ar ions is an important factor which affects the effective number density of electrons in the intraband transitions and thus the optical constants.

IV. X-Ray Diffraction Analysis

A Bragg-Brentano x-ray diffractometer (XRD) was used to investigate the microstructure of polycrystalline Ag and Al films such as the strongest orientation, lattice spacing, and grain size. In addition, the strain and average stress in the film plane were calculated from the change in lattice spacing.

For Ag films, the (111) diffraction profile showed the strongest orientation. The intensity of (200) orientation is about one-seventh of the intensity of the (111) orientation. Thus we consider only the (111) orientation.

The situation for Al films was more complicated. Thin Al films (15 nm, the same thickness at which the optical constants of Al films were measured using the SPR technique) showed no diffraction peaks. Since these thin Al films had been exposed to the atmosphere for a while before the XRD measurements, an oxide layer comprising an average of 20–30 at. % of the film (as measured by the Rutherford backscattering spectrometry) formed at the air-film interface. It

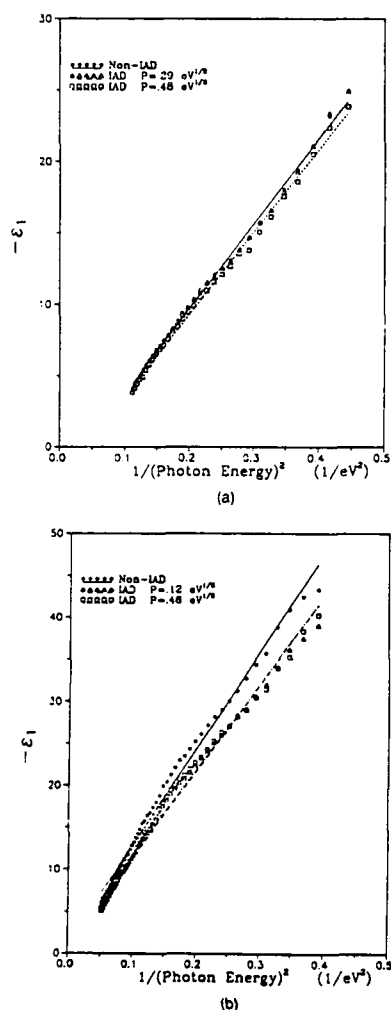


Fig. 8. $-\epsilon_1$ plotted as a function of $(1/E^2)$ for (a) Ag films and (b) Al films.

would be possible that the thin oxide layer disturbed the structure of very thin Al films and resulted in no diffraction profiles. For 100-nm thick Al films, the oxide layer comprised only an average of 2-3 at. % of the film, and thus a diffraction profile was observed but only the (111) orientation.

Table II. Fraction f of Voids in Al Films and the Thickness t of an Aluminum Oxide Layer are Simulated; the Thickness of Film is 100 nm

P (\sqrt{eV})	f (%)	t (nm)
0	12.4	3.3
0.12	18.2	3.5
0.46	20.7	2.4

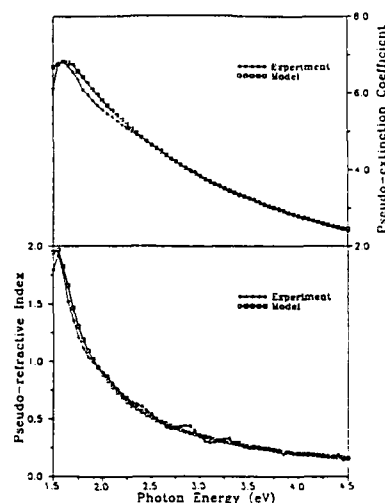


Fig. 9. Measured pseudorefractive index and pseudoextinction coefficient compared with those calculated from the model in Table II.

Lattice spacing d_{111} perpendicular to the film surface was calculated by the Bragg diffraction formula. The variation of d_{111} for Ag films is shown in Table III in terms of P . When P is small, d_{111} does not change significantly from that of the non-IAD Ag film. When P exceeds 0.2 \sqrt{eV} , however, d_{111} increases and levels off at ~ 360 Å, which is slightly larger than the value for Ag powder given by JCPDS¹¹ (2.359 Å). The results for Al films are shown in Table IV. In contrast to Ag films, d_{111} of IAD Al films keeps expanding slightly as P increases.

Table III. Ag Films; the Lattice Spacing (d_{111}), Strain ϵ_z Perpendicular to the Film Surface, and Strain ϵ_x in the Film Plane are Listed; the Thickness of Ag Films is 50 nm

P (\sqrt{eV})	d_{111} (Å)	ϵ_z (10^{-3})	ϵ_x (10^{-3})
0	2.354	-2.1200	2.40
0.18	2.354	-2.1200	2.40
0.22	2.358	-0.4240	0.48
0.29	2.360	0.4239	-4.80
0.30	2.360	0.4239	-4.80
0.37	2.360	0.4239	-4.80
0.48	2.360	0.4239	-4.80
Powder	2.359		

Table IV. Al Films; the Lattice Spacing d_{111} , Strain ϵ_z Perpendicular to the Film Surface, and Strain ϵ_x in the Film Plane are Listed; the Thickness of Al Films is 100 nm

P (\sqrt{eV})	d_{111} (Å)	ϵ_z (10^{-3})	ϵ_x (10^{-3})
0	2.343	2.14	2.01
0.06	2.344	2.57	2.42
0.12	2.344	2.57	2.42
0.29	2.345	2.99	2.82
0.46	2.346	3.42	3.22
Powder	2.338		

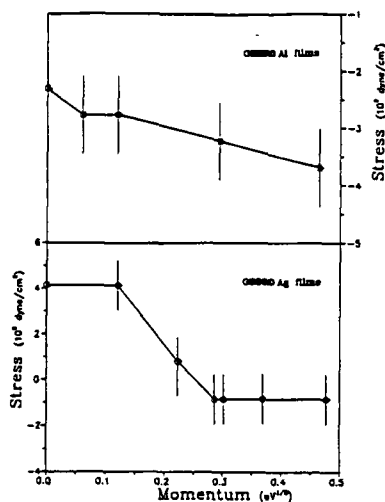


Fig. 10. Stress of Ag and Al Films as a function of P .

The change in lattice spacing is related to the strain ϵ_z perpendicular to the film plane as follows⁴²:

$$\epsilon_z = (d - d_0)/d_0$$

where d and d_0 are the strained and unstrained lattice spacings, respectively.

If we assume that the film plane is elastically isotropic and follow the developments of Vook and Witt⁴³ and Huang *et al.*,⁴⁴ the average stress σ_{av} and the strain ϵ_z in the film plane can be written by

$$\sigma_{av} = \epsilon_z / (2S_{11}),$$

$$\epsilon_z = \sigma_{av} (S_{11} + S_{12}),$$

where S'_{11} , S'_{12} , and S'_{33} are the elastic constants in the [111] orientation calculated by rotating the elastic constants for the [001] orientation.⁴⁵ The resulting ϵ_z and ϵ_x for Ag and Al films are listed in Tables III and IV, respectively. The average stress in the film plane is plotted in Fig. 10 as a function of P . Non-IAD and lightly bombarded IAD Ag films exhibit tensile stress, while IAD Ag films above $P = 0.2 \text{ eV}$ show a constant compressive stress value independent of P . Similar stress reversal has been reported in IAD Nb films,⁴⁶ dual ion beam sputtered Ag films,⁴⁴ and other sputtered metal films.^{47,48} In contrast to Ag films, the stress of IAD Al films is compressive throughout the entire P range and increases slightly with P .

It appears that the compressive stress of IAD Al films correlates well with P while the stress reversal from tensile to compressive for IAD Ag films requires a threshold value of P . Recently, Windischmann²² proposed a simple scaling law which relates the compressive stress for polycrystalline thin films prepared by ion beam sputtering with the momentum. Also, Hoffman and Gaertner¹⁶ demonstrated that the important

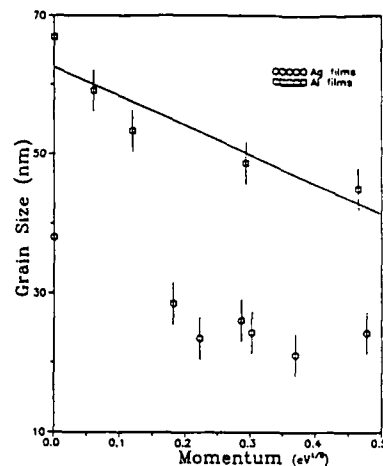


Fig. 11. Grain size of Ag and Al films as a function of P .

parameter for reversal of stress from tensile to compressive is related to the momentum transfer rather than energy by investigating evaporated Cr films bombarded with inert gases. Our results for stress analyses of IAD Ag and Al films appear to support Windischmann's scaling law and be in good agreement with Hoffman and Gaertner's results.

In addition to strain and stress, XRD allows us to examine the grain size in our films. Grain size L_{111} is given by the Scherrer equation,⁴² $L_{111} = \kappa \lambda / \beta \cos \theta$, where κ is a constant (taken to be 1), λ is 1.542 Å (CuK α radiation), θ is the Bragg diffraction angle, and β is the angular width of the pure diffraction profile on the 2θ scale. We corrected for instrumental broadening by assuming Gaussian profiles.⁴² As shown in Fig. 11, L_{111} of IAD Ag films is smaller than that of the non-IAD film, and it does not change significantly within the experimental error as P increases. On the other hand, L_{111} of IAD Al films decreases monotonically as P increases and at $P = 0.46 \text{ eV}$ L_{111} of the IAD Al film was only ~67% of that of the non-IAD film.

V. Electrical Resistivity Measurement

The electrical resistivity ρ of Ag and Al films at ambient temperature was measured by the van der Pauw four-point method.⁴⁹ With the appropriate correction factors, ρ of a flat metal film of arbitrary shape can be measured if the four contacts are at the circumference of the homogeneous film.⁵⁰ Resistivity for Ag and Al films is shown in Fig. 12 as a function of P . ρ of IAD films increases as P increases.

It is known that the electrical resistivity of a thin metal film is larger than that of the bulk and decreases as the thickness of the film increases. Fuchs developed a free-electron model to explain this phenomenon by considering the size effects of a thin film.⁵¹ In his theory, the thin film is assumed to be a homogeneous slab, and electrons are scattered not only in the

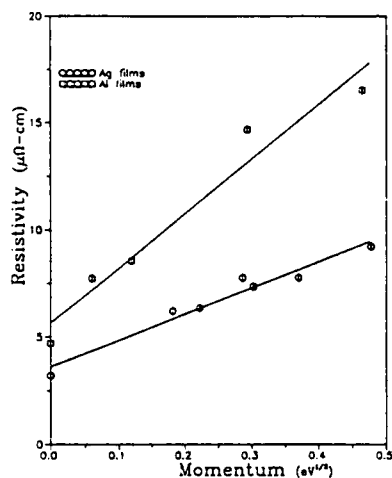


Fig. 12. Resistivity of Ag and Al films as a function of P.

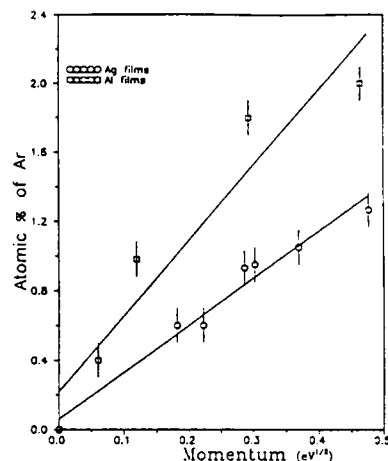


Fig. 13. Ar concentration in Ag and Al films as a function of P.

bulk but also by the smooth film surfaces. Real polycrystalline films, however, have different structures from the corresponding bulk. Modified models, based on Fuchs's theory and taking into account surface roughness,⁵² grain boundaries,⁵³ and charge carriers localization,⁵⁴ were later proposed. These also are not complete because the polycrystalline films studied have defects, dislocations, and impurities. With this in mind, Sambles⁵⁵ pointed out that extreme care must be taken in analyzing and interpreting the data of resistivity measurement.

Since Ar-ion bombardment on the growing Ag and Al films introduces microstructural changes, the pure Fuchs theory is not valid for our films. The rms surface roughness of our films was ~ 1 nm as measured by a noncontact surface profiler (WYKO TOPO 2D) and no significant difference in the surface roughness between non-IAD and IAD films was observed. We can thus exclude surface roughness as a factor in the differences in ρ between IAD and non-IAD films. Also, surface scattering due to the film thickness effects is relatively negligible because the grain size of Ag and Al films is smaller than the thicknesses (~ 50 and 100 nm for Ag and Al films, respectively), and so volume scattering dominates.

When Parmigiani *et al.*²⁰ applied Mayadas's⁵³ grain boundary scattering model to ion bombarded Ag films prepared by dual ion beam sputtering, it was found that the reflection coefficient R_g at the grain boundary depended on the deposition conditions. Since the Mayadas's model assumes a constant R_g for films of the same metal, the different R_g for each film was attributed to the different potential barrier at the grain boundaries due to the structural changes.

In this paper, we used Vancea's model⁵⁴: that the reduced effective number density of electrons N participating in the dc conductivity is a cause for the increase in resistivity of metal thin films. Vancea's

model seems to be an important factor for the increase in ρ of our films because we observed the reduction of N in the analysis of the real part of complex dielectric constants, which is related to the decrease in the dc conductivity of the free electron model by Eq. (4). Also, in Vancea's model, each grain acts as a potential well with the boundaries as barriers. Free electrons which pass through the potential barrier contribute to the dc conductivity. As the grain size decreases, the number of barriers increases, more electrons are trapped in grains, and the number of effective electrons participating in the dc conductivity decreases. This model thus relates the reduction of N and the decrease in grain size to the increase in ρ . Since the reduction of N implies an increase in void fraction as discussed in the SE section, the presence of a larger fraction of voids in IAD films seems to contribute to the increase in electric resistivity via Vancea's model.

VI. Rutherford Backscattering Spectrometry Analysis

The stoichiometry of our films was measured by Rutherford backscattering spectrometry (RBS). Incident singly ionized helium ($^4\text{He}^+$) ions with 1.892 MeV energy are backscattered by a thin film sample. The number of scattered ions per unit solid angle per incident ion is measured and compared with the known Rutherford scattering cross section. A simple calculation then yields the absolute number per unit area of each atomic species in the film.⁵⁶ The film stoichiometry thus can be measured very accurately. Graphite substrates were used because the Si and O peaks in a glass substrate would overlap the Al and O peaks in the films and thus reduce the accuracy.

The at. % of Ar in Ag and Al films is plotted in Fig. 13 in terms of P. Even though the amount of trapped Ar is < 2 at. %, it responds well to P in both Ag and Al films. The average at. % of oxygen in Ag films is $< 0.1\%$ and, therefore, negligible. Al films, on the other hand,

have most of their oxygen at the surface with the variation of average at. % of oxygen from run to run being <0.2%. Therefore, it seems that Ar ion bombardment on Al films does not influence the natural oxidation of the Al surface as discussed in modeling of Al films in the SE section.

It is known that the trapped Ar atoms in films under ion bombardment reside at grain boundaries.²⁰ According to Vancea's model, Ar atoms trapped at grain boundaries increase the height of potential barriers, localizing more electrons in grains. Alternatively, Ar atoms at grain boundaries act as electron traps, increasing the electrical resistivity. Also, Ar atoms at grain boundaries prevent diffusion of metal atoms across grain boundaries and so limit grain growth. However, we can speculate that since Ar ions in films have energy greater than the adatoms in the film and are moving with a preferred direction into the film, they do not necessarily all reside at grain boundaries and some may reside within grains. If this hypothesis is correct, the small amount of Ar in grains cannot be neglected as a factor in the change of electrical resistivity and stress. Therefore, in either case, the inclusion of Ar in films seems to affect electrical and structural properties.

VII. Conclusions

The following effects are observed in IAD Ag and Al films as the momentum transferred to the growing film by the Ar-ion beam per arriving metal atom increases:

(1) In the intraband transitions, the refractive index increases and extinction coefficient decreases, resulting in a decrease in reflectance. The interband absorption, however, decreases and reflectance increases. The changes in optical constants are consistent with the increase in the void fraction of the films and the reduction of the effective number density of free electrons in the intraband transitions.

(2) The lattice spacing perpendicular to the film surface expands. The stress changes from tensile to compressive for Ag films. The compressive stress of Al films increases slightly. The grain size decreases for both types of film. The dependence of stress on P supports Windischmann's scaling law, which relates stress to the momentum.

(3) The electrical resistivity increases. This is attributable to the reduced effective number density of free electrons. The decrease in grain size increases the number of potential barriers, which results in the decrease in the effective number density of free electrons. This is in good agreement with the observed reduction of the effective number density of free electrons in the intraband transitions resulting from the increase in the fraction of voids.

(4) The amount of trapped Ar increases slightly.

From the results of this study, IAD is likely to make Ag and Al metal thin films less bulklike by changing their microstructure. Also, many of their optical, electrical, and microstructural properties correlate well with the momentum transferred to the growing film by the Ar ions per arriving metal atom, suggesting that

the momentum is an important physical parameter in describing the influence of ion beam on growing thin films and determining the characteristics of IAD thin metal films.

The authors are extremely grateful to the University Research Initiative Program of the Air Force Office of Scientific Research for financial support. We wish to thank C. M. Falco of the University of Arizona Physics Department and Optical Sciences Center for allowing us to use the x-ray diffractometer; J. A. Leavitt, L. C. McIntyre, Jr., and their group of the University of Arizona Physics Department for RBS measurements; and K. Vedam of the Pennsylvania State University Materials Research Laboratory for the SE measurements. Also, we would like to thank M. R. Jacobson and B. G. Bovard for helpful discussions and M. R. Potoff and S. I. Rana for technical support.

References

1. J. M. E. Harper, J. J. Cuomo, R. J. Gambino, and H. R. Kaufman, "Modification of Thin Film Properties by Ion Bombardment during Deposition," in *Ion Bombardment Modification of Surfaces*, O. Auciello and R. Kelly, Eds. (Elsevier, Amsterdam, 1984).
2. P. J. Martin, "Ion-based Methods for Optical Thin Film Deposition," *J. Mat. Sci.* 21, 1-25 (1986).
3. U. J. Gibson, "Ion Beam Processing of Optical Thin Films," *Phys. Thin Films* 13, 109-150 (1987).
4. P. J. Martin, H. A. Macleod, R. P. Netterfield, C. G. Pacey, and W. G. Sainty, "Ion-Beam-Assisted Deposition of Thin Films," *Appl. Opt.* 22, 178-184 (1983).
5. R. P. Netterfield, W. G. Sainty, P. J. Martin, and S. H. Sie, "Properties of CeO₂ Thin Films Prepared by Oxygen-Ion-Assisted Deposition," *Appl. Opt.* 24, 2267-2272 (1985).
6. S. G. Saxe, M. J. Messerly, B. Bovard, L. DeSandre, F. J. Van Milligen, and H. A. Macleod, "Ion Bombardment-Induced Retarded Moisture Adsorption in Optical Thin Films," *Appl. Opt.* 23, 3633-3637 (1984).
7. T. Allen, "Properties of Ion Assisted Deposited Silica and Titania Films," *Proc. Soc. Photo-Opt. Instrum. Eng.* 325, 93-100 (1982).
8. E. H. Hirsch and I. K. Varga, "The Effects of Ion Radiation on the Adhesion of Germanium Films," *Thin Solid Films* 26, 445-452 (1978).
9. C. M. Kennemore III and U. J. Gibson, "Ion Beam Processing for Coating MgF₂ onto Ambient Temperature Substrates," *Appl. Opt.* 23, 3608-3611 (1984).
10. P. J. Martin, R. P. Netterfield, and W. J. Sainty, "Modification of the Optical and Structural Properties of Dielectric ZrO₂ Films by Ion-Assisted Deposition," *J. Appl. Phys.* 55, 235-241 (1984).
11. J. D. Targove, J. P. Lehan, L. J. Lingg, H. A. Macleod, J. A. Leavitt, and L. C. McIntyre Jr., "Ion-Assisted Deposition of Lanthanum Fluoride Thin Films," *Appl. Opt.* 26, 3733-3737 (1987).
12. S. S. Nandra, F. G. Wilson, and C. D. Desforges, "Modification of Gold Coatings by Ion Bombardment During Deposition," *Thin Solid Films* 107, 335-344 (1983).
13. W. C. Herrmann, Jr. and J. R. McNeil, "Ion Beam Application for Optical Coating," *Proc. Soc. Photo-Opt. Instrum. Eng.* 325, 101-104 (1982).
14. P. J. Martin, W. G. Sainty, and R. P. Netterfield, "Enhanced Gold Film Bonding by Ion-Assisted Deposition," *Appl. Opt.* 23, 2668-2669 (1984).

15. M. Laugier, "The Effect of Ion Beam Bombardment on Stress and Adhesion in Thin Films of Silver and Aluminum," *Thin Solid Films* 81, 61-65 (1981).
16. D. W. Hoffman and M. R. Gaertner, "Modification of Evaporated Chromium by Concurrent Ion Bombardment," *J. Vac. Sci. Technol. A* 17, 425-428 (1980).
17. F. Parmigiani, E. Kay, T. C. Huang, and J. D. Swalen, "Interpretation of the Nonbulklike Optical Density of Thin Copper Films Grown under Ion Bombardment," *Appl. Opt.* 24, 3335-3338 (1985).
18. G. A. Al-Jumaily, J. J. McNally, and J. R. McNeil, "Effect of Ion Assisted Deposition on Optical Scatter and Surface Microstructure of Thin Films," *J. Vac. Sci. Technol. A* 3, 651-655 (1985).
19. R. A. Roy, J. J. Cuomo, and Y. S. Yee, "Control of Microstructure and Properties of Copper-Films Using Ion-Assisted Deposition," *J. Vac. Sci. Technol. A* 6, 1621-1626 (1988).
20. F. Parmigiani, E. Kay, T. C. Huang, J. Perrin, M. Jurich, and J. D. Swalen, "Optical and Electrical Properties of Thin Silver Films Grown under Ion Bombardment," *Phys. Rev. B* 33, 879-883 (1985).
21. E. Kay, F. Parmigiani, and W. Parrish, "Effect of Energetic Neutralized Noble Gas Ions on the Structure of Ion Beam Sputtered Thin Metal Films," *J. Vac. Sci. Technol. A* 5, 44-51 (1987).
22. H. Windischmann, "An Intrinsic Stress Scaling Law for Polycrystalline Thin Films Prepared by Ion Beam Sputtering," *J. Appl. Phys.* 62, 1800-1807 (1987).
23. W. P. Chen and J. M. Chen, "Use of Surface Plasma Waves for Determination of the Thickness and Optical Constants of Thin Metallic Films," *J. Opt. Soc. Am.* 71, 189-191 (1981).
24. H. Rather, "Surface Plasma Oscillations and Their Applications," *Phys. Thin Films* 9, 145-262 (1977).
25. R. D. Olney and R. J. Romagnoli, "Optical Effects of Surface Plasma Waves with Damping in Metallic Thin Films," *Appl. Opt.* 26, 2279-2282 (1987).
26. H. A. Macleod, "Surface Plasmon Resonance Effects and the Admittance Diagram," *Proc. Soc. Photo-Opt. Instrum. Eng.* 777, 300-309 (1987).
27. G. V. Reklaitis, A. Ravindran, and K. M. Ragsdell, *Engineering Optimization Methods and Applications* (Wiley, New York, 1983).
28. F. S. Zhang, R. W. Wang, H. A. Macleod, R. E. Parks, and M. R. Jacobson, "Surface Plasmon Detection of Surface Contamination of Metallic Film Surfaces," *Proc. Soc. Photo-Opt. Instrum. Eng.* 777, 162-170 (1986).
29. D. E. Aspnes, E. Kinsbron, and D. D. Bacon, "Optical Properties of Au: Sample Effects," *Phys. Rev. B* 21, 3290-3299 (1980).
30. J. E. Yehoda, B. Yang, K. Vedam, and R. Messier, "Investigation of the Void Structure in Amorphous Germanium Thin Films as a Function of Low-Energy Ion Bombardment," *J. Vac. Sci. Technol. A* 6, 1631-1635 (1988).
31. K. Vedam and P. J. McMarr, "Nondestructive Depth Profiling by Spectroscopic Ellipsometry," *Appl. Phys. Lett.* 47, 339-341 (1985).
32. K. Vedam, S. Y. Kim, and L. D'Aries, "Nondestructive Depth Profiling of ZnS and MgO Films by Spectroscopic Ellipsometry," *Opt. Lett.* 12, 456-458 (1987).
33. S. Y. Kim and K. Vedam, "Simultaneous Determination of Dispersion Relation and Depth Profile of Thorium Fluoride Thin Films by Spectroscopic Ellipsometry," to be published.
34. D. E. Aspnes, "Microstructural Information from Optical Properties in Semiconductor Technology," *Proc. Soc. Photo-Opt. Instrum. Eng.* 276, 188-195 (1981); see also references therein.
35. S. Y. Kim and K. Vedam, "Proper Choice of the Error Function in Modeling Spectroellipsometric Data," *Appl. Opt.* 25, 2013-2021 (1986).
36. P. B. Johnson and R. W. Christy, "Optical Constants of Noble Metals," *Phys. Rev. B* 6, 4370-4379 (1972).
37. J. M. Ziman, *Principles of Theory of Solids* (Cambridge U.P., London, 1972).
38. R. W. Fane and W. E. J. Neal, "Optical Constants of Aluminum Films Related to the Vacuum Environment," *J. Opt. Soc. Am.* 60, 790-793 (1970).
39. L. G. Bernland, O. Hundrei, and H. P. Myers, "Optical Absorption in Vapor-Quenched Aluminum," *Phys. Rev. Lett.* 31, 363-365 (1973).
40. D. Y. Smith, E. Shiles, and M. Inokuti, "The Optical Properties of Metallic Aluminum," in *Handbook of Optical Constants of Solids*, E. D. Palik, Ed. (Academic, Orlando, 1985).
41. Joint Committee on Powder Diffraction Standards, 1601 Park Lane, Swarthmore, PA (1969).
42. H. P. Klug and L. E. Alexander, *X-Ray Diffraction Procedures* (Wiley, New York, 1974).
43. R. W. Vook and F. Witt, "Thermally Induced Strains in Evaporated Films," *J. Appl. Phys.* 36, 2169-2171 (1965).
44. T. C. Huang, G. Lim, F. Parmigiani, and E. Kay, "Effect of Ion Bombardment during Deposition on the X-Ray Microstructure of Thin Silver Films," *J. Vac. Sci. Technol. A* 3, 2161-2166 (1985).
45. D. E. Gray, Ed., *American Institute of Physics Handbook* (McGraw-Hill, New York, 1972).
46. J. J. Cuomo et al., "Modification of Niobium Film Stress by Low-Energy Ion Bombardment During Deposition," *J. Vac. Sci. Technol. A* 20, 349-354 (1982).
47. D. W. Hoffman and J. A. Thornton, "Internal Stresses in Sputtered Chromium," *Thin Solid Films*, 40, 355-363 (1977).
48. J. A. Thornton, J. Tabock, and D. W. Hoffman, "Internal Stresses in Metallic Films Deposited by Cylindrical Magnetron Sputtering," *Thin Solid Films* 64, 111-119 (1979).
49. L. J. van der Pauw, "A Method of Measuring Specific Resistivity and Hall Effect of Discs of Arbitrary Shape," *Philos. Res. Rep.* 13, 1-9 (1958).
50. R. Chwang, B. J. Smith, and C. R. Crowell, "Contact Size Effects on the van der Pauw Method for Resistivity and Hall Coefficient Measurement," *Solid-State Electron.* 17, 1217-1225 (1974).
51. K. L. Chopra, *Thin Film Phenomena* (McGraw-Hill, New York, 1969).
52. S. B. Soffer, "Statistical Model for the Size Effect in Electrical Conduction," *J. Appl. Phys.* 38, 1710-1715 (1967).
53. A. F. Mayadas and M. Shatzkes, "Electrical Resistivity Model for Polycrystalline Films: the Case of Arbitrary Reflection at External Surfaces," *Phys. Rev. B* 1, 1382-1389 (1970).
54. J. Vances and H. Hoffmann, "Reduced Density of Effective Electrons in Metal Films," *Thin Solid Films* 92, 219-225 (1982).
55. J. R. Sambles, "The Resistivity of Thin Films-Some Critical Remarks," *Thin Solid Films* 106, 321-331 (1983).
56. W. K. Chu, J. W. Mayer, and M. A. Nicolet, *Backscattering Spectrometry* (Academic, New York, 1978).

Reactive ion assisted deposition of aluminum oxynitride thin films

Chang Kwon Hwangbo, Linda J. Lingg, John P. Lehan, H. Angus Macleod, and F. Suits

Optical properties, stoichiometry, chemical bonding states, and crystal structure of aluminum oxynitride (AlO_xN_y) thin films prepared by reactive ion assisted deposition were investigated. The results show that by controlling the amount of reactive gases the refractive index of aluminum oxynitride films at 550 nm is able to be varied from 1.65 to 1.83 with a very small extinction coefficient. Variations of optical constants and chemical bonding states of aluminum oxynitride films are related to the stoichiometry. From an x-ray photoelectron spectroscopy analysis it is observed that our aluminum oxynitride film is not simply a mixture of aluminum oxide and aluminum nitride but a continuously variable compound. The aluminum oxynitride films are amorphous from an x-ray diffraction analysis. A rugate filter using a step index profile of aluminum oxynitride films was fabricated by nitrogen ion beam bombardment of a growing Al film with backfill oxygen pressure as the sole variation. This filter shows a high resistivity to atmospheric moisture adsorption, suggesting that the packing density of aluminum oxynitride films is close to unity and the energetic ion bombardment densifies the film as well as forming the compound.

I. Introduction

Aluminum oxynitride (AlO_xN_y) can be used as an optical thin film with variable optical constants between those of aluminum oxide and aluminum nitride. Rugate filters, which are designed with a sinusoidal refractive index profile, and other types of inhomogeneous films can be made by varying the refractive index of an aluminum oxynitride film continuously. AlO_xN_y can also be used as a tunable medium refractive index material in the near UV and visible, depending on the stoichiometry of AlO_xN_y and the application. Aluminum oxynitride has not been studied in detail when compared to aluminum oxide and aluminum nitride, and relatively few papers have been published on it. Stoichiometry and optical properties of aluminum nitride and oxynitride films prepared by ion assisted deposition (IAD) have been studied in this laboratory in the past.¹ Composite aluminum oxynitride [$(\text{Al}_2\text{O}_3)_x(\text{AlN})_y$] films prepared by laser assisted CVD showed a refractive index variation from 1.67 for Al_2O_3 to 2.08 for AlN at 300 nm by changing the substrate temperature.² Also ion beam sputtered alumi-

num oxynitride films have been used to encapsulate GaAs substrates at high temperature.³

In this study we made aluminum oxynitride films by bombarding a growing Al film with a nitrogen ion beam or a mixture of nitrogen-oxygen ion beam in an oxygen backfill. We investigated the optical properties, stoichiometry, chemical bonding states, and crystal structure of the films. To illustrate an application of aluminum oxynitride films, we made a rugate filter using a step index profile and compared its performance to the predicted value of a simulated one.

II. Deposition Conditions

Aluminum oxynitride films in our experiments were deposited by reactive IAD in a Balzers 760 box coater, which has been described elsewhere.¹⁻³ The base pressure was $\sim 7 \times 10^{-7}$ mbar. The chamber temperature was 100°C, and its variation during a single layer deposition was $< 10^\circ\text{C}$. Al was e-beam evaporated from an intermetallic crucible. The condensation rate was 3 Å/s as measured by a quartz crystal oscillator. Fused silica, graphite slabs, and Si wafers were used as substrates for the various postdeposition measurements. Just prior to deposition, substrates were sputter cleaned *in vacuo* by the ion beam for 20 s.

We employed a 3-cm aperture Kaufman hot cathode ion source for two cases with nitrogen or a mixture of nitrogen and oxygen gases as the bombarding species. In Case 1, nitrogen gas was admitted through the ion source until a pressure of 8×10^{-5} mbar was obtained in the chamber. Then oxygen gas was bled through the side of the chamber by an automatic gas pressure

When the work was done all authors were with University of Arizona, Optical Sciences Center, Tucson, Arizona 85721; C. K. Hwangbo is now with Inha University, Physics Department, Incheon, Korea, and F. Suits is now with IBM Watson Research Center, Yorktown Heights, New York.

Received 21 November 1988.

0003-6935/89/142779-06\$02.00/0.

© 1989 Optical Society of America.

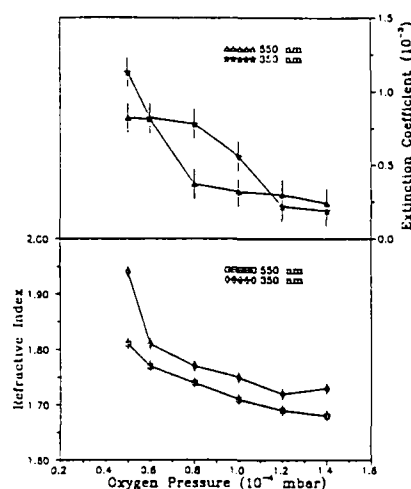


Fig. 1. Case 1: variations of refractive index and extinction coefficient of AlO_xN_y thin films at 350 and 550 nm as the backfilled oxygen pressure varies from 0.5 to 1.4×10^{-4} mbar. The nitrogen pressure through the ion gun was kept at 8×10^{-5} mbar. Ion energy was 1250 eV, and current density was $40 \mu\text{A}/\text{cm}^2$.

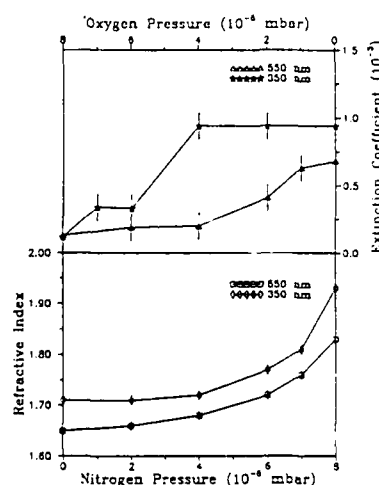


Fig. 2. Case 2: variations of refractive index and extinction coefficient of AlO_xN_y thin films at 350 and 550 nm as the pressure of a mixture of nitrogen/oxygen gases through the ion gun varies from $(0/8)$ to $(8/0) \times 10^{-5}$ mbar. The backfilled oxygen pressure was kept at 4×10^{-5} mbar. Ion energy was 1250 eV, and current density was $40 \mu\text{A}/\text{cm}^2$.

control valve, and its pressure was varied from 0.4 to 1.4×10^{-4} mbar to control the stoichiometry of AlO_xN_y films and thus the optical constants. In Case 2, a mixture of nitrogen and oxygen gases was admitted through the ion gun. The total pressure of nitrogen and oxygen in the chamber was kept at 8×10^{-5} mbar, while the ratio of two gases (nitrogen/oxygen) was varied from $8/0$ to $0/8$. Also backfill oxygen gas at a pressure of 4×10^{-5} mbar was let into the chamber. In both cases, the ion beam energy was 1250 eV, while the current density as measured by a Faraday cup was held at $40 \mu\text{A}/\text{cm}^2$.

III. Experiments and Results

A. Optical Constants Analysis

Refractive index n and extinction coefficient k of aluminum oxynitride films were obtained by measuring the transmittance in a Cary 2415 spectrophotometer (Varian) and using an envelope method which is applicable to weakly absorbing thin films.⁶

In addition to the basic envelope method, we corrected the rear surface reflections of the substrate and assumed a Cauchy's dispersion relation of the form

$$T = A + B/\lambda^2 + C/\lambda^4$$

for the envelopes. We then used the Cauchy's relation to calculate the optical constants at 350 and 550 nm.

In Case 1 when a nitrogen ion beam was used to bombard a growing Al film in an oxygen backfill, variations of n and k at 350 and 550 nm vs backfilled oxygen pressure are shown in Fig. 1. As the backfilled oxygen pressure increases from 0.5 to 1.4×10^{-4} mbar, n at 550 nm decreases from 1.81 to 1.68 and k at 550 nm de-

creases from 8.2 to 2.4×10^{-4} . As the amount of reactive oxygen gas increases, n and k of AlO_xN_y approach those of Al_2O_3 films.

In Case 2 when the mixture of nitrogen/oxygen ion beam was used to bombard a growing Al film in an oxygen backfill, variations of n and k at 350 and 550 nm vs different nitrogen/oxygen mixture ratios through the ion gun are shown in Fig. 2. As the pressure of nitrogen/oxygen gases changes from $(0/8)$ to $(8/0) \times 10^{-5}$ mbar, n at 550 nm increases from 1.65 to 1.83 and k at 550 nm increases 1.6 – 9.0×10^{-4} . As the ratio of nitrogen/oxygen gases increases, n and k of AlO_xN_y films increase toward those of AlN.

All aluminum oxynitride films showed good transmittance in the near UV (>300 nm) and visible. The cutoff wavelength was ~ 190 nm.

B. Rutherford Backscattering Spectrometry Analysis

Stoichiometry (x and y) of AlO_xN_y films was measured by Rutherford backscattering spectrometry (RBS).⁷

In Case 1, variations of x and y with an oxygen backfill are listed in Table I. As the backfilled oxygen pressure increases from 0.5 to 1.4×10^{-4} mbar, x increases from 0.85 to 1.28 , while y does not vary appreciably. Corresponding changes in n and k were discussed in the previous section and summarized in Fig. 1.

In Case 2, variations of x and y are listed in Table II. As the ratio (nitrogen/oxygen) is varied from $8/0$ to $0/8$ while keeping the sum of two partial pressures at 8×10^{-5} mbar, x decreases from 0.84 to 1.55 , while y decreases from 0.60 to 0 . Corresponding changes in n and k are shown in Fig. 2.

C. X-Ray Photoelectron Spectroscopy Analysis

While RBS provides quite accurate information about the film stoichiometry, it does not provide information about the chemical bonding states of the elements in the film. A Perkin-Elmer PHI 5100 ESCA system for x-ray photoelectron spectroscopy (XPS) was employed to investigate the chemical bonding states of AlO_xN_y films. $\text{Mg K}\alpha$ x-rays (1253.6 eV) were used, and all samples were sputter etched at 70° for 10 min by Ar ions at 4 keV to remove surface contaminants prior to making measurements. The Al_{2p} , O_{1s} , and N_{1s} peaks were investigated.

We were primarily interested in whether aluminum oxynitride is simply a mixture of aluminum oxide and aluminum nitride such as $(\text{Al}_2\text{O}_3)_x(\text{AlN})_y$ or an aluminum oxynitride compound (AlO_xN_y). If it were a mixture of two materials, we would expect the Al_{2p} peak to be a doublet. Thus as x increases and y decreases, the intensity of one peak bonded to oxygen increases, and that of the other peak bonded to nitrogen decreases without shifting the peak position. On the other hand, if it were a compound, we would see only a single Al_{2p} peak.

AlO_xN_y films investigated by XPS were prepared by varying the ratio of nitrogen/oxygen gas mixture through the ion gun (Case 2 films as are listed in Table II). As references, we made aluminum oxide and aluminum nitride films by bombarding an oxygen ion beam on a growing Al film in an oxygen backfill and a nitrogen ion beam on a growing Al film in a nitrogen

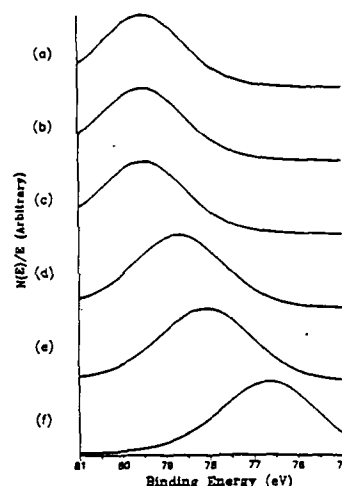


Fig. 3. Shift of the Al_{2p} peaks of AlO_xN_y from that of $\text{AlO}_{1.52}$ to that of $\text{AlN}_{1.23}$: (a) $\text{AlO}_{1.52}$; (b) $\text{AlO}_{1.42}\text{N}_{0.18}$; (c) $\text{AlO}_{1.33}\text{N}_{0.27}$; (d) $\text{AlO}_{1.00}\text{N}_{0.46}$; (e) $\text{AlO}_{0.84}\text{N}_{0.66}$; (f) $\text{AlN}_{1.23}$.

backfill, respectively. The aluminum nitride film showed superstoichiometry¹ ($\text{AlN}_{1.23}$) with a small amount of oxygen at the air-film interface which would be sputter etched by the Ar ions.

The Al_{2p} peaks of AlO_xN_y films are shown in Fig. 3 as x and y vary. Interesting, the AlO_xN_y films have a single Al_{2p} peak which shifts from the high binding energy [Fig. 3(a)] of $\text{AlO}_{1.52}$ to the lower binding energy [Fig. 3(f)] of $\text{AlN}_{1.23}$ as x decreases and y increases. When x is larger than 1.3 and y is smaller than 0.3, we see no shift in the Al_{2p} peak. In other words, it seems that a small amount of nitrogen ($y < 0.3$) does not appreciably affect the chemical bonding states of Al, and the dominant oxygen ($x > 1.3$) bonded to Al behaves as if it were bonded as aluminum oxide. As x decreases below 1.3 and y increases above 0.3, the Al_{2p} peak of AlO_xN_y films shifts toward that of $\text{AlN}_{1.23}$ because Al is shared by more N and less O. Since the binding energy of a single Al_{2p} peak of AlO_xN_y film shifts and the shape of the Al_{2p} peak does not change significantly as x and y vary, AlO_xN_y is a compound.

The O_{1s} peaks shown in Fig. 4 behave quite similarly to the Al_{2p} peaks in Fig. 3. When $x > 1.3$ and $y < 0.3$, the binding energy of O_{1s} of AlO_xN_y film does not move (as in the Al_{2p} case). This is further evidence that when oxygen is above a threshold value ($x \approx 1.3$ in this case), it behaves as aluminum oxide. When $x < 1.3$ and $y > 0.3$, the O_{1s} peak shifts to the lower binding energy.

The N_{1s} peaks are plotted in Fig. 5. As x increases and y decreases [from (e) to (a)], the main N_{1s} peak evolves from the low binding energy (400 eV) of $\text{AlN}_{1.23}$ to the high binding energy at which both N and O are bonded to Al. When $x = 1.42$ and $y = 0.18$, where the Al and O peaks are not separated from those of $\text{AlO}_{1.52}$, a new peak is observed at the 6.2-eV higher binding energy than the main N_{1s} peak, as shown in Fig. 6.

Table I. Variation of Stoichiometry (x and y) of AlO_xN_y Thin Films as the Pressure of Oxygen Backfill Changes

Ion source nitrogen (mbar) ($\times 10^{-5}$)	Backfill oxygen (mbar) ($\times 10^{-4}$)	AlO_xN_y	
		$x(\pm 0.05)^a$	$y(\pm 0.05)^a$
8	0.5	0.85	0.46
8	0.6	0.97	0.49
8	0.8	1.07	0.46
8	1.0	1.20	0.41
8	1.2	1.27	0.43
8	1.4	1.28	0.45

^a This represents the maximum excursion from film to film given the same nominal deposition conditions.

Table II. Variation of Stoichiometry (x and y) of AlO_xN_y Thin Films as the Ratio of a Mixture of Nitrogen/Oxygen Gases Through the Ion Gun Changes

Ion source Nitrogen (mbar) ($\times 10^{-5}$)	Oxygen (mbar) ($\times 10^{-5}$)	Backfill oxygen (mbar) ($\times 10^{-4}$)	AlO_xN_y	
			$x(\pm 0.05)^a$	$y(\pm 0.05)^a$
0	8	4	1.52	0
2	6	4	1.42	0.18
4	4	4	1.33	0.27
6	2	4	1.21	0.36
7	1	4	1.00	0.46
8	0	4	0.84	0.60

^a This represents the maximum excursion from film to film given the same nominal deposition conditions.

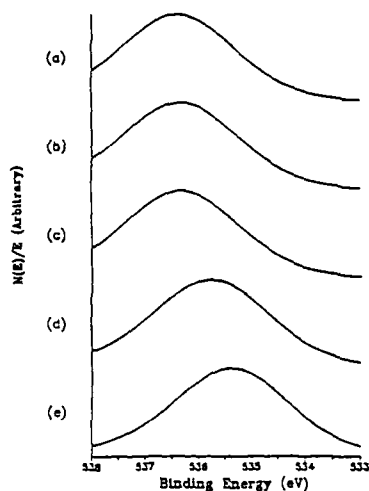


Fig. 4. Shift of the O_{1s} peaks of AlO_xN_y : (a) $AlO_{1.52}$; (b) $AlO_{1.42}N_{0.18}$; (c) $AlO_{1.33}N_{0.27}$; (d) $AlO_{1.00}N_{0.46}$; (e) $AlO_{0.84}N_{0.60}$.

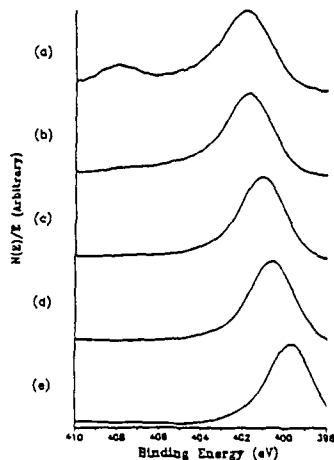


Fig. 5. Shift of the main N_{1s} peaks of AlO_xN_y and appearance of new peaks at higher binding energy for (a) and (b): (a) $AlO_{1.42}N_{0.18}$; (b) $AlO_{1.33}N_{0.27}$; (c) $AlO_{1.00}N_{0.46}$; (d) $AlO_{0.84}N_{0.60}$; (e) $AlN_{1.23}$.

When $x = 1.33$ and $y = 0.27$, where the Al and O peaks are the same as those of $AlO_{1.52}$, the new peak is very small and the main N_{1s} peak moves 0.1 eV to a lower binding energy (Fig. 6). When $x < 1.3$ and $y > 0.3$, the new peak disappears and the main N_{1s} peak shifts.

D. Infrared Transmittance and X-Ray Diffractometry Analysis

Aluminum oxynitride films are transparent up to $\sim 9 \mu m$ in the IR spectral range without much absorption, as measured by an Analect Instruments FX-6200 Fourier transform infrared spectrometer. Our aluminum oxynitride films exhibited no absorption lines of alu-

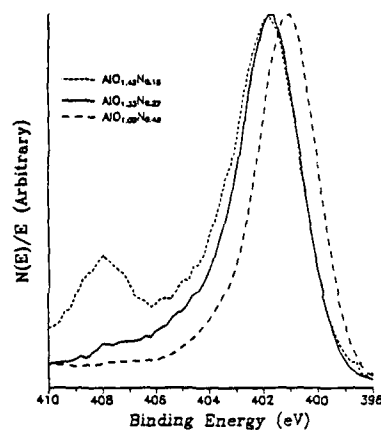


Fig. 6. Extended view of (a), (b), and (c) in Fig. 5.

minum oxide or aluminum nitride which were observed by Demiryont *et al.*² in composite aluminum oxynitride films. This agrees with the results from our XPS analysis that the aluminum oxynitride film prepared by reactive IAD is not a mixture of aluminum oxide and aluminum nitride but a compound. Also we have not seen any special absorption peaks which can be considered as aluminum oxynitride absorption peaks.

From Bragg θ -2 θ x-ray diffractometer analysis it was found that our aluminum oxide, aluminum oxynitride, and aluminum nitride films are amorphous.

IV. Applications

We made a rugate filter by using the step index profile of Fig. 7. Of the two ways we investigated to control the optical constants, we chose Case 1 where we varied the oxygen backfill pressure while a nitrogen ion beam bombarded the growing Al film. We chose this for the practical reason that the lifetime of the tungsten filaments in the ion gun decreases drastically when oxygen gas is used as a bombarding species. The backfilled oxygen gas pressure was varied from 0.5 to 1.4×10^{-4} mbar. We avoided 0.4×10^{-4} mbar of oxygen backfill at which the highest refractive index was obtained because downward fluctuations in oxygen pressure resulted in a large undesirable absorption in the near UV. Thus n was varied from 1.81 to 1.63. Each cycle has ten homogeneous step index layers and a 168.6-nm physical thickness. Fifteen cycles were deposited on a fused silica substrate. Measured reflectance R and transmittance T and theoretically simulated R and T from the assumed index profile (Fig. 7) (neglecting the dispersion of aluminum oxynitride films) are shown in Fig. 8. Absorption ($A = 1 - R - T$) of the filter (2.5- μm total thickness) at the peak wavelength is found to be $< 0.5\%$.

The discrepancy in T and R between real and simulated filters can be attributed to a fluctuation of backfilled oxygen pressure during each layer's deposition

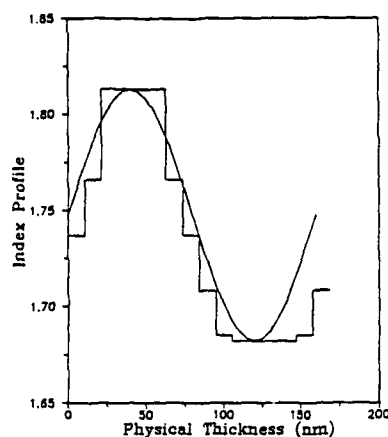


Fig. 7. Step-index profile of AlO_xN_y films obtained from Fig. 1 for a rugate filter. One cycle consists of ten homogeneous step index layers and has a 168.6-nm physical thickness. A sinusoidal curve is fitted to the step index profile.

and the nondispersive calculation used for the simulation. Also, the changes in refractive index were not sharp steps but had some slope, because the pressure of oxygen gas admitted into the chamber could not be increased or decreased instantaneously. Another possible reason for the discrepancy is that the nitrogen ion current density at the substrate on each layer varied slightly due to ion scattering from the different oxygen backfill pressure. It appears that these slight variations in each layer reduce the peak-to-peak variation of refractive index profile and cause a decrease in the peak reflectance in the real filter when compared with the simulated one. Better control of optical constants can be accomplished by computer automated control of gas pressure, accounting for fluctuations in the optical constants and thickness correction.

Moisture adsorption of this filter from the atmosphere was investigated by measuring the peak wavelengths of the filter under vacuum (10 mTorr) and at atmospheric pressure. No shift of the peak wavelength was observed. This indicates that the packing density of aluminum oxynitride films prepared in this fashion is close to unity.

V. Discussion

For the first time, we believe, the binding energy shift of the Al_{2p} peaks of AlO_xN_y films from aluminum oxide to aluminum nitride is observed as the stoichiometry changes. The differences in the binding energies of the Al_{2p} peaks of $\text{AlO}_{1.52}$ and $\text{AlN}_{1.23}$ films is 2.9 eV. In contrast, a 2-eV difference for the Al_{2p} peaks of Al_2O_3 and AlN films was observed in an ionized cluster beam deposited film.⁸

Similarly, new peaks at 6.5-eV higher binding energy than the main N_{1s} peak were observed when AlN powder was heated to between 700 and 900°C. These new peaks were attributed to oxynitrides.⁹ In our films the new peaks (Fig. 6) show up only when the amount of

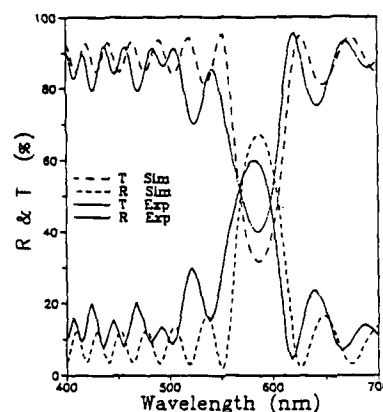


Fig. 8. Reflectance R and transmittance T of the real and simulated rugate filters. Fifteen cycles were employed.

nitrogen is small and the amount of oxygen is close to that of $\text{AlO}_{1.52}$. Since Al and O peaks for $x > 1.3$ and $y < 0.3$ are at the same binding energies and have the same shape as those of $\text{AlO}_{1.52}$ (Figs. 3 and 4), possible explanations for the new peak are that (1) this peak has to do with a reaction between nitrogen and oxygen (not necessarily NO but a general nitrogen-oxygen interaction) and (2) Al needs the minimum amount of oxygen (threshold value $x \approx 1.3$ in this case) to act like $\text{AlO}_{1.52}$. When $x = 1.42$ and $y = 0.18$, the excess oxygen ($x > 1.3$) reacts with nitrogen, and this results in the new peak at the high binding energy (408 eV), while the rest of the nitrogen reacts with Al and this contributes to the main N_{1s} peak (at 401.8 eV) (Fig. 6). When $x = 1.33$ and $y = 0.27$, the excess oxygen available for the nitrogen-oxygen reaction is small. Thus the new peak shifts to low binding energy (407 eV) and the intensity is low. Since more nitrogen ($y = 0.27$) reacts with Al than in the above case ($x = 1.42$ and $y = 0.18$), the main N_{1s} peak moves 0.1 eV to lower binding energy. As x decreases below 1.3 and y increases above 0.3, the new peak disappears because there is no excess oxygen to react with the nitrogen. Also since both oxygen and nitrogen react only with Al (for $x < 1.3$ and $y > 0.3$), the main N_{1s} peak moves in proportion to y .

Those films ($x > 1.3$ and $y < 0.3$) in which Al_{2p} , O_{1s} , and the main N_{1s} peaks are at the same binding energies show different transmittances and thus different optical constants. In XPS the only difference between these films is the different binding energy and heights between new peaks. Thus this new peak must be significant in determining the different optical constants for these films.

It is known that when an energetic N_2 ion bombards an Al surface, it is neutralized just before it strikes the surface and dissociated into two nitrogen atoms as it impacts.^{10,11} These two nitrogen atoms are implanted, react with two Al atoms, and result in 2AlN . The kinetic energy of each nitrogen atom is less than or

close to half of kinetic energy of N_2 ion because the N_2 ion loses its kinetic energy when it collides on the surface and it dissociates into two nitrogen atoms.¹²⁻¹⁴ On the other hand, a N ion in a nitrogen ion beam is neutralized and reacts with an Al atom with the same energy as it is given by the ion gun.

In our study we made an Al film in a nitrogen backfill (2×10^{-4} mbar) to check whether nitrogen molecules react with Al atoms. For this particular film the substrate temperature was 200°C to facilitate the reaction. It was found from RBS that the Al film consists of Al and O the atomic concentrations of which are $98 \pm 2\%$ and $2 \pm 2\%$, respectively. Even at the air-film and film-substrate interfaces only a small amount of oxygen was found. In other words, the nitrogen in the film and at the interfaces is under the detectable limit of RBS (~ 0.4 at. %). Thus Al does not chemisorb molecular nitrogen. This result agrees with Winters and Kay's classification¹⁵ of Al as one of the Class 2 materials which do not chemisorb molecular nitrogen but form nitrides.

Based on observations of Taylor *et al.*^{10,11} and Winters *et al.*,^{12,15} we can speculate what the nitrogen ion beam does in the formation of aluminum oxynitride films. Many molecular nitrogen ions (1250 eV) are neutralized and dissociated into nitrogen atoms on collision with the film surface. The resultant atomic nitrogen atoms (≤ 625 eV) penetrate the growing film, transfer their momenta to aluminum and oxygen atoms by collision cascades, and densify the film,¹⁶ slow down, and finally stop and react with aluminum and oxygen atoms. On the other hand, the atomic nitrogen ions (1250 eV) from the ion gun are neutralized, and the nitrogen atoms with 1250 eV follow a similar series of steps.

VI. Conclusions

Optical constant measurements, RBS, and XPS were combined to achieve an understanding of aluminum oxynitride films prepared by reactive ion assisted deposition. The refractive index at 550 nm with a very small extinction coefficient could be varied from 1.65 to 1.83, and a relationship between refractive index and stoichiometry was obtained. Aluminum oxynitride prepared by reactive ion assisted deposition is not simply a mixture of aluminum oxide and aluminum nitride but a compound. With a step index design, an aluminum oxynitride rugate filter has been successfully fabricated. Absorption of the filter was found to be $< 0.5\%$. No vacuum-to-air spectral shift of the rugate filter was observed, suggesting that the packing density of aluminum oxynitride films is close to unity, and the energetic nitrogen ion bombardment densifies the film as well as forming the compound. An amorphous aluminum oxynitride is a good candidate material for an inhomogeneous film, a rugate filter, and a medium index film, because the absorption is small and the optical constants can be readily varied from those of aluminum oxide to those of aluminum nitride by simply varying the amount of reactive gases introduced in the ion gun or alternatively the

backfilled gas while the ion beam bombards a growing Al film.

The authors are extremely grateful to the University Research Initiative Program of the Air Force Office of Scientific Research for its financial support. We wish to thank U. J. Gibson of the University of Arizona Optical Sciences Center for allowing us to use ESCA/SAM for XPS and J. A. Leavitt, L. McIntyre Jr., J. Oder, D. Ashbaugh, and B. Desfouly-Arjomandy of the University of Arizona Physics Department for RBS measurements. Also, we would like to thank B. G. Bovard and T. A. Taylor for helpful discussions and M. R. Potoff and S. I. Rana for technical support.

References

1. J. D. Targove, L. J. Lingg, J. P. Lehan, C. K. Hwangbo, H. A. Macleod, J. A. Leavitt, and L. C. McIntyre, "Preparation of Aluminum Nitride and Oxynitride Thin Films by Ion-assisted Deposition," *Mat. Res. Soc. Symp. Proc.* 93, 311-316 (1987).
2. H. Demiryont, L. R. Thompson, and G. J. Collins, "Optical Properties of Aluminum Oxynitrides Deposited by Laser-Assisted CVD," *Appl. Opt.* 25, 311-318 (1986).
3. H. Birey-Demiryont, S.-J. Park, and J. R. Sites, "Ion-Beam Sputtered Al_2O_3/N_x Encapsulating Films," *J. Vac. Sci. Technol. A* 16, 2086-2089 (1979).
4. C. K. Hwangbo, L. J. Lingg, J. P. Lehan, H. A. Macleod, J. L. Makous, and S. Y. Kim, "Ion Assisted Deposition of Thermally Evaporated Ag and Al Films," *Appl. Opt.* 28, 2769-2778 (1989).
5. C. K. Hwangbo, "Optical Thin Films Prepared by Ion Assisted and Ultrasound-Assisted Deposition," Ph.D. Dissertation, U. Arizona (1988).
6. J. C. Manifacier, J. Gasiot, and J. P. Fillard, "A Simple Method for the Determination of the Optical Constants n , k , and the Thickness of a Weakly Absorbing Thin Film," *J. Phys. E* 9, 1002-1004 (1976).
7. W. K. Chu, J. W. Mayer, and M. A. Nicolet, *Backscattering Spectrometry* (Academic, New York, 1978).
8. H. Takaoka, "Low Temperature Growth of AlN and Al_2O_3 Films by the Simultaneous Use of a Microwave Ion Source and an Ionized Cluster Beam System," *Thin Solid Films* 157, 143-158 (1988).
9. A. D. Katnani and K. I. Papathomas, "Kinetics and Initial Stages of Oxidation of Aluminum Nitride: Thermogravimetric Analysis and X-Ray Photoelectron Spectroscopy Study," *J. Vac. Sci. Technol. A* 5, 1335-1340 (1987).
10. J. A. Taylor, G. M. Lancaster, A. Ignatiev, and J. W. Rabalais, "Interaction of Ion Beams with Surfaces. Reactions of Nitrogen with Silicon and its Oxides," *J. Chem. Phys.* 68, 1776-1784 (1978).
11. J. A. Taylor and J. W. Rabalais, "Reaction of N_2^+ Beams with Aluminum Surfaces," *J. Chem. Phys.* 75, 1735-1745 (1981).
12. H. F. Winters, D. E. Horne, and E. E. Donaldson, "Adsorption of Gases Activated by Electron Impact," *J. Chem. Phys.* 41, 2766-2772 (1964).
13. H. F. Winters, "Ionic Adsorption and Dissociation Cross Section for Nitrogen," *J. Chem. Phys.* 44, 1472-1476 (1966).
14. H. F. Winters and E. Kay, "Gas Incorporation into Sputtered Films," *J. Appl. Phys.* 38, 3928-3934 (1967).
15. H. F. Winters and E. Kay, "Influence of Surface Adsorption Characteristics on Reactively Sputtered Films Grown in the Biased and Unbiased Modes," *J. Appl. Phys.* 43, 794-799 (1972).
16. K.-H. Muller, "Model for Ion-Assisted Thin Film Densification," *J. Appl. Phys.* 59, 2803-2807 (1986).

SCATTERING FROM SURFACES AND MULTILAYER COATINGS: RECENT ADVANCES FOR A BETTER INVESTIGATION OF EXPERIMENT

C. Amra, P. Bousquet

Laboratoire d'Optique des Surfaces et des Couches Minces - Unité Associée au C.N.R.S. (U.A. 1120) - Ecole
Nationale Supérieure de Physique de Marseille - Domaine Universitaire de St Jérôme - 13397 Marseille
Cedex 13 - France

Abstract

It is necessary to take into account scattering phenomena in optical systems since one is interested in a very detailed energy balance. We recall the principles of the vector theories that have been developed to predict the spatial and spectral distribution of light scattered from an optical surface or a multilayer coating. With the help of a scattering apparatus, we emphasize the key scattering parameters (roughness, autocorrelation length, isotropy degree, crosscorrelation laws) that are necessary to characterize surface defects and materials microstructure in thin film form. In spite of numerous parameters involved in the calculation, particular techniques enable us to extract all these parameters and lead to good agreement between theory and experiment. When the coating is made of a high number of layers, investigation of experimental results is quite more difficult. However, with the help of a correctly chosen model, we can strongly reduce the number of scattering parameters, and this allows an easy comparison between theory and experiment.

I - INTRODUCTION

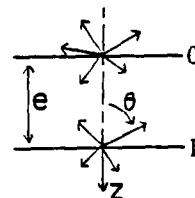
Drawing up a very detailed energy balance (typically at better than 10^{-3}) in optical multilayers remains until now a difficult problem because of numerous parameters that are more or less connected to the microstructure [1, 2] of materials in thin film form, such as absorption, surface and volume scattering, adsorption, index inhomogeneity and anisotropy, ... Even in the simplest case of a single layer (figure 1) deposited on a transparent substrate, we must write:

$$1 = R + T + A + D_e + D_i$$

where:

- R and T are the reflection and transmission coefficients of the ensemble (layer-substrate);
- A characterizes absorption losses [3, 4];
- D_e characterizes external scattering losses [5, 6], which represent the quantity of scattered light that can merge out of the stack and that is easily measurable;
- D_i characterizes internal scattering losses (fig. 1), which represent the quantity of scattered light embedded inside the stack, and that can be absorbed or not.

Fig. 1 - Scattering from the two interfaces (0) and (1) of a single layer with thickness e . External scattering D_e characterizes scattered waves that can merge out of the layer and that can be easily measurable. Internal scattering D_i characterizes the quantity of scattered light which is embedded inside the layer (scattering at large angles θ in the layer).



In the same way, to explain the differences observed between calculated and measured optical properties of these layers, we are often constrained to take account of a gradient index inside the layer [7], which is characteristic of the material growth in a columnar form. Let us notice that this columnar growth can also induce a slight anisotropy of the refractive index, that can be measurable with guided wave techniques [8].

Our laboratory has developed experimental and theoretical tools to investigate each of these phenomena [7, 8, 9, 10, 11, 12, 13], which permitted us to demonstrate the preponderance of surfacic scattering phenomena in the limitation of optical coating performances [14] (in particular for high quality mirrors and multiple cavity Fabry-Perot filters used in multi-demultiplexing systems). At this time, we have at our disposal a scattering apparatus [15] capable of measuring the scattered light in whole space and a vector theory [16] to investigate experimental results. We have noted an excellent agreement between theory and experiment in many cases, especially for bare substrates [15], antireflection layers [17, 18] and multilayer mirrors [19]. However, comparison of theory and experiment [20] remains quasi impossible in the case of complex coating designs, because of the high number of parameters involved in the calculation ($5p+4$ parameters for a p -layers stack).

On this subject, we will show here how a correctly chosen model enables us to strongly reduce the number of scattering parameters. This allows computation of systematic research of the scattering parameters that lead to the best agreement between theory and experiment.

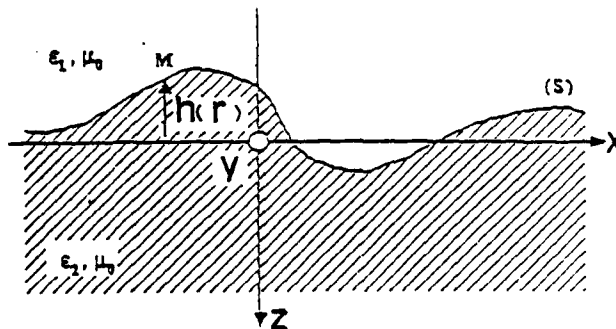
In a more general way, we will try here to give some elements of response to the following questions: what are the key parameters that characterize scattering from surfaces and multilayer coatings? What techniques can be used to point out these parameters? How can we improve the theoretical model to allow an easy comparison between theory and experiment, and consequently extract the maximum information from the measurements? So we first propose an up to date review which will permit us, without entering the detail of calculation, to present some recent results obtained in our laboratory.

II - VECTOR SCATTERING THEORY FOR OPTICAL SURFACES AND MULTILAYER OPTICS: RECALLS AND COMPLEMENTS

Among the vector theories that can predict the spatial distribution of light scattered from an optical surface, Elson's [5, 21] and Bousquet's [16] theories take a particular place because they present the advantage that they can also be applied to the case of multilayer coatings. It is certainly useful to begin by some recalls concerning the fields of application of these two theories, that are:

- the height fluctuations $h(\vec{r})$ of the surface (figure 2) are assumed to be very small with respect to the wavelength of incident light.
- the slope of the surface defects is very small with respect to unity.

Fig. 2 - Profile $h(\vec{r})$ of a rough surface separating 2 media of permittivities ϵ_1 and ϵ_2 . (xoy) is the mean plane of the rough surface.



Both mediums (ϵ_1 and ϵ_2) (fig. 2) are assumed to be linear, homogeneous and isotropic. We want also to emphasize the fact that these are perturbative theories, for which the surface is considered as a deformation of a perfectly flat surface (with no roughness).

Hence it is obvious that these theories can only be applied to the case of very good quality optical surfaces (micropolishes), with no pits, no scratches, no dust ...

1) Equivalence between Elson's and Bousquet's theories

Without entering the detail of calculation that can be found elsewhere [22], we briefly indicate here the reason why the two theories [16, 21] are equivalent for the calculation of external scattering. In fact, resolution of Maxwell's equations show that the field scattered by a rough surface separating two media is equal to the field radiated by surfacic currents distributed on a perfectly plane ($z = 0$) surface ("ideal surface") separating the same media. The scattered field \vec{E}^d being defined as the difference between the total field \vec{E} existing in space when the rough surface is illuminated and the "ideal" field \vec{E}^0 which would exist in the same conditions if the surface was perfectly flat, it follows the two equations:

$$\text{rot } \vec{E}^d = j\omega\mu \vec{H}^d + \vec{M} \delta(z) \quad (1-a)$$

$$\text{rot } \vec{H}^d = -j\omega\epsilon_1 \vec{E}^d + \vec{J} \delta(z) \quad (1-b)$$

where:

- \vec{E}^d and \vec{H}^d are electric and magnetic scattered fields
- \vec{M} and \vec{J} are magnetic and electric surfacic currents
- δ is the Dirac distribution
- $\epsilon_1 = \epsilon_1 + (\epsilon_2 - \epsilon_1) H(z)$ with H being the Heaviside function
- ϵ and μ are permittivity and permeability of the media
- $\omega = 2\pi/\lambda$ with λ being the wavelength of incident light.

According to the calculation method that is employed to obtain equations (1), the source couple (\vec{M}, \vec{J}) can be written following Elson:

$\vec{M} = \vec{M}_t$ and $\vec{J} = \vec{J}_t$ (where the index t indicates that the currents are tangential to the ideal surface $z = 0$)

or following Bousquet:

$\vec{M} = \vec{0}$ and $\vec{J} = \vec{J}_t + \vec{J}_N$ (where the index N indicates a normal component of the electric current). One can then verify that the tangential components of the fields scattered by the source couples (\vec{M}_t, \vec{J}_t) and $(\vec{0}, \vec{J}_t + \vec{J}_N)$ are identical because of the relation

$$j\omega\epsilon_2 \vec{M}_t - \vec{z} \wedge (\text{grad } J_{N1})_t = \vec{0}.$$

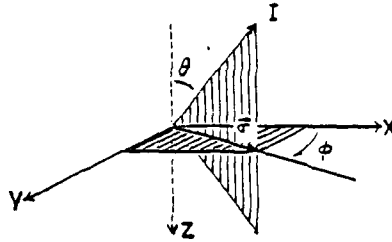
Consequently these two theories lead to identical results as far as calculation of external scattering is concerned.

2) Results for a single surface

Resolution of equation (1) is made in the Fourier plane and leads to the following expression for the intensity scattered in a particular direction (θ, ϕ) of space (fig. 3):

$$I(\theta, \phi) = a(\theta, \phi) \gamma(\theta, \phi)$$

Fig. 3 Scattering angles θ and ϕ that characterize a scattering direction. (xoy) is the mean plane of the rough surface. $(\vec{\sigma})$ is the spatial frequency of the grating responsible for scattering at (θ, ϕ) .



The coefficient $a(\theta, \phi)$ is called "ideal coefficient" because it does not depend on the surface defects, but only on the illumination and observation conditions. The roughness spectrum $\gamma(\theta, \phi)$ is the Fourier transform of the autocorrelation function of the profile $h(\vec{r})$, and contains all accessible information on the interface defects.

To permit a better understanding, it is convenient to consider the rough surface $h(\vec{r})$ as the sum of an infinity of sinusoidal gratings (Fourier decomposition). In the case of normal incidence, one can easily show that the fields scattered at symmetrical directions (θ, ϕ) and $(\theta, \phi + \pi)$ take their origin in the presence, on the rough surface, of one sinusoidal grating

$$s_{\sigma}(\vec{r}) = 2|\hat{h}(\vec{\sigma})| \cos[\vec{\sigma} \cdot \vec{r} - \psi(\vec{\sigma})]$$

with:

$$\hat{h}(\vec{\sigma}) = \text{FT}[h(\vec{r})] = |\hat{h}(\vec{\sigma})| e^{j\psi(\vec{\sigma})}$$

$$\vec{\sigma} = \frac{2\pi}{\lambda} \sin\theta \begin{pmatrix} \cos\phi \\ \sin\phi \end{pmatrix}$$

Through this remark, we can see that measurement of scattering at a given direction θ will give us information on a particular defect (fig. 3) which spatial period is $C = \frac{\lambda}{\sin\theta}$. This will

be essential for the calculation of roughness which will depend on the different kinds of measurable defects (see III-2).

When the surface is illuminated at normal incidence with natural light, the ideal coefficient only depends on θ and the scattered intensity can be written as: $I(\theta, \phi) = a(\theta) \gamma(\theta, \phi)$ or also:

$I(\vec{\sigma}) = a(\sigma) \gamma(\vec{\sigma})$ where $\sigma = |\vec{\sigma}|$. If we rotate now the surface of an angle α around its normal, its profile must then be written in the $(o x y z)$ coordinates system as $h'(\vec{r}) = h[R_\alpha(\vec{r})]$, where R_α is a rotation of angle α in the plane oxy . As rotation is conserved by Fourier Transform, we can then measure the quantity

$$I_m(\vec{\sigma}) = a(\sigma) \gamma[R_\alpha(\vec{\sigma})]$$

that is $I_m(\theta, \phi) = a(\theta) \gamma(\theta, \phi + \alpha) = I(\theta, \phi + \alpha)$

This shows that it is equivalent in these conditions to measure scattering in the whole space or to limit the measurements in one particular plane ϕ for different angular positions α of the sample in its own plane. Our scattering apparatus [15, 16] is based on this principle and this is also quite useful for investigation of roughness anisotropy (see III-4). In the case of an isotropic surface, the scattering distribution will be obviously symmetrical with respect to the normal of the sample.

3) Case of a multilayer coating

In the case of a multilayer coating (fig. 4), each rough interface is a source of scattered light. The scattered intensity that can be measured is due to the superposition of the waves emitted by these surfaces and we have to take into account both the multiple reflections of each scattered wave inside the multilayer and the interference phenomena between all these scattering sources. The preceding theories [16, 21] can be easily generalized to the case of multilayer coatings and lead to the following expression for the scattered intensity:

$$I(\theta, \phi) = \sum_{i=0}^p |C_i|^2 \gamma_{ii} + \sum_{i \neq j} C_i \bar{C}_j \gamma_{ij}$$

(\bar{C}_j = conjugate complex number of C_j)

where p is the number of layers of the stack and γ_{ij} the roughness spectrum of interface (i) (it contains all information relative to the defects of this interface). The C_i coefficients are called "ideal coefficients" because they only depend on the formula of the coating and on the illumination and observation conditions (incidence, wavelength and polarization). They take into account the multiple reflections of the scattered waves inside the stack. The γ_{ij} term is the Fourier Transform of the crosscorrelation function between the profiles of surfaces (i) and (j), and takes into account the interference phenomena between the scattering sources at interfaces (i) and (j). It is commonly used to define a crosscorrelation coefficient α_{ij} by the relation $\gamma_{ij} = \alpha_{ij} \gamma_{jj}$. This coefficient can be seen as a degree of coherence between the scattering sources (i) and (j), or as a degree of similitude between the surface profiles (i) and (j).

In order to simplify, it is generally assumed that α_{ij} does not depend on spatial frequency, so that we are interested only in the two extreme cases of uncorrelated surfaces ($\alpha_{ij} = 0$) and perfectly correlated surfaces ($\alpha_{ij} = 1$). One also usually consider that such coefficient α_{ij} is a free parameter, independent of roughness. We will see in section V how a

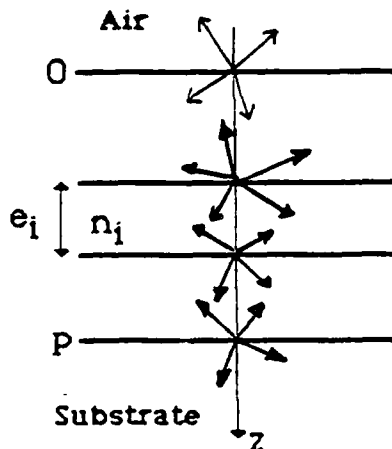


Fig. 4 - Scattering from a multilayer stack with p layers of thicknesses e_i and indices n_i . Each interface is a source of scattered light.

more realistic model can be developed. In a general way, these crosscorrelation laws are the key parameters for understanding and controlling scattering phenomena.

III - SIMULTANEOUS USE OF THEORY AND EXPERIMENT IN THE CASE OF A SINGLE SURFACE

Let us first specify that we can use calculation to investigate experiment only in the case of surfaces that are conformable to the theoretical model (see section II), that are of good quality, with no defects such as dust particles, pits, scratches ... The experimental results that are presented here are always relative to such surfaces that have been previously cleaned and then observed with a Nomarsky microscope. We intend here to emphasize the problems that must be solved when characterizing an optical surface [6, 23, 24] with scattering measurements, and to bring some solutions. We will limit ourselves to the case of sufficiently opaque substrates so that we have no difficulties with volume or back surface substrate scattering. In the case of transparent sample, we usually make use of the aluminum technique [13, 25].

1) Extraction of roughness spectrum

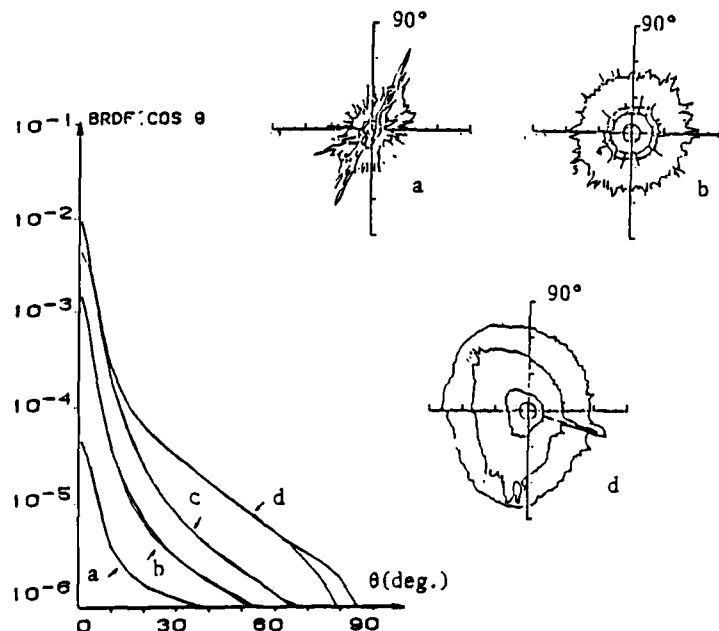
It is obvious that measurement of scattered intensity $I(\theta, \phi)$ together with calculation of ideal coefficient $a(\theta, \phi)$ leads to the roughness spectrum $\gamma(\theta, \phi)$. We have verified that this roughness spectrum remains invariable when the incidence and polarization of incident light are modified [15], which shows that γ is a real characteristic of the surface defects. Such results are therefore a good test for both the validity of theory and the accuracy of the measurements.

In many cases, we verified that the spectrum γ of isotropic surfaces could be fitted in the range of measurable spatial frequencies with the Hankel Transform γ_a of the sum Γ_a of an exponential and a gaussian function [6]:

$$\Gamma_a(\tau) = \delta_g^2 e^{-\left(\frac{\tau}{L_g}\right)^2} + \delta_e^2 e^{-\left(\frac{\tau}{L_e}\right)}$$

Fig. 5 gives an idea of the quality of agreement between theory and experiment such obtained on angular scattering curves.

Fig5 - Comparison of theory and experiment for four black glasses. $BRDF \cdot \cos \theta$ [16] is the scattered flux per unit of surface and solid angle, normalized to the incident flux. For each sample (a, b, c, d), we have superimposed the calculated and measured angular scattering curves at quasi-normal incidence and at the wavelength $\lambda = 632.8 \text{ nm}$. We have also plotted the anisotropy maps [15] [24] for 3 samples. The angular range (0 to 90°) corresponds to scattering by reflection.



2) Calculation of roughness

The roughness δ (mean quadratic height) can immediately be obtained by integration of the roughness spectrum in the range of measurable spatial frequencies $\vec{\sigma}$:

$$\delta^2 = \int_{\vec{\sigma}} \gamma(\vec{\sigma}) d\vec{\sigma} \quad \text{at normal incidence}$$

For an isotropic surface, we obtain: $\delta^2 = 2\pi \int_{k \sin \theta_m}^k \sigma \gamma(\sigma) d\sigma$

with $k = \frac{2\pi}{\lambda}$ and θ_m = scattering measurement minimum angle (with respect to the sample normal).

However, we must notice here (as shown in section II-2) that this roughness δ is relative to particular defects responsible for external scattering, that have spatial periods C in the range

$\lambda \leq C \leq \frac{\lambda}{\sin \theta_m}$. Consequently, it is not possible to definitely associate a roughness δ to a surface,

since the value of δ will depend on the wavelength under study, on the angular range where scattering measurements are performed and on the illumination incidence, according to the different kinds of defects that are concerned. Exactly speaking, a roughness measured at wavelength λ_1 cannot be used for calculation at λ_2 . Therefore, one must be careful as far as the statistical parameters of an optical surface are concerned.

3) Autocorrelation length

Usually, the autocorrelation length of surface defects is taken as the value L_g of the preceding gaussian function ($L_e > L_g$). But this implicitly assumes that the analytic function γ_a can fit the roughness spectrum γ in a range of spatial frequencies from 0 to infinity. However, according to the type of surface under study, the errors such committed are practically always acceptable. For that matter, we verified that the exact value δ of the roughness (obtained by integration of the roughness spectrum γ) is very close to the value $\sqrt{\delta_e^2 + \delta_g^2}$. Anyway, we can take into account the limited domain of measurable spatial frequencies and obtain the autocorrelation function by using a convolution product [24]. We have also studied the effects due to the apparatus function of the scatterometer [24].

4) Problems connected with anisotropy of surface defects

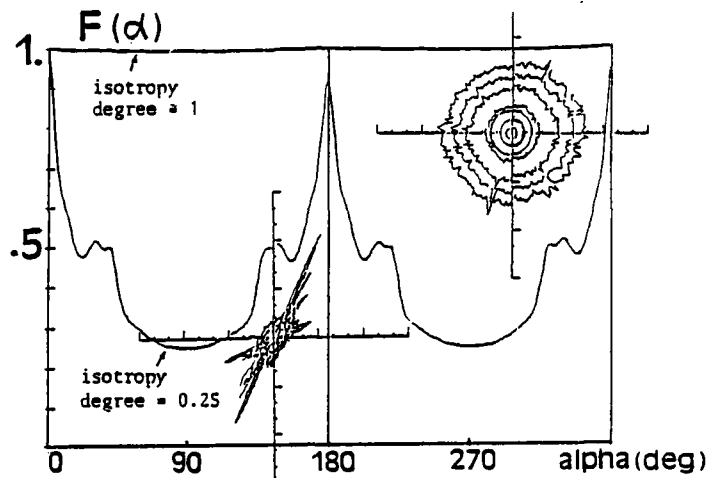
Another problem which appears when associating a roughness to an optical micropolish is due to the fact that anisotropy defects are not taken into account. In fact, some surfaces give rise to scattering levels that are very different according to the scattering plane ϕ where measurements are performed (fig. 5). Such roughness anisotropy leads to some error on the measurement of roughness and it is interesting to be able to quantify it. For that, we calculate an anisotropy function $F(\alpha)$ defined by:

$$\begin{aligned} F(\alpha) &= \int_{\vec{\tau}} \Gamma(\vec{\tau}) \Gamma[R_\alpha(\vec{\tau})] d\vec{\tau} \\ &= 4\pi^2 \int_{\vec{\sigma}} \gamma(\vec{\sigma}) \gamma[R_\alpha(\vec{\sigma})] d\vec{\sigma} \end{aligned}$$

where Γ is the autocorrelation function of the surface defects. While $\Gamma(\vec{\tau})$ measures the similitude between profiles $h(\vec{r})$ and $h(\vec{r} - \vec{\tau})$, the function $F(\alpha)$ measures the similitude between $\Gamma(\vec{\tau})$ and $\Gamma[R_\alpha(\vec{\tau})]$. It is the angular autocorrelation of the autocorrelation function $\Gamma(\vec{\tau})$ of the surface profile $h(\vec{r})$. In the case of isotropic defects, the Γ function will be radial and the anisotropy function $F(\alpha)$ will be constant. Then it is reasonable to define an isotropy degree from the minimum of the curve $F(\alpha)$ (Fig. 6), and the surface will be said perfectly isotropic if its isotropy degree is equal to unity. We will later present complementary results, in particular about the variations of isotropy degree versus spatial frequency. These

studies concerning roughness anisotropy are quite promising since anisotropy maps are a real signature of surface defects.

Fig. 6 - Anisotropy functions $F(\alpha)$ and anisotropy maps for isotropic (isotropy degree = 1) and anisotropic (isotropy degree = 0.25) surfaces. Measurements are performed at the wavelength $\lambda = 632.8$ nm.



IV - SIMULTANEOUS USE OF THEORY AND EXPERIMENT IN THE CASE OF MULTILAYER COATINGS

The case of multilayer coatings is quite more complex because of the high number of parameters involved in the calculation. We must take into account the roughnesses δ_e, δ_g and autocorrelation lengths L_e, L_g at each interface, as well as crosscorrelation coefficients between surfaces, so that $(5p + 4)$ parameters are required to describe scattering from a p -layer coating. Though it is always possible, in these conditions, to find a family of parameters leading to good agreement between calculation and experiment, this family is not necessarily unique and we must use complementary techniques to verify the obtained conclusions. For that, the use of specific stacks judiciously chosen [26] or particular effects such as antiscattering [17] allows us to eliminate any ambiguity on the choice of these parameters. It is also possible to use variations of scattering versus wavelength [14, 25, 27] or illumination incidence, or the aluminum layer technique [13, 25], to confirm the results. We will try here to rapidly describe these different methods capable of pointing out the key parameters of scattering. We will also recall how these parameters give us access to information concerning the microstructure of materials in thin film form.

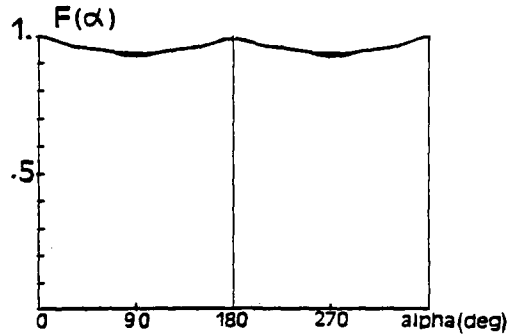
We insist again on the fact that all measurements here are relative to thin films of good quality, so that calculation can be meaningful. Observations with a Nomarski microscope allow us to verify that the top interface of the coating has a quality very similar to that of the substrate before coating (no dust, pits or scratches ...). The coatings are produced with multiple precautions and the conclusions drawn here obviously depend on the deposition techniques that are employed. In order to obtain a detailed confrontation between theory and experiment, the coatings are generally produced on black glasses and scattering from back surface substrate is therefore eliminated.

1) Aluminum technique

Contrary to the case of only one surface, it is quasi impossible to isolate the flux scattered from one particular surface of a multilayer stack. However, we have access to the roughness of the top interface of the coating by covering it with a thin (150 nm) opaque layer of Aluminum. Such method obviously assumes that the deposition conditions of the metal are good enough so that all top interface defects are reproduced by the aluminum layer. On this matter, our experimental results confirm these predictions, at least for glass surfaces with roughnesses greater than 0.5 nm. The mean roughness spectrum has been found to be unchanged before and after deposition of aluminum, in the whole range of measurable spatial frequencies [25]. As for anisotropy defects, fig. 7 shows that the results are extremely satisfying.

However, one should take care when using this technique for substrates with roughnesses less than 5 Å, because the aluminum microstructure can limit the reproduction of substrate defects [28].

Fig. 7 - Anisotropy functions $F(\alpha)$ of a black glass before and after deposition of a thin opaque layer of Aluminum. The two curves are practically identical.



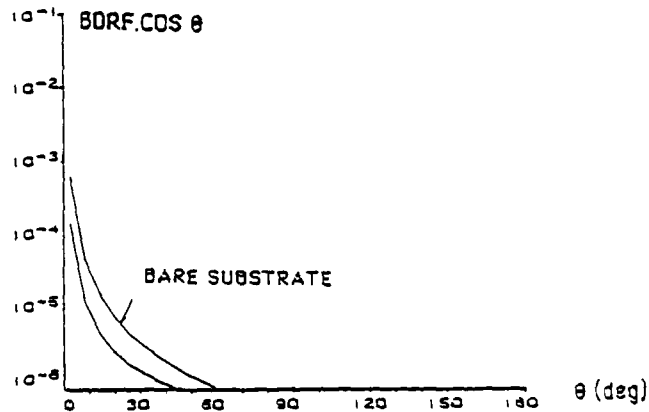
Such metallic layer technique is quite useful because it considerably reduces the number of scattering parameters. In the case of a single layer for instance (9 parameters), we can measure the roughness spectra of the substrate before coating and of the top interface after coating and Al deposition, so that only the crosscorrelation coefficient remains to be determined. However, as it was shown by few experimental results, such coefficient α can depend on spatial frequency [17] and can lie in the range $0 \leq \alpha \leq 1$ [29].

In the case of a multilayer mirror (15 layers), the Al layer technique led to excellent agreement between theory and experiment [19, 25].

2) Use of antiscattering effect

Antiscattering effect has already been largely described [17, 18], and is related to the fact that scattering can strongly be reduced after deposition of one particular layer on a substrate (provided that we have good correlation between interfaces). In the case of the TiO_2 layer in fig. 8, we have shown [19] that reduction of scattering cannot be explained assuming uncorrelated surfaces ($\alpha = 0$): the two scattering interfaces show very good correlation ($\alpha \approx 1$).

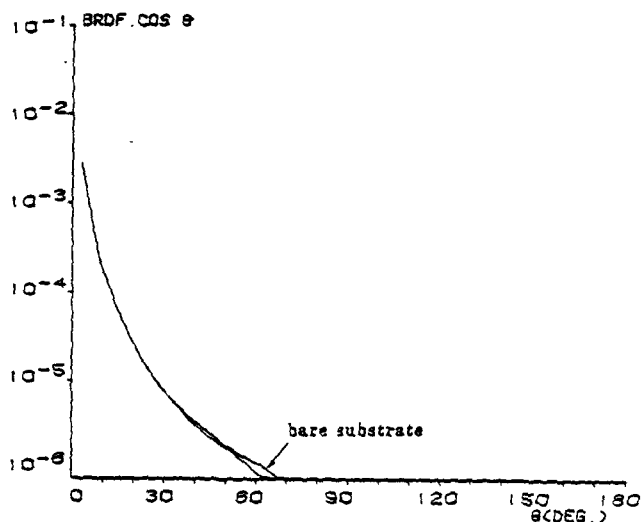
Fig. 8 - Angular scattering curves measured at quasi-normal incidence for a black glass before and after coating by a single TiO_2 layer with optical thickness $\lambda_0 = 632.8$ nm. Scattering losses measured at λ_0 are reduced by 58% after coating.



Antiscattering effect also brings information on the microstructure (at the scale of optical spatial frequencies) of materials in thin film form. In the case of the SiO_2 layer shown in fig. 9 for example, the two angular scattering curves before and after coating are identical, which indicates that the two interfaces are perfectly correlated ($\alpha = 1$) and that they have identical roughnesses: the material microstructure is sufficiently fine to reproduce all substrate defects without increasing or decreasing their magnitude. Furthermore, we can use

substrates of increasing quality until we obtain departure of the two angular scattering curves before and after coating, which will be connected to the limit of reproduction of substrate defects. Complementary results will be found elsewhere [17].

Fig. 9 - Angular scattering curves measured at normal incidence for a black glass, before and after coating by a SiO_2 layer with optical thickness $\lambda_0/2$. The two curves are practically identical, which indicates a quasi-perfect correlation ($\alpha \approx 1$) and identical roughnesses ($\delta_0 = \delta_1$) at the two interfaces of the layer.



3) Variations versus wavelength

Our calculation programs enabled us to show that scattering losses vary in phase or in phase cancellation with the reflection coefficient of the stack, according to the value ($\alpha = 1$ or $\alpha = 0$) of the crosscorrelation coefficient between interfaces [27].

The example shown in fig. 10 for one single layer obviously shows that measurements of scattering versus wavelength will rapidly give access to the crosscorrelation coefficients.

Let us notice also the stability of antiscattering effect (fig. 11) over a wide range of wavelengths in the case of a quarterwave low index layer.

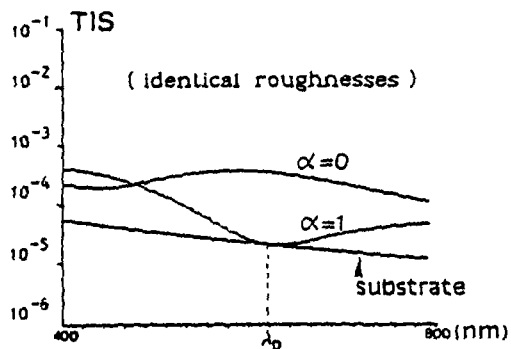


Fig.10 - Variations of scattering losses (integrated in whole space) or TIS versus wavelength in the case of ZnS layer with optical thickness $\lambda_0/2$, for two extreme values of the crosscorrelation coefficient α . The two roughnesses are assumed identical for this calculation.

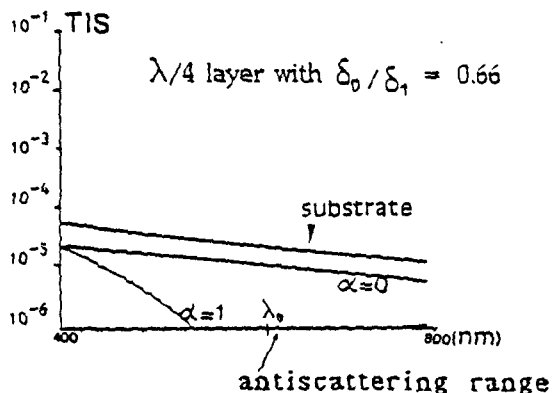


Fig 11 Variations of scattering losses (or TIS) versus wavelength for a cryolite layer with optical thickness $\lambda_0/4$, in the case where the ratio of the two roughnesses is equal to $(\delta_0/\delta_1) = 0.66$ (δ_0 is the roughness of the top interface). Antiscattering effect is stable over a wide range of wavelengths.

In the case of coatings with a high number of layers (as multiple cavity Fabry-Perot filters), the spectral variations of scattering [14] are however quite sensitive versus scattering parameters, and investigation of experimental results may be more complex.

4) Use of specific stacks

Another way to study scattering parameters consists in using particular stacks which scattering losses show a high sensitivity versus scattering parameters. Analytical calculations led us to the choice of a design made of an odd number of alternated half-wave high index and low index layers [26]. As shown in Table I, the case of perfectly correlated surfaces ($\alpha = 1$) shows no variation of scattering before and after coating, whatever the number N of layers of the stack. On the other hand, we can notice a high increase of scattering with the number of layers of the coating (by a factor 100 with 11 layers) in the case of uncorrelated surfaces ($\alpha = 0$).

Table I - Scattering losses D by reflection calculated for a glass substrate before ($N = 0$) and after coating by an odd number N of alternative high index (TiO_2) and low index (SiO_2) layers with optical thickness $\lambda_0/2$.

	N=0	N=1	N=3	N=5	N=11
$10^6 \cdot D (\alpha=0)$	23.	649.	1153.	1660.	3175.
$10^6 \cdot D (\alpha=1)$	23.	23.	24.	26.	28.

Calculation is performed at wavelength λ_0 for two extreme values ($\alpha = 0$ and $\alpha = 1$) of the crosscorrelation coefficient. We can notice that for correlated surfaces ($\alpha = 1$), there is practically no change of scattering before and after coating, whatever the number N of alternative layers. On the other hand, for uncorrelated surfaces ($\alpha = 0$), scattering highly increases with the number N of layers (a factor 100 with $N = 11$).

Some experimental results are presented in Table II and show that scattering is always reduced after coating. We have verified [26] that this can only be explained by a very high correlation ($\alpha \approx 1$) between interfaces together with a slight reduction of roughness at interfaces (near 0.7).

Table II - Scattering losses of 3 black glasses measured before ($N = 0$) and after deposition of an odd number of alternative high index (TiO_2) and low index (SiO_2) layers with optical thicknesses $\lambda_0/2$. Scattering is always reduced after coating.

	N=0	N=1	N=3	N=5
$10^6 \cdot D$	41.	9.6	10.0	13.4

V - BETTER USE OF THE MODEL

We have seen how we could have access to the key parameters (roughnesses and crosscorrelation laws) of scattering in the case of classical coatings and consequently obtain information about each interface inside the multilayer stack. The results obviously depend on the quality of the substrates used for the coating as well as on the deposition techniques that were employed, and therefore on the microstructure of the materials obtained with these techniques. This enables us to modify the deposition conditions in order to control the scattering parameters and obtain minimal scattering losses for a particular design. For example, it is preferable for a mirror to have uncorrelated roughnesses [30] while it is the contrary for a Fabry-Perot filter (in this last case, scattering can vary by a factor of 100 according to the value of the crosscorrelation coefficient). Unfortunately, as far as designs with a high number of layers are concerned (multiple cavity Fabry-Perot filters for example), the preceding specific techniques of comparison between experiment and theory are not sufficient enough to investigate experimental results since the number of scattering

parameters is too high. It is difficult for instance to point out the origin of roughness in multilayer stacks. We have shown [13, 30] in some cases that such roughness could be due both to reproduction of substrate defects (for low spatial frequencies) and to a residual roughness (for high spatial frequencies) brought by the material microstructure.

We intend here to briefly show how the theoretical model can be improved to reduce the number of parameters and to permit an easy investigation of scattering phenomena in complex coating designs.

1) Influence of substrate defects

Our experimental results show that in many cases, the anisotropy maps of the substrates are very similar before and after coating (and after deposition of Al).

In the easy case of a single layer, we even show (see section IV-2) that the two interface roughness spectra are identical in the whole range of measurable spatial frequencies. This leads us to consider that there is a relation between cause and effect [31] for the surface profiles inside the multilayer, relation which will of course depend on the quality of the substrate [29], on the microstructure [17] and thickness [29] of material layer, and also on the spatial frequency [17] of the concerned defect.

For instance, we can write the following relation:

$$h_i = \frac{1}{4\pi^2} a_{ij} * h_j$$

where h_i and h_j are profiles of interfaces (i) and (j), and (*) indicates a convolution product.

We then obtain after Fourier Transform : $\hat{h}_i(\vec{\sigma}) = \alpha_{ij}(\vec{\sigma}) \hat{h}_j(\vec{\sigma})$, $\alpha_{ij} = \text{FT} [a_{ij}(\vec{r})]$.

Consequently, the crosscorrelation coefficient α_{ij} represents the ratio of the magnitudes of the gratings of same period $C = \frac{2\pi}{\sigma}$ at interfaces (i) and (j) [19]. It varies with spatial frequency σ so that we can consider the fact that the material will act differently according to the kinds of defects that are concerned.

With this "causal" model, the number of free parameters is considerably reduced because roughness spectra and crosscorrelation laws are henceforth linked by the relation:

$$\alpha_{ij}(\vec{\sigma}) = \sqrt{\frac{\gamma_{ii}(\vec{\sigma})}{\gamma_{jj}(\vec{\sigma})}} e^{j\psi_{ij}(\vec{\sigma})}$$

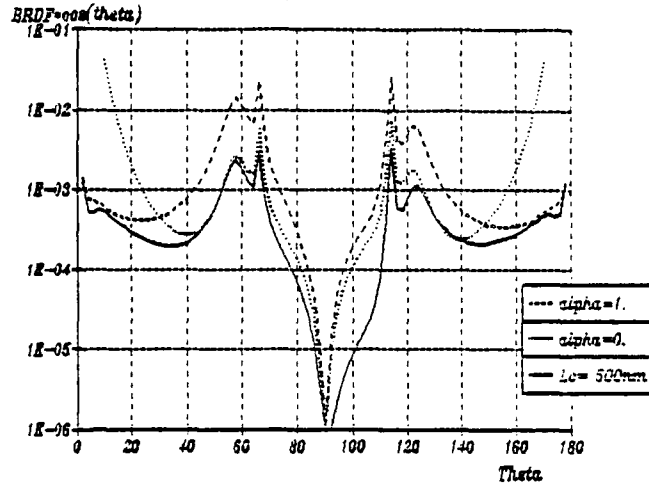
Moreover, the α_{ij} coefficients can be calculated with the $\alpha_{i,i+1}$ coefficients. As for the argument $\psi_{ij}(\vec{\sigma})$, one can consider that it is equal to zero provided that deposition of material is made near normal incidence and on rotating substrates (gratings are reproduced with no lateral shift). In the case of a quarterwave coating made of only two materials, we can also assume that each material will have the same behavior whatever the layer of the stack which is made of this material. Therefore, we have to consider only two functions a_{ij} that characterize the two materials: $\alpha_{i,i+1} = \alpha_{i+2,i+3}$.

In that way, provided that the substrate was measured before coating, the unknown parameters are the crosscorrelation functions α_{01} and $\alpha_{12}(\vec{\sigma})$. As it is probable that the greater the defect periods the better they are reproduced, we can choose for $\alpha_{ij}(\vec{\sigma})$ a slow decreasing function analogous to a low-pass filter (or other) with cut-off frequency σ_{ij}^c . We will not enter here the detail of calculation, but we will emphasize the fact that such causal model allows computation for systematic research of the parameters that show good agreement between theory and experiment. A good agreement will be obtained in that way provided that the materials do not bring an important residual roughness (due to their microstructure).

Figure 12 illustrates these results in the case of a Fabry-Perot filter. The two extreme cases ($\alpha = 0$ and $\alpha = 1$) that are generally used are also represented. With our causal model and a cut-off frequency $\sigma_c = \frac{2\pi}{L_c} = 12.6 \mu\text{m}^{-1}$, the angular scattering curve is very similar to one and other classical cases of uncorrelated ($\alpha = 0$) and correlated ($\alpha = 1$) surfaces, according to the angular range that is concerned. This is explained by the fact that scattering at low angles is due to large period defects ($\sigma \ll \sigma_c$) that are reproduced ($\alpha \approx 1$), while scattering at large angles is due to short period defects that are lost ($\alpha(\sigma) < 1$). Let us notice here that the case of

homothetic surfaces (see II-3) would lead to the easy relation $\alpha_{ij} = \frac{\delta_i}{\delta_j}$ which recalls that roughnesses and crosscorrelation laws are not independent. On the other hand, the classical case of independent roughnesses is not taken into account with this model (see section V-3).

Fig 12 - Angular scattering curve calculated at the wavelength λ_0 and at normal incidence for a Fabry-Perot filter which design is: H L H L H (6L) H L H L H where H and L are quarterwave $\lambda_0/4$ high index (ZnS) and low index (cryolite) layers. We can notice the presence of scattering peaks [14, 25]. The two extreme cases $\alpha = 0$ and $\alpha = 1$ that are represented correspond to the classical cases of correlated and uncorrelated surfaces. The curve in full line has been calculated according to the causal model and assuming that the crosscorrelation coefficient $\alpha(\sigma)$ is a slow decreasing low-pass filter with a cut-off frequency $\sigma_C = \frac{2\pi}{L_c} = 12.6 \mu\text{m}^{-1}$.



The angular range ($90^\circ \rightarrow 180^\circ$) corresponds to scattering by transmission.

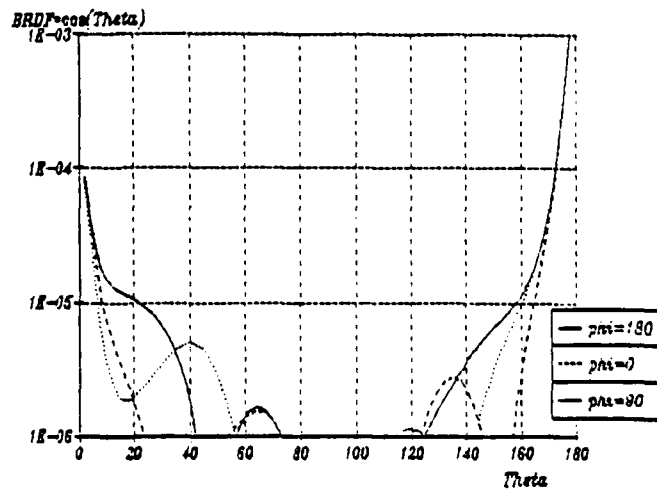
2) "Pseudo-anisotropy" effects

In spite of experimental and theoretical difficulties, we can go further to know until where the preceding causal model will be realistic. Let us consider for instance a deposition performed at oblique incidence β on a non-rotating substrate. As the material flux reaches the substrate at incidence β , the layer will grow under certain conditions in a form of columns with an angle α with respect to the sample normal ($\tan \beta = 2 \tan \alpha$ [32]).

Therefore we can consider that the different gratings are reproduced with a lateral shift (which modulus is $|\vec{a}|$) depending on the incidence β and on the layer thickness. In this case, the crosscorrelation coefficient α is not a real number and we must take into account its argument $\Psi_{ij}(\vec{\sigma}) = \vec{\sigma} \cdot \vec{a}$. As shown in fig. 13, we then observe a "pseudo-anisotropy" effect which means that scattering varies with the scattering plane ϕ that is concerned (though the surfaces are isotropic).

Experiments are under study but are quite difficult because of the high thickness of the layer; indeed we must not lose the relation between cause and effect for the surface profiles. Some results will be given later.

Fig. 13 - Angular scattering curves calculated at wavelength λ_0 and at normal incidence for a cryolite layer with optical thickness $13\lambda_0/4$ deposited at incidence $\beta = 25^\circ$ on an isotropic and non rotating substrate. The crosscorrelation coefficient α is therefore a complex number ($\Psi \neq 0$) and it appears "pseudo-anisotropy" effects, which means that scattering varies with the scattering plane ϕ .



3) Material grain size

Until now, we considered only the reproduction of substrate defects layer after layer, without taking into account a residual roughness due to the material microstructure [13, 17]. However it is possible to consider both these two effects by the relation:

$$h_{i+1}^* = \frac{1}{4\pi^2} a_{i+1,i} \cdot h_i^* + g_{i+1}$$

where the first term is relative to reproduction of defects and the second term g_{i+1} to the residual roughness brought by the material. The notation h_i^* is used here to indicate the difference with the preceding causal model.

We then obtain:

$$\eta_{ii}^* = \eta_{ii} + \sum_{(k,q)}^i \alpha_{ik} \tilde{\alpha}_{iq} \alpha_{kq} g | \hat{g}_q |^2$$

$$\eta_{ij}^* = \eta_{ij} + \sum_{\substack{k=1 \text{ to } i \\ q=1 \text{ to } j}} \alpha_{ik} \tilde{\alpha}_{jq} \alpha_{kq} g | \hat{g}_q |^2$$

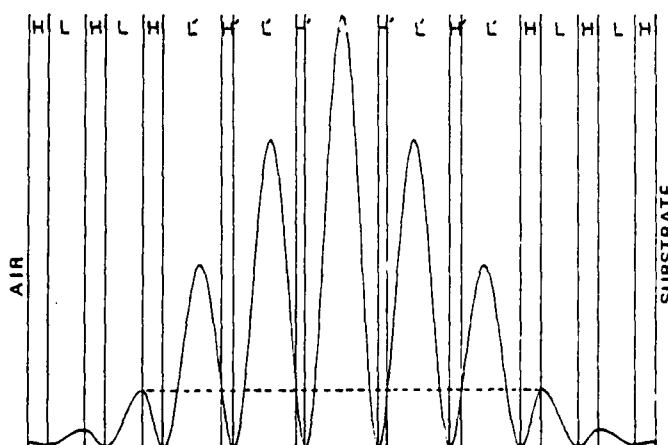
where $\alpha_{ij}g$ indicates a possible correlation between residual roughnesses at interfaces (i) and (j). In the case of a coating made of only two materials, we can assume that the residual roughnesses of the two materials are independent, so that $\alpha_{q,q+2k+1} = 0$, and therefore easy computation can be performed.

VI - MINIMAL SCATTERING LOSSES

The techniques presented in the preceding sections will permit us, owing to a better understanding of scattering phenomena, to adjust the deposition conditions in order to obtain minimal scattering losses. However, we could also try to modify the coating design so that scattering losses are reduced, without altering the required optical properties. This is quite a difficult problem, and we will limit ourselves here to the case of a simple example. For a classical mirror, it has been shown that it was possible to shift the ideal electric field in the volume of the stack by addition of particular layers on the mirror, without decreasing the reflection coefficient. In this way, absorption [33] and scattering [30] can be reduced. However, reduction of scattering is only 50% and this only occurs in the case of uncorrelated surfaces. This method can also be applied to the case of Fabry-Perot filters (Fig. 14) and scattering is then reduced by a factor 5, for uncorrelated surfaces (let us notice that the case $\alpha = 0$ can occur with substrates of high quality). However, these results are somewhat limited, and it is rather useful to search for destructive interferences between the scattered waves, as shown in section IV-2 and IV-4.

Fig. 14 - Distribution of the square of the electric field in a Fabry-Perot filter which design is:

HL HL HL' H'L' H' (2L) H' L'H' L'H LH LH The design is slightly different with respect to that of classical quarterwave Fabry-Perot filters so that the maxima of electric field [30, 33] inside the stack are shifted in the volume of the layers. Surface scattering is therefore reduced by a factor of 5 in the case of uncorrelated surfaces.



On the other hand, in particular for multi-demultiplexing in optical telecommunications [14], we often have the choice of several designs that can reach the required isolation and transmission specifications. Our theoretical calculations then enable us to choose the multiple cavity Fabry-Perot filter which leads to minimal scattering at critical directions of transmission information (Fig. 15).

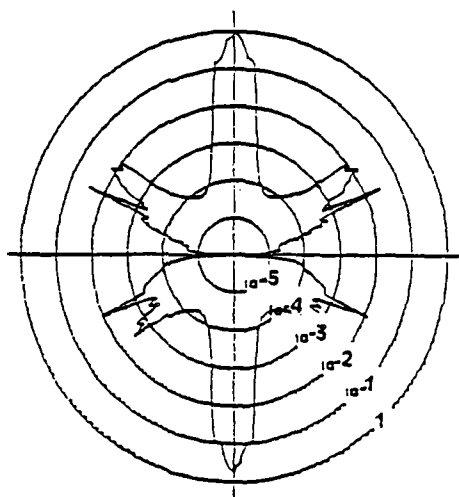


Fig. 15 - Scattering distribution from a Fabry-Perot filter.

CONCLUSION

We presented a rapid overview of the works that have been performed in our Laboratory for the study of scattering from multilayer optics. We expect promising results from other experimental and theoretical works under study.

The case of an uncoated surface appears to be well solved since we can extract the roughness, autocorrelation length and isotropy degree in the range of measurable spatial frequencies. For multilayer classical coatings, we have shown how it was possible to extract the key parameters of scattering with the help of particular techniques such as Al overcoating, antiscattering effect, variations of scattering versus wavelength, and specific stacks. These parameters (roughnesses and crosscorrelation laws) give us precious information concerning the materials microstructure, and it is therefore possible to modify the deposition conditions to obtain the finest microstructure.

In the case of complex coating design, the high number of parameters causes the comparison between theory and experiment to be extremely difficult. However, we demonstrated that a more realistic model for crosscorrelation laws permitted us to considerably reduce the number of parameters involved in the calculation; one can also search for pseudo-anisotropy effects. In a more general way, these results allow computation for systematic research of the scattering parameters that lead to the best agreement between theory and experiment, and therefore permit an easy understanding of scattering mechanisms. At last, such calculation enables us to choose, at the conception of a multi-demultiplexing system, the coating designs that lead to minimal scattering at the critical directions where information is transmitted.

References

- 1 H.A. Macleod, "The microstructure of optical thin films", Proc. SPIE, 325, 21 (1982)
M. Harris, M. Bowden, H.A. Macleod, "The relationship between optical inhomogeneity and film structure", Thin Solid Films, 57, 173 (1979)
- 2 K.H. Guenther, H.K. Pulker, "Electron microscopic investigations of cross sections of optical thin films," Applied Optics, 15, 2992 (1976)
H.K. Pulker and E. Jung, "Correlation between film structure and sorption behaviour of vapor deposited ZnS, cryolite and MgF₂ films," Thin Solid Films, 9, 57 (1971) - Thin Solid Films, 10, 163 (1972)
- 3 J.M. Bennett, "Optical scattering and absorption losses at interfaces and in thin films," Thin Solid Films, 123, 27 (1985)
- 4 C.K. Carniglia and J.H. Apfel, "Maximum reflectance of multilayer dielectric mirrors in the presence of slight absorption," J. Opt. Soc. Am. 70, 523 (1980)

- 5 J.M. Elson and J. M. Bennett, "Relation between the angular dependence of scattering and the statistical properties of optical surfaces, J. Opt. Soc. Am. 69 (1979)
- 6 J. M. Elson, J.P. Rahn, and J.M. Bennett, "Relationship of the total integrated scattering from multilayer-coated optics to angle of incidence, polarization, correlation-length, and roughness crosscorrelation properties," Appl. Opt. 22, 3207 (1983)
- 7 J.P. Borgogno, P. Roche and G. Albrand, "Un modèle de couche inhomogène valable dans un large domaine spectral et pour une incidence quelconque, Thin Solid Films, 146, 145 (1987)
J.P. Borgogno, F. Flory, P. Roche, B. Schmitt, G. Albrand, E. Pelletier, H.A. Macleod, "Refractive index and inhomogeneity of thin films," Appl. Opt. 23, 3567 (1984)
- 8 E. Pelletier, "Optical characterization of thin films by guided waves," Conf. Presented at: "Fourth topical meeting on OPTICAL INTERFERENCE COATINGS", April 12-15, 1988, Tucson, Arizona - Submitted to Applied Optics
- 9 J.P. Borgogno, B. Lazaridès, P. Roche, "An improved method for the determination of the extinction coefficient of thin film materials," Thin Solid Films, 102, 209 (1983)
J.P. Borgogno, B. Lazaridès, E. Pelletier, "A method for determining the optical constants, inhomogeneity and thickness of dielectric films for optical applications," Proceedings of the eighth International Vacuum Congress - Cannes, Sept. 22-26, 1980 - Supplément à la revue: Le Vide, les Couches Minces, 1, Thin Films, 385-388
- 10 M. Commandré, L. Bertrand, G. Albrand, E. Pelletier, "Measurement of absorption losses of optical thin film components by Photothermal Deflection Spectroscopy," SPIE Proceedings, "Optical Components and Systems", 805, 128 (1987)
- 11 B. Schmitt, J.P. Borgogno, G. Albrand and E. Pelletier, "In situ and air index measurements: influence of the deposition parameters on the shift of TiO_2/SiO_2 Fabry-Perot filters.," Appl. Opt., 25, 3909 (1986)
- 12 F. FLORY, G. ALBRAND, C. MONTELYMARD, E. PELLETIER, "Optical study of the growth of Ta_2O_5 and SiO_2 layers obtained by Ion Assisted Deposition," SPIE Proceedings, Thin Film Technologies II, 652, 248 (1986)
- 13 P. ROCHE, C. AMRA, E. PELLETIER, "Measurement of scattering distribution for characterization of the roughness of coated or uncoated substrates," SPIE Proceedings, Thin film Technologies II, 652, 256-263, (1986)
- 14 C. GREZES-BESSET, C. AMRA, B. COUSIN, G. OTRIO, E. PELLETIER, R. RICHIER, "Etude de la diaphonie d'un système de démultiplexage par filtres interférentiels. Conséquences de la diffusion de la lumière par les irrégularités des surfaces optiques," Ann. Télécommun., 43, 135 (1988)
C. Grèzes-Besset, "Conception et réalisation de filtres optiques adaptés au démultiplexage pour les télécommunications par satellites. Influence de la diffusion sur la limitation des performances," Thèse de doctorat, Université d'Aix-Marseille III (1987)
- 15 P. ROCHE, E. PELLETIER, "Characterizations of optical surfaces by measurement of scattering distribution," Appl. Opt., 23, 3561 (1984)
- 16 P. BOUSQUET, F. FLORY, P. ROCHE, "Scattering from multilayer thin films: theory and experiment," J. Opt. Soc. Am., 71, 1115 (1981)
- 17 C. AMRA, G. ALBRAND and P. ROCHE, "Theory and application of antiscattering single layers: antiscattering antireflection coatings.," Appl. Opt. 25, 2695 (1986)
- 18 P. ROCHE, E. PELLETIER, G. ALBRAND, "Antiscattering transparent monolayers: theory and experiment," J. Opt. Soc. Am. 1, 1032 (1984)
- 19 C. AMRA, P. ROCHE, E. PELLETIER, "Interface roughness cross-correlation laws deduced from scattering diagram measurements on optical multilayers: effect of the material grain size," J. Opt. Soc. Am - B., 4, 1087 (1987)
- 20 J.M. Elson, J.P. Rahn and J.M. Bennett, "Light scattering from multilayer optics: comparison of theory and experiment," Appl. Opt. 19, 669 (1980)
- 21 J.M. Elson, "Angle resolved light scattering from composite optical surfaces," Proc. Soc. Photo. Opt. Instrum. Eng. 240, 296 (1980)
- 22 C. Amra, "Développement et comparaison de deux théories vectorielles de la diffusion de la lumière par des surfaces peu rugueuses. Application à l'étude des surfaces et empilements de couches diélectriques," Thèse de doctorat, Université d'Aix-Marseille III (1986)

- 23 J.M. Bennett, "Scattering and surface evaluation techniques for the optics of the future," Optics News, July 1985
- 24 C. AMRA, C. GREZES-BESSET, P. ROCHE, E. PELLETIER, "Description of a scattering apparatus- Application to the problems of characterization of opaque surfaces. - *Conf.* presented at: "Fourth topical meeting on OPTICAL INTERFERENCE COATINGS", April 12-15, 1988, Tucson, Arizona - Submitted to Applied Optics
- 25 E. Pelletier, P. Roche, C. Grèzes-Besset, "Measurement of scattering curves of coated or uncoated optical surfaces: experimental techniques for determining surface roughnesses. *Conf.* presented at "The International Congress on Optical Science and Engineering", Hamburg, 19-23 September 1988. This issue.
- 26 C. AMRA, "Minimizing scattering in multilayers: technique for searching optimal realization conditions. - *Conf.* presented at "19th Annual Boulder Damage Symposium" - Oct. 26-28, 1987, Boulder, Colorado, To be published in "laser induced damage in optical materials"
- 27 J.P. BORGOGNO, E. PELLETIER, "Determination of the extinction coefficient of dielectric thin films from spectrophotometric measurements," *Conf.* presented at: "Fourth topical meeting on OPTICAL INTERFERENCE COATINGS", April 12-15, 1988, Tucson, Arizona - Submitted to Applied Optics
- 28 L. Mattsson, "Light scattering and characterization of thin films," SPIE Proceedings, 652 (1986)
- 29 P. ROCHE, P. BOUSQUET, F. FLORY, J. GARCIN, E. PELLETIER, G. ALBRAND, "Determination of interface roughness cross-correlation properties of an optical coating from measurements of the angular scattering," J. Opt. Soc. Am., 1, 1028 (1984)
- 30 C. AMRA, "Scattering distribution from multilayer mirrors - Theoretical research of a design for minimum losses - *Conf.* presented at: "18th Annual Boulder Damage Symposium" - Nov. 3-5, 1986, Boulder, Colorado - To be published in "Laser induced damage in optical materials"
- 31 R.B. Sargent, Dar-Yuan Song and H.A. Macleod, "Computer simulation of substrate defect propagation in thin films," Proc SPIE, 821 (1987)
- 32 A.G. Dirks, H.J. Leamy, Thin Solid Films, 47, 219 (1977)
- 33 J. H. Apfel, "Optical coating design with reduced electric field intensity," Appl. Opt. 16 (1977)

Comparison of the properties of titanium dioxide films prepared by various techniques

Jean M. Bennett, Emile Pelletier, G. Albrand, J. P. Borgogno, B. Lazarides, Charles K. Carniglia, R. A. Schmell, Thomas H. Allen, Trudy Tuttle-Hart, Karl H. Guenther, and Andreas Saxer

Fourteen university, government, and industrial laboratories prepared a total of twenty pairs of single-layer titanium dioxide films. Several laboratories analyzed the coatings to determine their optical properties, thickness, surface roughness, absorption, wetting contact angle, and crystalline structure. Wide variations were found in the optical and physical properties of the films, even among films produced by nominally the same deposition techniques.

1. Introduction

This paper began as a project of the Optical Society's Optical Materials and Thin Films (OM&TF) Technical Group. The question was asked "What are the optical constants of a titanium dioxide thin film?" To answer it, fourteen university, government, and industrial laboratories made single layer TiO_2 films using seven different processes: electron-beam (E-B) evaporation, ion-assisted deposition (IAD), ion-beam sputter deposition (IBSD), activated-reactive evaporation (ARE), ion or plasma plating (IP), rf diode sputtering (RFS), and dip coating from a solution using the Schott process: Dip).¹ Commercial grade polished fused silica substrates were provided to each group. Two coated samples were made of each type of film and the complete set of samples was then divided into two groups for measurement and analysis.

Initially, the optical properties of the films were analyzed: the index of refraction, absorption and inhomogeneity as a function of wavelength, along with the thickness as determined by spectrophotometry. One set of samples was measured and analyzed at Ecole Nationale Supérieure de Physique de Marseille. This set of samples and the group at Marseille that

performed the analysis are both designated as Group A. Measurements were made on the second set of samples by the Research Department at Optical Coating Laboratory, Inc. (OCLI), and the data were analyzed at the Developmental Optics Facility of the U.S. Air Force operated by Martin Marietta Astronautics Group in Albuquerque, N.M. This second set of samples and the groups at OCLI and Martin Marietta are both called Group B.

The results of the optical properties measurements of twenty different titania films were reported by each group at the OM&TF Technical Group Meeting at the 1986 Annual Meeting of the OSA. The optical constants of different films showed some correlation with deposition method, but also indicated that there was considerable influence of the coating system, coating conditions, and operator.

During the following year the films in Group B were subjected to a number of additional measurements. These measurements included surface roughness, absorption (using photothermal deflection spectroscopy), wetting contact angle, and film microstructure as determined by Raman spectroscopy. The results were reported at the 1987 Annual Meeting of the OSA.

This paper reports on the entire project, including the film preparation, the measurements and analysis techniques, and the results. We found that the optical and physical properties of various films of the same material were, in fact, quite different. Thus, the initial question about the optical constants of a titanium dioxide film does not have a unique answer.

A related question might inquire about which deposition process produced the best films. The results of the study indicate that the answer to this question depends on the criteria that are used to define the term, best: high refractive index, low absorption, low scatter, etc. We conclude that there is enough variation in the observed properties that titania films can be optimized for a wide range of applications.

Jean Bennett is with Naval Weapons Center, Michelson Laboratory, China Lake, California 93555. Charles Carniglia and R. A. Schmell were with Martin Marietta Astronautics Group, Laser Systems Technology, P.O. Box 9316, International Airport, Albuquerque, New Mexico 87119; they are now with S. Systems Corporation at the same address. Thomas Allen and T. Tuttle-Hart are with Optica Coating Laboratory, Inc., Santa Rosa, California 95407. Karl Guenther is with University of Central Florida, Center for Research in Electro-Optics & Lasers, Orlando, Florida 32826. Andreas Saxer is at 103 Innrain, 6020 Innsbruck, Austria. The other authors are with Ecole Nationale Supérieure de Physique de Marseille, Laboratoire d'Optique des Surfaces et des Couches Minces, Domaine Universitaire de Saint-Jerome, 13397 Marseille, CEDEX 12, France.

Received 13 December 1988.

II. Film Preparation

The substrates provided to all participants were 25.4 mm (1 in) diam by 1.6 mm (0.063 in.) thick polished fused silica substrates of the type frequently used for commercial coatings. Highly polished surfaces (bowl feed polished, for example) would have been preferable for the evaluation of some properties such as surface roughness and scatter. However, the initial intent of the project was to look at the optical properties of typical coatings rather than the very best ones that could be made under ideal laboratory conditions. (Also the cost of super smooth substrates was about ten times higher.) Even though the substrate roughness was non-negligible, it was possible in most cases to measure the added roughness from the films. The starting material for the films was supplied by each participating group, since each process required different forms of titanium oxide or titanium metal.

Each participant provided two samples coated in the same run with a nominal optical thickness of 5 quarter waves at 550 nm. This thickness was chosen so that a spectral transmittance scan over the region of transparency of the titanium film-silica substrate combination would contain a sufficient number of maxima and minima to allow the refractive index to be determined accurately. The participants had been told, however, that the actual thickness was relatively unimportant. As is shown in Sec. IV, the average wavelength for which the films had an optical thickness of five quarter waves was close to 570 nm.

The participating groups and the types of films they made are listed in Table I. They had all been asked to provide the parameters of the processes they were using if the information was not company proprietary. These are listed in Table II.

Most of the coating processes are well known. However, a brief summary is given here. Excellent reviews of most of the ion assisted processes have been given by Martin² and Matthews.³ There are additional excellent review articles on ion beam sputter deposition,⁴ reactive ion plating,^{5,6} and dip coating.⁷ Optical properties of titania films prepared by different techniques are summarized by Martin;² the improvement in the optical properties by intermittent ion bombardment has also been discussed.^{8,9}

Electron-Beam (E-B) Deposition: The substrates are placed in a vacuum chamber with a base pressure in the 10^{-6} mbar range. The source is an electron beam gun into which titanium oxide is placed. A focused beam of electrons in the gun melts the material; it evaporates onto the substrates which have been heated to about 300 °C. To improve the stoichiometry, the deposition is generally done in a partial pressure of oxygen of $0.6-3 \times 10^{-4}$ mbar.¹⁰ Typical evaporation rates are 0.2-0.8 nm/s. Films deposited using an electron beam gun or other thermal sources have a columnar microstructure¹¹ which can be porous. The resulting surface roughness and grain boundaries produce light scattering.¹² For this reason, other techniques have been developed to make denser films whose properties are closer to that of the bulk material.

Table I. Suppliers of Titania Films

Type	Sample #	Group
IP	165.166	Balzers AG, FL-9496 Balzers, Liechtenstein, W. Thoen, M. Kasper
RFS	093.145	Battelle, Pacific Northwest Division, Battelle Blvd., P.O. Box 999, Richland, WA 99352, W. T. Pawlewicz
IBSD	078.079	Colorado State University, Department of Physics, Fort Collins, CO 80523, James R. Sites, Rong Rajkorkarn
Dip	213a,213b	Denton Vacuum, Inc., Cherry Hill Industrial Center, Cherry Hill, NJ 08003, Peter R. Denton, Anthony Musset
E-B, ARE	052.057	Indian Institute of Science, Instrumentation and Services Unit, Bangalore 560 012, India, S. Mohan
E-B	025.023	Laybold AG, Dept. UC 2, Siemensstr. 100, 8755 Alzenau, West Germany, R. Hermann, W. Klug
IAD	024.022	Martin Marietta Astronautics Group, Laser Systems Technology, P.O. Box 9316, International Airport, Albuquerque, NM 87119, R. A. Schmeil
E-B	094.097	National Institute of Standards and Technology (formerly National Bureau of Standards), Bldg. 223, Room A329, Gaithersburg, MD 20899, Albert Feldman, Ed Farabaugh
E-B	201.202	Optical Coating Laboratory, Inc., 2789 Northpoint Pkwy, Santa Rosa, CA 95407, T. H. Allen, T. Tuttle-Hart
IBSD	120.122	Optical Sciences Center, Univ. of Arizona, Tucson, AZ 85721, H. A. Macleod, John Lehan
IP	114.115	
E-B	138.140	
IAD	137.139	
IAD	143.144	
E-B	036.038	Opus Mechanik, Inc., 425 North Drive, P.O. Box 361907, Melbourne, FL 32935, Ron R. Willey
IBSD	135.136	Rockwell International, Electronics Operations, Autonetics Marine Systems Division, 3370 Marlin Ave., Mail Sta. GE 14, Anaheim, CA 92803, Austin N. Kalb, Mark Mildebrath
E-B	003.002	Spectra Physics, Inc., Opus Division, 1250 West Middlefield Rd., Mountain View, CA 94042, Gary DeBell
E-B	006.005	
IAD	013.014	University of New Mexico, Dept. of Electrical and Computer Engr., Albuquerque, N. Mex. 87131, J. R. McNeil, Forrest Williams
IAD	011.012	

E-B	Electron Beam Deposition	RFS	RF Diode Sputtering
IAD	Ion Assisted Deposition	IP	Ion (or Plasma) Plating
IBSD	Ion Beam Sputter Deposition	Dip	Schott Dip Process
ARE	Activated Reactive Evaporation		

* Present address: 4718 Reeves Road, Ojai, CA 93023

Table II. Coating Parameters for Titania Films

Type	Sample #	Base Pressure [10 ⁻⁶]mbar	Temp °C	Oxygen Pressure [10 ⁻⁶]mbar	Rate nm/s	E gun kV	Ion gun mA	Notes
E-B	003.002							a
	006.005	1	300	0.5	0.2	10.5		b
	201.202	13	300	2.6	0.2	8.4		c
	025.023	13	300	2.6	0.4			
	138.140	2.6	136	2.6	0.2			
	052	1.3	75	0.6	0.2	9.5	0.06	d
	094.097	4	225	1.3	0.25	6.5	0.18	
	036.038	26	300	2.6	0.3	7.0	0.04	
IAD	024.022	13	50	2.6	0.16	9.4	750	e
	137.139	2.6	136	2.6	0.4		300	f
	143.144	2.6	137	2.6	0.4		300	f
	013.014	0.08	175	2	0.15	6.4	0.16	g
	011.012	0.08	275	1.3	0.15	6.4	0.16	h
IBSD	135.136	0.03		2.6	0.093		1300	i
	078.079	0.6	50	0.6	0.025		1100	j
	120.122	2.6	100	1.2			1400	k
ARE	057	1.3	75	0.6	0.1	9.5	0.06	d
RFS	093.145	0.1	250	40	0.1		1450	l
IP	165.166							
	114.115							
Dip	213a,b							

Notes

- a Small chamber
- b Large chamber
- c Ion cleaned substrates
- d Cryopumped system
- e 50 μ A/cm²
- f Intermittent
- g 30 μ A/cm²
- h 40 μ A/cm²
- i Neutral beam
- j Argon $h \times 10^{-3}$ mbar; thickness as given noted in films
- k IAD 50 V, 200 mA
- l 3 W/cm², Argon 2.2×10^{-3} mbar, substrate bias voltage 100 V

Ion-Assisted Deposition (IAD): A beam of ions, generally argon, is directed onto the substrate along with the arriving titania molecules. The ion beam is usually produced by a Kaufmann-type ion source. The ions break up the normal columnar growth and densify the film by impulse transfer.¹³ Films produced by IAD have smoother surfaces and show less grain structure. Hence they have lower scattering levels than films produced by electron beam deposition.

Ion-Beam Sputter Deposition (IBSD): A beam of energetic argon ions is used to sputter material from a titanium metal or titanium oxide target onto the substrates. The argon beam is produced by admitting argon gas into an ion gun at a pressure of about 10^{-2} mbar. Electrons from a thermionic emitter ionize the gas. Argon ions from the source (having energies in the 1000 to 1400 eV range) are extracted into the coating chamber using dual grids to form a well-defined ion beam which is directed at the sputtering target. The coating chamber is differentially pumped to a back pressure in the range of 10^{-4} to 5×10^{-5} mbar. Oxygen is usually also admitted at a partial pressure of $1-2 \times 10^{-4}$ mbar to react with the sputtered material. In dual ion beam sputtering, the second ion source bombards the growing titania film with low-energy oxygen ions to control its stoichiometry or for substrate precleaning. The low energy of the oxygen ions (50-100 eV) minimizes coating damage. Films produced by IBSD are dense and homogeneous; film density can be close to that of the bulk material.

Activated Reactive Evaporation (ARE): Titania films are made using an electron beam gun to evaporate titanium oxide onto the substrates in a reactive gas atmosphere. An additional discharge source is used through which the reactive gas passes. The reactive gas is ionized or excited and emerges from a nozzle. It then impinges on the substrate along with the coating material in vapor form. The deposition in the presence of ionized and excited gas enhances the reactivity, thereby ensuring complete oxidation and improving the stoichiometry of the films. As a result, the films are nearly absorption free. The energy of the ions is so low that it causes minimum disturbance (dissociation) to the growing film.

Ion Plating or Plasma Plating (IP): In this process titanium oxide or titanium metal is melted in an electron beam evaporator. The E-B crucible serves as the anode of a low-voltage, high-current plasma arc which is maintained with argon gas at about 2 mbar pressure in the source compartment. A hot cathode ionizes the argon gas. The pressure differential at a 1-2 mm diam. hole leading to the main vacuum chamber (at a background pressure below 10^{-6} mbar) extracts the argon plasma. Oxygen is admitted at a pressure of $\sim 10^{-3}$ mbar to react with the titanium metal ions at the substrate surface and produce titanium dioxide. The large electron current formed in the plasma discharge not only ionizes the vapor above the crucible (M^+ , MO^+) but also the reactive gas in the main chamber (O_2^+). The plasma sheath thus produced in the main

chamber is in contact with the dielectric substrates which sit on isolated holders. Electrons leaving the plasma more easily than the heavier ions charge the substrates negatively with a self bias of -5 V to -60 V. This bias attracts and accelerates the positive ions (titanium vapor, oxygen and argon) from the plasma environment. The impact of ions in this energy range densifies the growing film by a momentum transfer process.¹⁴ Resputtering does not seem to occur except possibly as preferential sputtering from asperities protruding from the film surface and of coadsorbed impurities. This process helps to make the film smooth and eliminate impurities such as water vapor.

RF Diode Sputtering (RFS): An rf sputtering technique has been used at Battelle Pacific Northwest Laboratories¹⁵ for depositing metal and dielectric films. Titanium dioxide is produced by rf sputtering a titanium disk in a mixture of argon and oxygen at a total pressure of ~ 0.03 mbar. The substrates are positioned on a second disk, located parallel to the first disk, and ~ 30 mm away. The substrate holder may also be an rf electrode. Rf power applied to the source electrode induces a negative bias of ~ 1500 volts, causing Ar^+ ion bombardment and sputtering of titanium and oxygen atoms from the oxidized titanium surface by momentum transfer. The atoms travel to the substrate with energies of about 10 eV, and condense on the substrate to form a dense film. Activated oxygen produced in the interelectrode discharge assures complete reaction and stoichiometry. Any desired mixed phase composition (x anatase, $1-x$ rutile) can be made, from pure anatase to pure rutile, by selection of the oxygen percentage in the sputtering gas. Higher oxygen percentages and rf substrate bias (increased oxygen activation) produce more rutile phase. Grain size is adjustable over the range from amorphous (<50 Å) to 600 Å by selection of the rf source power (substrate temperature).

Dip Coating (Dip): Dip coating is entirely different from the vacuum processes described previously. An organometallic compound (metal alkoxide) is made in solution; it contains titanium and an organic radical. The sample is dipped into the solution and the excess liquid is drained off. The sample is then exposed to moist air to hydrolyze the alkoxide to an oxide. Next the film is heated to 700-800°C to drive off the remaining organic materials and to densify the film. The organometallic solution can be made to favor a high or low refractive index, dense or porous films. The film made for this study was dip coated from a solution designed to produce low index anti-reflection coatings.

III. Measurements and Analysis

A. Optical Constants

1. Wideband Spectrophotometric Method

The method used by Group A at Marseille to obtain n , k , and the inhomogeneity $\Delta n/n$ has been described previously¹⁶⁻¹⁹ and is summarized here. Reflectance and transmittance were measured at 151 different wa-

wavelengths in the spectral range 400–1000 nm using a double-grating spectrometer designed and constructed specifically for measurements of optical constants. The average angle of incidence was 2° , and the optical beam was close to being parallel ($f/20$). The illuminated area on the sample was a rectangle $4 \times 6.8 \text{ mm}^2$. The R and T measurements were equally spaced in wavenumbers (cm^{-1}) so the wavelength intervals varied from 1.6 nm at the short wavelength end to 9.9 nm at the long wavelength end.

Since the substrates were not wedged as they were for the measurements in Ref. 16, a correction had to be made for the reflection from the back surface of the substrate. An identical uncoated substrate was used for this purpose. The measurements and analysis are as follows: The transmittance τ_0 of the bare nonabsorbing substrate is

$$\tau_0 = T_0 T_r / (1 - R_0 R_r), \quad (1)$$

where T_0 and R_0 are the transmittance and reflectance, respectively, at the front surface, and T_r and R_r are the transmittance and reflectance at the rear surface (see Fig. 1). The transmittance τ_c of the coated substrate is

$$\tau_c = T_c T_r / (1 - R_c R_r), \quad (2)$$

where T_c and R_c are the transmittance and reflectance, respectively, at the surface coated with the titanium dioxide film.

The reflectance for the bare substrate is

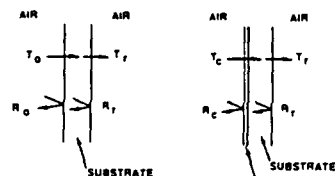


Fig. 1. Diagrams showing the quantities used in the calculations of the optical constants of the titania films. The T s and R s are intensity transmittances and reflectances, respectively.

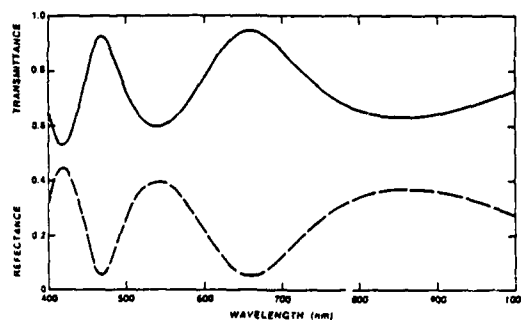


Fig. 2. Derived transmittance T_c and reflectance R_c for IBSD film #120 measured by Group A.

$$\rho_0 = R_0 + T_0^2 R_r / (1 - R_0 R_r), \quad (3)$$

and for the film-coated surface is²⁰

$$\rho_c = R_c + T_c^2 R_r / (1 - R_c R_r), \quad (4)$$

For a nonabsorbing substrate

$$R_0 + T_0 = 1, \quad (5)$$

from which it follows that

$$T_0^2 - R_0^2 = (T_0 - R_0)(T_0 + R_0) = T_0 - R_0. \quad (6)$$

At each wavelength, the quantities measured are τ_c , τ_0 , ρ_c and ρ_0 . Then with the ratios $Q_T = \tau_c / \tau_0$ [Eqs. (1) and (2)], and $Q_R = \rho_c / \rho_0$ [Eqs. (3) and (4)], and Eq. (5), R_c and T_c can be determined without any approximations. The relation for T_c is

$$T_c = \beta + \alpha R_c, \quad (7)$$

where $\beta = T_0 Q_T / (1 - R_0 R_r)$ and $\alpha = -R_r \beta$.

The expression for R_c is

$$R_c = (\gamma Q_R - \beta^2 R_r) / (1 - R_0 R_r), \quad (8)$$

where $\gamma = [R_0 + R_r(T_0 - R_0)] / (1 - R_0 R_r)$.

For fused silica substrates, the reflectance is given by

$$R_0 = R_r = (1 - n_s)^2 / (1 + n_s)^2, \quad (9)$$

where the refractive index n_s of the fused silica is assumed to be known (from a handbook or glass catalog). The value for T_0 is obtained from Eq. (5) if the substrate is nonabsorbing. It is also possible to take into account absorption in the substrate, but the calculations and calibration are more tedious.

Since R_c and T_c are the reflectance and transmittance of the TiO_2 film between two semiinfinite media—fused silica and air—the values obtained from the above analysis can be used for theoretical calculations of the optical constants of the film. (The angle of incidence in the spectrometer was 2° . In the calculations we assume the case of normal incidence.)

The accuracy of the measured reflectance and transmittance of the TiO_2 films was lower than it would have been had the films been deposited on wedged substrates. On plane parallel substrates the uncertainties in R and T were about ± 0.003 .

An example of reflectance and transmittance data for IBSD TiO_2 film #120 is shown in Fig. 2; digitized reflectance and transmittance data were recorded to four decimal places, and were then used to calculate the optical constants.

For the calculations, a linear variation of the refractive index is assumed throughout the thickness of the layer, and the three following parameters are determined simultaneously:

- (1) The mean complex index of refraction $n^* = n - ik$, which is a function of the wavelength λ .
- (2) The variation $\Delta n / n$ of the refractive index in the thickness of the layer, with the sign convention $\Delta n = n_0 - n_s$, where n_0 is the refractive index at the air-film interface and n_s at the film-substrate interface.
- (3) The geometrical thickness d .

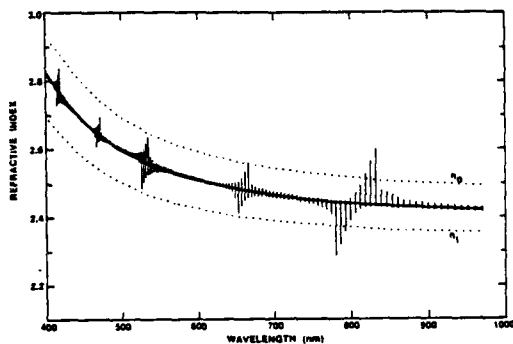


Fig. 3. Calculated refractive index versus wavelength for IBSD film #120 measured by Group A. The solid curve is the average refractive index, and upper and lower dotted curves are n_0 at the air-film interface and n_1 at the film-substrate interface, respectively. The error bars were calculated assuming uncertainties of ± 0.003 in both T_c and R_c .

For the initial calculations, approximate values for n can be obtained from R_c or T_c . Values of k were calculated using the method described in Ref. 18. In the inhomogeneity calculation, the film is split into ten sublayers of equal (physical) thickness with different refractive index n . The extinction coefficient k is assumed to remain constant for each sublayer. Scattering losses are not taken into account in the calculations; the value obtained for the extinction coefficient assumes that all significant losses are caused by absorption. The final values for n , k , and $\Delta n/n$ for each wavelength, and the thickness d of the film, were automatically calculated using the method described in Refs. 18 and 19.

An example of calculated values of n vs λ for TiO_2 film #120 is shown in Fig. 3. The error bars are based on the assumption that the errors in R_c and T_c were each ± 0.003 . The upper dotted curve is the calculated refractive index n_0 (at the air-film interface), while the lower dotted curve is the calculated refractive index n_1 (at the film-substrate interface). Further details of the measurements and the fully automated calculations are given in Refs. 16–19.

Finally, it is convenient to express n as a function of wavelength in the form of a Cauchy function such as

$$n = A + B/\lambda^2 + C/\lambda^4, \quad (10)$$

where the coefficients A , B , and C are obtained during the calculations. The refractive indices for most films measured by Group A are given in this form in Table IV in Sec. IV.

2. Modified Valeev Turning Point Method

The method of obtaining n and k used by Group B (OCLI and Martin Marietta) has also been described previously.¹⁶ However, the main points are given here. Each sample was scanned in transmission and

reflection over the spectral range 350–900 nm using a Cary 17-DX spectrophotometer interfaced to a Hewlett Packard 9825T desk-top computer. The sample was in a moderately converging $f/5.6$ beam, and the illuminated area on the sample was a rectangle ~ 4 –5-mm long and 1-mm wide. The wavenumber spacing between data points was 81.6 cm^{-1} . The transmittance was measured using a procedure similar to that used by Group A: The transmittance τ_c of the coated part and τ_0 of an uncoated fused silica reference piece (sample #126) were measured, and the ratio $Q_T = \tau_c/\tau_0$ was used in the analysis. By using this ratio, the effect of substrate absorption was minimized. The reflection losses for the uncoated substrate and for the coated sample were calculated using the known refractive index vs wavelength for used silica. These were taken into account in the analysis.

The film reflectance was measured by using a specially designed single bounce reflectance attachment on the spectrophotometer. In order to balance the sample and the reference beams, a similar single bounce reflectance attachment with an uncoated sapphire substrate was used in the reference beam. The light beam was incident on the sample at 10° although the deviation from normal incidence was ignored. Only the reflectance from the first surface of the sample was measured. The second surface reflection was eliminated by attaching a fused silica wedge onto the back of the sample with index matching fluid. To eliminate the effects of variations in detector sensitivity, source intensity, etc. with wavelength, an uncoated BK-7 wedge was scanned for the background. A new background scan was run for every four samples.

The reflectance R_c of the titania film was determined from the relation

$$R_c = \rho'_c R_b / \rho'_b, \quad (11)$$

where ρ'_c is the measured reflectance of the titania-coated substrate and ρ'_b is the measured reflectance of the BK-7 reference wedge. The primes indicate that ρ'_c and ρ'_b are measurements of the reflectance of a single surface and do not include the second surface reflection. The term R_b is the theoretical reflectance of a BK-7 surface calculated from an expression similar to Eq. (9) using the index of the BK-7 glass.

Values of n , k and the inhomogeneity $\Delta n/n$ were determined using a modified turning point method described in detail in Ref. 16, as adapted from the work of Valeev.^{21,22} This method uses the transmittance values at the turning points (maxima and minima in the transmittance vs wavelength curve) and gives the optical constants only at the half wave points. The method was extended to take into account inhomogeneity in the films. Turning points were determined after the transmittance ratio data Q_T had been smoothed using eleven points for the smoothing process.²³ The steps in the analysis were as follows:

(1) Transmittance ratios at the minima were interpolated to the wavelengths of the maxima, and were designated $Q_{T\text{int}}$.

(2) The average value of n and an approximate value of k were determined at the half wave points from

Q_{Tmax} , Q_{Tmin} , λ , and m using the method of Valeev.^{21,22} Here m is the order of interference of the maximum at which the calculations are being made.

(3) A more accurate value of k was determined from the relation

$$k = nA/2\pi m, \quad (12)$$

where the absorbance A is given by

$$A = 1 - R_{cmin} - T_{cmax}. \quad (13)$$

R_{cmin} is the reflectance of the coated surface measured at the minimum corresponding to the m th order maximum of Q_T and T_{cmax} is the maximum transmittance of the coating only, determined in a manner analogous to Eq. (7).

(4) The degree of inhomogeneity $\Delta n/n$ was determined from the reflectance minima using the relation

$$\Delta n = n(R_{cmin} - R_0)/(4.4R_0), \quad (14)$$

where $\Delta n = n_0 - n_i$ as before and it is assumed that the average value of n determined in step (2) is given by $n = (n_0 + n_i)/2$. The factor 4.4 has been arrived at empirically.¹⁶

(5) The physical thickness d of the film was calculated at each half point from the relation

$$m\lambda/2 = nd, \quad (15)$$

where nd is the optical thickness of the film.

Graphs of n and k vs λ are given in Figs. 4 and 5 for two films prepared by ion beam sputter deposition. Note that the data points for n and k are obtained at the wavelengths corresponding to integral multiples of a half wave optical thickness of the films (maxima in the transmittance vs wavelength curves). The inhomogeneity for n and uncertainty in k are determined at the wavelengths corresponding to odd integral multiples of a quarter wave optical thickness of the films (minima in the transmittance vs wavelength curves). In Fig. 4 the film has a small but nonzero k value which decreases with wavelength, while the k value for the film in Fig. 5 is large at the shortest wavelength but smaller elsewhere. The bars associated on the refractive index curves extend from n_i at the lower end to n_0 at the upper end, indicating the degree of inhomogeneity. The bars on the k curves indicate the uncertainty in the k values.

B. Film Absorption

In addition to obtaining values of the extinction coefficient k from measurements of the film reflectance and transmittance, film absorption was measured using photothermal deflection spectroscopy.²⁴ A schematic diagram of the apparatus is shown in Fig. 6. The film-coated substrate is placed in a cell containing CCl_4 which has a large temperature coefficient of the refractive index. An argon ion laser pump beam ($\lambda = 514$ nm) or a focused Xe light source at normal incidence heats the film. The He-Ne laser probe beam ($\lambda = 633$ nm) is directed through the CCl_4 parallel to the sample and very slightly displaced from it. As the film absorbs the pump light it conducts heat to

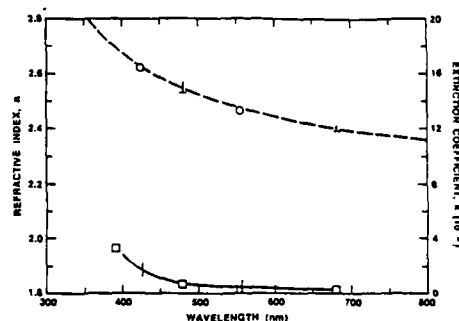


Fig. 4. Calculated refractive index n (upper curve) and extinction coefficient k (lower curve) vs wavelength for IBS film #136 measured by Group B. The vertical bars on the n curve indicate the wavelengths where the inhomogeneity was measured; the length of the bars indicates the difference $n_0 - n_i$. The length of the vertical bars on the k curve indicates the uncertainty in k .

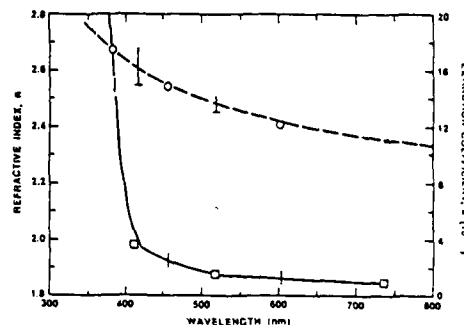


Fig. 5. Calculated refractive index n (upper curve) and extinction coefficient k (lower curve) vs wavelength for IBS film #079 measured by Group B. The vertical bars have the same meanings as in Fig. 4.

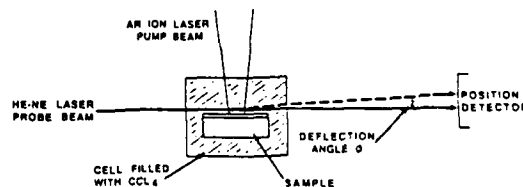


Fig. 6. Schematic diagram of the photothermal deflection spectroscopy apparatus.

the CCl_4 , changing its refractive index. This causes the He-Ne probe beam to deviate slightly. The change of position is sensed by a position detector.

The relationship between the deflection angle ϕ , shown in Fig. 6, and the absorbance of the sample is

$$\phi = \left(\frac{L}{n_0} \right) \left(\frac{dn}{dT} \right) \left(\frac{k_d}{(\kappa_d k_d + \kappa_s k_s)} \right) \exp(-k_d z_0) I_0 A = \left(\frac{L}{n_0} \right) \left(\frac{dn}{dT} \right) \left(\frac{dT}{dz} \right) \quad (16)$$

where n_0 is the refractive index of CCl_4 at room temperature, (dn/dT) is the change of n_0 with temperature, L is the interaction length between the probe and pump beams, i.e., the pump beam diameter on the sample, κ_d or κ_s is the thermal conductivity of the deflecting medium or the substrate material, k_d or k_s the thermal diffusion coefficient of the deflecting medium or the substrate material, I_0 the intensity of the incident pump beam in W/cm^2 , z_0 the distance between the sample surface and probe beam, and A the absorbance of the sample ($A = 1 - R - T$, neglecting scattering). There are only two unknown quantities z_0 and A . Therefore, a measurement is first necessary with a sample of known absorbance in order to determine z_0 . Once z_0 is known, the absorbance of other samples can be determined.

To calculate k from the measured absorbance A of the titania film, the expressions given by Bubbenzer and Koidl²⁵ were used. However, the film refractive index and thickness are also needed. These values were obtained from the reflectance and transmittance curves measured by Group B for the same films. Similar results for the k values were obtained with a program²⁶ which calculates the k value from the measured absorbance and refractive index. The calculated values of n and t agreed with those of Group B within the limits of the experimental error (somewhat larger than the errors of Group B). In the conversion of A to k , extreme accuracy is not needed in n and t .

C. Surface Roughness

Surface roughness was measured at two places on all films of Group B using the Talystep Surface Profiling Instrument²⁷ at the University of Alabama in Huntsville. The instrument had a diamond stylus with 1- μm radius of curvature; a 2-mg loading was used. Two different profile lengths were measured at each site: 1 mm (1000 μm) and 100 μm . The longer profile included roughness from both the titanium dioxide film and the commercially polished fused silica substrate, while the roughness on the shorter profile was primarily caused by the film. In both cases there were 2628 data points, with sampling distances of 0.38 μm and 0.038 μm , respectively. The lateral resolution of the 1- μm radius stylus was ~ 0.1 – $0.2 \mu\text{m}$ for this type of surface.

Autocovariance functions²⁸ were calculated from the profile data, and the autocovariance lengths determined. The autocovariance function is a measure of the correlation properties of the surface roughness. It is the product of two copies of the same surface profile as one is shifted relative to the other. The amount of lateral shift between the two profiles is the lag length. The autocovariance length is the value of the lag length at which the autocovariance function drops to $1/e$ (0.368) of its value at zero lag length. Very short autocovariance lengths, less than 0.5 μm , indicate that the granularity of the titanium dioxide film is the

dominating feature. Longer autocovariance lengths show that the substrate roughness is more important.

Power spectral density functions were calculated from the autocovariance functions.²⁹ These give the frequency spectrum of the surface roughness. Since the roughness appeared to be uniform over the film surface, the surface statistics were averages of measurements made at only two places on each film.

D. Microstructure

Film properties can be measured in a variety of ways to show film microstructure, degree of crystallinity, stress, adhesion to substrates, etc. In the titania film study, only a limited analysis of film structure was attempted, partly to avoid destructive measurement techniques, and partly because of limited time and availability of people to perform the specialized measurements.

An attempt was made to investigate film stress by placing the coated substrates between crossed polarizers, illuminated by an extended white light source, and looking for the characteristic cross-shaped pattern. Selected samples of Group B were tested as well as uncoated substrates. No evidence of stress could be observed on either the coated or uncoated substrates. Flatness of selected coated and uncoated substrates was measured in a Zygo interferometer at the University of Alabama in Huntsville to see if there was evidence of substrate curvature produced by stress in the titania films. The optical figure of the commercial grade uncoated substrates was several fringes from being flat

Table III. Measured Optical Constants of Titania Films at $\lambda = 550 \text{ nm}$

Type	Sample #		Refractive Index <i>n</i>			Extinction Coef. <i>k</i> (10 ⁻¹)			Inhomogeneity $\Delta n/n$	
	A	B	A	B	C*	A	B	C*	A	B
E-B	003	002	2.320	2.29		0	0		0.03	-0.02
	006	005	2.306	2.30		2	0		-0.05	-0.04
	201	202	2.30	2.40		20	20			-0.03
	025	023	2.362	2.36	2.38	3	9	30	**	**
	138	140	2.308	2.31	2.35	3	0	10	0	0.02
	052	052	2.205	2.21		1	3		0.04	0.03
	094	097	2.248	2.22	2.27	2	3	*	0	0.01
	036	038	2.360	2.36		7	4		0	-0.01
IAD	024	022	2.506	2.51	2.55	0	4	0.72	0	0.01
	137	139	2.433	2.43		0	0		0	-0.02
	143	144	2.425	2.43		10	0		0	0
	013	014	2.344	2.35		0	0		-0.04	-0.05
	011	012	2.461	2.44	2.47	7	6	14.5	-0.15	-0.15
IBSD	135	136	2.480	2.48	2.53	0	4	4.4	0	0.01
	078	079	2.417	2.45	5	5	14		0.03	0.02
	120	122	2.543	2.53	2.57	20	21	49	-0.07	0.08
ARE	057	057	2.198	2.18		0	5		0.03	0.03
RFS	093	145	2.530	2.49	2.46	**	22	23	**	0.05
IP	165	166	2.518	2.53	2.58	2	0	5.5	0	0.01
	114	115	2.611	2.61	2.65	15	10	10	0.08	0.09
Dip	213a	213b	2.212	2.19	2.21		12	5.9		

A. Measured and analyzed at Ecole Nationale Supérieure de Physique de Marseille, France.

B. Measured at OCLI, Santa Rosa, CA, analyzed at Martin Marietta Astronautics Group, Albuquerque, NM.

C. Measured and analyzed by A. Sauer at University of Alabama in Huntsville; AL and F.N.C.A. Rome, Italy.

C*. n was calculated from R and T measurements and interpolated to 514 nm. k was measured at 514 nm by photoacoustic deflection spectroscopy.

* Rectangular substrate did not fit in sample holder.

** Inhomogeneity prevented satisfactory measurement.

($\lambda = 633$ nm), and varied considerably from one substrate to another. Thus the surface flatness was not good enough to detect small changes produced by stress in the films.

Two measuring techniques were used with some success to investigate film microstructure. They are described below:

1. Contact Angle for Wetting

One way to determine the type of structure in titania films is to measure the contact angle for wetting. There are two possible structures for crystalline titania—anatase and rutile. The wetting properties of these materials are different, and are also different from the wetting of amorphous fused silica.²⁹ Wetting is governed by an interaction force at a solid-liquid interface, which is expressed by the Hamaker constant.²⁹ Anatase has a constant of 3.5×10^{-20} , while rutile has a constant of 8×10^{-20} ; these differ by a factor >2 . Further, silica has an intermediate constant, 6×10^{-20} . In order to see whether differences could be discerned between films prepared by different techniques, water drops were placed on the surfaces of Group B films and photographs were taken aiming the camera parallel to the film surface to show the drops in cross section. Contact angles were measured on the photographs. Differences were seen between films, and are reported in Sec. IV.

2. Raman Spectroscopy

A Raman microprobe was used to investigate the crystalline structure in the titania films. The two forms, anatase and rutile, have Raman scattering peaks at different frequencies, and thus are easily distinguishable. The primary anatase peak is at 143 cm^{-1} , while the rutile structure has peaks in the vicinity of 422 cm^{-1} and 595 cm^{-1} .³⁰ All the films in Group B were studied with the Raman microprobe at the University of Alabama in Huntsville. The instrument was

a Jobin Yvon Instruments S.A. MOLE U1000, with excitation by a Spectra-Physics Series 2020 argon ion laser. The focused spot on the surface was $\sim 5 \mu\text{m}$. Stokes transitions were measured on the long wavelength side of the exciting 514.5-nm argon line. No rutile was seen in any of the films, but anatase was observed, as reported in Sec. IV. Rutile has previously been found in laser annealed titania films³¹ and films subjected to laser damage.³⁰

IV. Results

A. Optical Constants

The values of the optical constants measured by Groups A and B using the techniques described in Sec. IIIA are given in Tables III and IV. Further information is shown in Figs. 7–11. Several interesting observations can be made about the values of the optical constants, and are discussed in this section.

First, in Table III are listed values of n , k , and $\Delta n/n$ for all films at a wavelength of 550 nm, as measured by Groups A and B, respectively. There is excellent

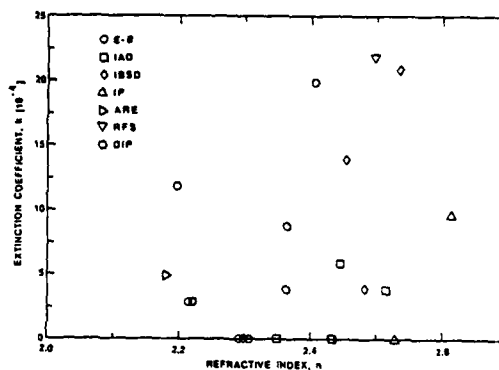


Fig. 7. Refractive index n vs extinction coefficient k for the films in Group B.

Table IV. Cauchy Constants [Eq. (10)] for the Refractive Indices of Films in the Wavelength Range 400–1000 nm Measured by Group A; the Wavelength is in μm

Type	Sample #	A	B (10^4)	C (10^7)
E-B	003	2.1883	2.440	4.640
	006	2.1868	1.772	5.539
	023	2.2935	0.787	8.839
	138	2.1758	2.348	4.980
	052	2.0898	2.389	3.554
	094	2.1222	2.353	4.342
IAD	036	2.1970	3.780	3.492
	024	2.3493	2.601	6.387
	022	2.3435	2.899	6.062
	137	2.2675	3.567	4.333
	143	2.2741	2.638	5.818
IBSD	013	2.2407	0.791	7.044
	011	2.4188	-2.367	11.03
	135	2.3154	3.148	5.513
ARE	078	2.2799	1.950	6.710
	120	2.3953	1.727	8.267
IP	157	2.0780	2.244	4.120
DIP	165	2.3683	2.114	7.225
	114	2.4629	1.542	8.886
	213	2.1886	-3.796	13.56

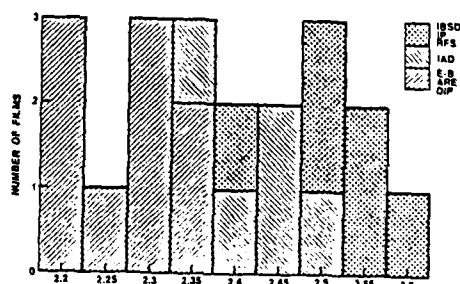


Fig. 8. Histogram showing the refractive indices of all films in Group A. The mean value of n was 2.30 for the E-B films, 2.43 for the IAD films, and 2.51 for the IBSD and IP films as compared to 2.39 for all films.

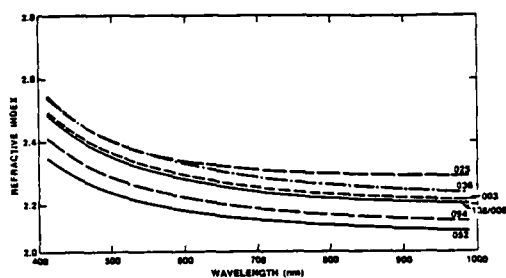


Fig. 9. Calculated refractive index vs wavelength of E-B deposited films measured by Group A.

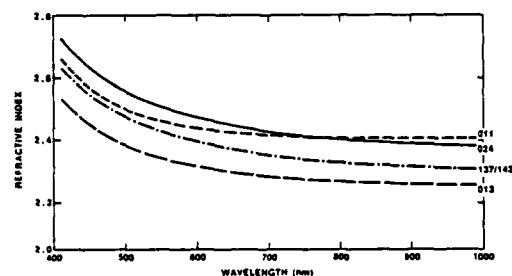


Fig. 10. Calculated refractive index vs wavelength for IAD films measured by Group A.

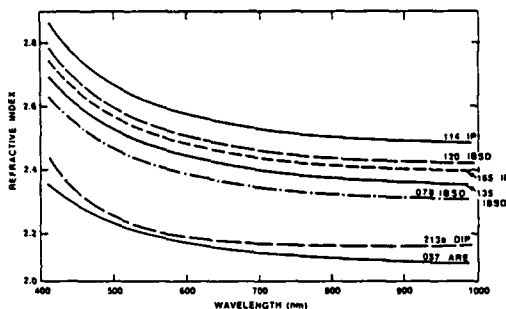


Fig. 11. Calculated refractive index vs wavelength for IBSD, IP, ARE and dip coated films measured by Group A.

agreement in the n values measured by each group on films prepared at the same time. This shows consistency in the film preparation, and that the two different measurement techniques were free of systematic errors. All the n values agreed within 0.03 except for two films which were observed to be nonuniform. The refractive indices of the films spanned a range from 2.18–2.61, indicating a large variation among the various films. Most of the films had very low k values at $\lambda = 550$ nm; in general the k values measured by Groups

A and B were in agreement. Small film inhomogeneities $\Delta n/n$ were measured in most cases, showing that the preparation techniques gave uniform, homogeneous films. Only two films were too inhomogeneous to yield a value of $\Delta n/n$, while a third had a large negative inhomogeneity, i.e., the film refractive index was highest at the film-substrate interface. The film prepared by dip coating was initially coated on both sides of a 1 in (25 mm) \times 6 in (152 mm) fused silica substrate. However, the film on one side was removed with a saturated solution of ammonium bifluoride. The part was then cut into two 1 in (25 mm) \times 3 in (76 mm) pieces; one of the pieces was sent to each group for measurement. The measurement of k and $\Delta n/n$ may have been complicated because the coating was composed of several layers, perhaps resulting in a nonuniform index.

In order to determine whether there was any relation between the optical constants and the method of film preparation, n is plotted vs k in Fig. 7 for all films in Group B. The n and k values for most of the E-B films cluster around the low end, while other deposition techniques yield films with higher n values and somewhat higher k values. The ARE and dip-coated films are exceptions; these had the lowest refractive indices of all. The dip coating was made from standard solutions used in making production multilayer antireflection coatings, and was intended to have a low refractive index. With other liquid precursor solutions dense, high refractive index films can also be made by dip coating.

Figure 8 shows a histogram of the refractive indices for all films measured by Group A. Again the E-B deposited films have the lowest n values, the IAD films have higher n values, and the IBSD, IP and RFS films have the highest n values.

Other quantities were also compared: n , k and Δn vs the temperature of the substrate during deposition, and n and k vs oxygen pressure. No correlation was seen between any of these quantities and the method of film preparation.

The wavelength dependence of the refractive index measured by Group A is given in the form of Cauchy constants in Table IV, and as curves of n vs λ for the different types of films in Figs. 9–11. The variation of n with λ was almost identical for all E-B films with the exception of film #036. All IAD films had similar wavelength dependences except for film #011. The IBSD and IP films not only had the highest refractive indices but also the highest short wavelength absorption. The wavelength dependence for ARE film #057 was quite similar to that for the E-B films. Dip coated film #213a had a unique wavelength dependence.

The wavelength dependence of k was also measured by both groups. In general k was largest at the shortest wavelengths. However, since the curves of k vs λ were quite variable, only two examples are shown (Figs. 4 and 5).

Table V lists the optical and physical film thicknesses obtained from the analysis of the reflectance and transmittance measurements. The optical thick-

Table V. Physical (d) and Optical (nd) Thicknesses of Titania Films at $\lambda = 550$ nm Obtained from the Measurements of Groups A and B; all Thicknesses Are in nm

Type	Sample #	A		B		
		d	nd	Sample #	d	nd
E-B	003	308	714	002	310	710
	006	315	727	005	314	722
	201	*	*	202	284	682
	025	345	814	023	350	826
	138	310	715	140	308	711
	052*	386	851	052*	384	849
	094	333	748	097	335	744
	036	299	706	038	300	708
	024	300	752	022	300	753
	137	283	688	139	281	683
IAD	143	267	647	144	265	644
	013	238	558	014	234	550
	011	314	773	012	311	759
	135	285	707	136	284	704
	078	209	505	079	215	772
IBSD	120	266	676	122	267	698
	ARE	057*	374	057*	374	815
RFS	093	-	-	145	269	670
	IP	165	272	166	273	691
Dip	114	261	681	115	262	684
	213a	288	637	213b	291	637
Average		298	708	300	715	

A: Measured and analyzed at Ecole Nationale Supérieure de Physique de Marseille, France
B: Measured at OCLI, Santa Rosa, CA; analyzed at Martin Marietta Astronautics Group, Albuquerque, NM

* Rectangular substrate did not fit in sample holder
* Samples 052 and 057 measured by Groups A and B

nesses nd are for $\lambda = 550$ nm rather than for the five quarter wave interference maximum wavelength, which varied around an average value of 570 nm. The excellent agreement between physical and optical thicknesses obtained on pairs of films prepared at the same time again validates the two analysis techniques, and shows that the pairs of films had nearly identical properties. In the only case where there is a large discrepancy between the two samples in a pair (IBSD films #078 and #079), colors were clearly evident on sample #078 indicating a nonuniform film thickness.

Figure 12 shows a histogram of the optical thicknesses for the films in Group A. Twelve films had optical thicknesses lying between 675 and 775 nm, 4 films had lower values and 3 had higher values. The average optical thickness for all films was 711 nm; the wavelengths for which the films had a $5\lambda/4$ optical thickness were not tabulated.

Physical film thicknesses could not be measured with a profiling instrument because the film edges were not sharp. In most cases colored rings showed that the film thickness was decreasing over a distance of several millimeters. It was also not possible to remove the film nondestructively from part of the substrate.

B. Absorption

The results of the direct absorption measurements using photothermal deflection spectroscopy are presented in Tables III (C^*) and VI. Since an argon laser $\lambda = 514$ nm was used to heat the film, the k values in Table III and the absorptance values in Table VI are

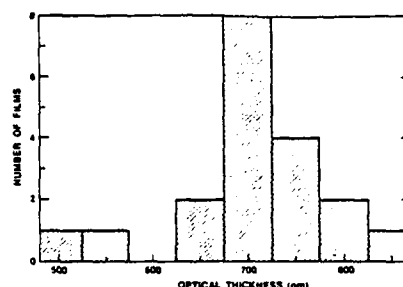


Fig. 12. Histogram of the optical thicknesses of the films in Group A, calculated at $\lambda = 550$ nm.

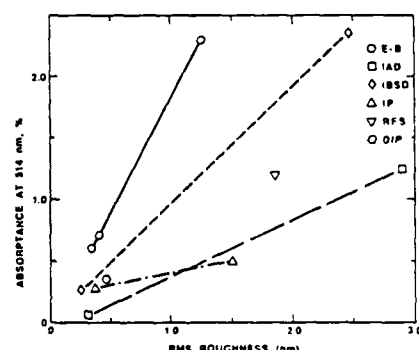


Fig. 13. Absorptance as measured by photothermal deflection spectroscopy vs rms roughness for selected films in Group B.

for that wavelength. However, the k values in Table III, column C^* are in reasonable agreement with those calculated by Groups A and B from spectrophotometric measurements. The two films having the highest k values from optical measurements (IBSD film #122 and RFS film #145) also have high k values calculated from photothermal deflection spectroscopy measurements. The agreement for E-B film #023, which also had a high measured absorptance, is not so good. Later measurements on other titania films made at several wavelengths indicate that there is a 20–50% decrease in k between 514–550 nm.

The relation between the surface roughness of some films and their absorption at $\lambda = 514$ nm is shown in Fig. 13. As discussed in Sec. IV.C, the short-profile-length roughness is characteristic of the film surface only. The plot of the film absorptance (as determined by photothermal deflection spectroscopy at 514 nm) vs the surface roughness of the 100- μ m profiles (from Table VI) shows clearly that the rougher films also have more absorption. Since only two films prepared by each technique were measured by photothermal deflection spectroscopy, it is not known whether there is a linear relation between surface roughness and ab-

sorption. However, it is clear that the dependence of absorption on surface roughness is different for the different types of films. The ion plated films show the least increase in absorption with increasing roughness. A possible explanation for these results is that there is an enhanced coupling of the pump light energy (at 514 nm) for the rougher surfaces because of enhanced scattering into the TiO_2 film. The different slopes for the different deposition techniques seem to be related to the microstructure of the films. The fairly porous columnar structure known for E-B films provides for an abundance of foreign adsorbates in the film, whereas the almost perfectly dense IP films prevent such intrinsic absorption, and these films stay clean.

Table VI. Measured Roughness, Correlation Length, and Absorbance of TiO_2 Films in Group B

Type	Sample#	Surface Roughness 100 μm Profile		Surface Roughness 1000 μm Profile		Absorbance ρ $\lambda = 514 \text{ nm}$
		$\delta(\text{nm})$	$\sigma(\mu\text{m})$	$\delta(\text{nm})$	$\sigma(\mu\text{m})$	
E-B	097	0.35	3.6	0.63	19.7	0.595
	140	0.41	4.1	0.68	26.6	
	038	0.51	1.2	0.68	27.7	2.3
	002	0.52	1.3	0.80	14.4	
	202	0.74	0.9	0.94	14.0	
	023	1.26	0.3	1.38	1.9	
IAD	005	1.60	0.3	1.42	1.3	0.0575
	022	0.32	3.4	0.46	23.5	
	139	0.36	2.6	0.60	22.4	
	144	0.41	2.5	0.91	23.5	
IBSD	014	0.90	0.2	1.03	17.1	1.25
	012	2.91	0.2	2.09	1.1	
	136	0.25	1.9	0.79	61.5	0.264
RFS	079	0.34	2.1	0.68	26.6	
	122	2.46	0.2	1.73	1.1	
IP	145	1.86	0.1	1.32	1.1	1.2
	166	0.37	3.0	0.67	32.7	
	115	1.51	0.2	1.07	1.1	
Dip	213b	0.47	4.1	0.82	35.3	0.335
Uncoated	126	0.28	3.1	0.63	41.4	

Roughness measured by J. M. Bennett at University of Alabama in Huntsville, AL

Absorbance measured by A. Saxer at University of Alabama in Huntsville, AL and ENEA, Rome, Italy

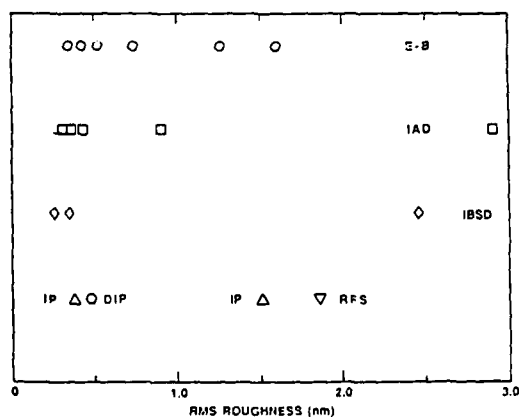


Fig. 14. Measured rms roughnesses of films in Group B.

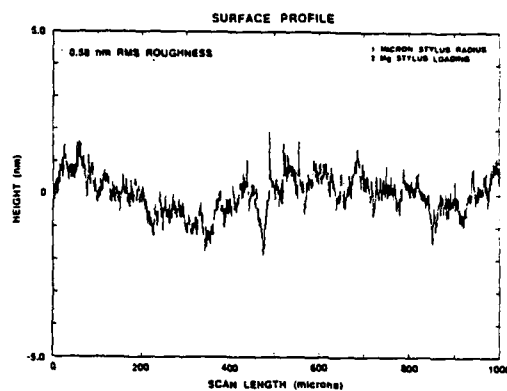


Fig. 15. Surface profile (1000- μm profile length) for a typical uncoated fused silica substrate in Group B.

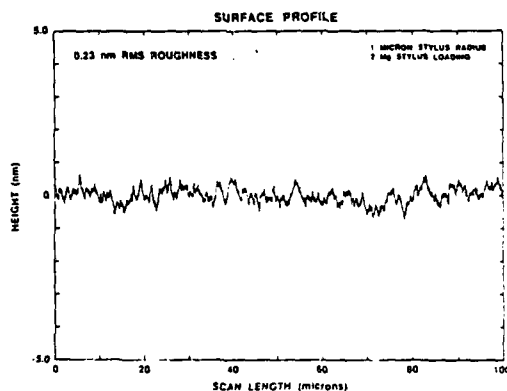


Fig. 16. Surface profile (100- μm profile length) for IBSD film #136.

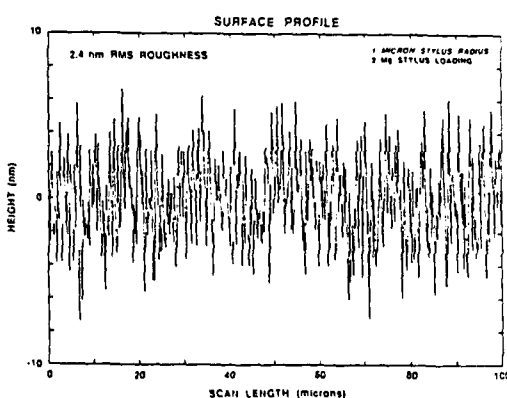


Fig. 17. Surface profile (100- μm profile length) for IBSD film #122.

C. Surface Roughness

The measured roughnesses and autocovariance lengths of the films in Group B are listed in Table VI. The films are in the order of increasing roughness. Roughness values for the 1000 μm profile length include both the substrate roughness and the added short spatial wavelength roughness of the titania films. Film roughness, when present, generally dominates in the 100- μm profiles. Film roughnesses (100- μm profile length) are shown for the different film types in Fig. 14. It is clear that no one type of film preparation method gives the smoothest films; smooth films (and also rougher ones) were produced by all methods.

Figures 15–21 show selected surface profiles, as well as autocovariance functions and power spectral density functions obtained from the profiles. A 1000- μm -long profile of one of the uncoated commercially polished fused quartz substrates is shown in Fig. 15. The roughness, 0.58 nm rms, is typical of the roughness values of the bare substrates which ranged from 0.4–0.8 nm rms; most were about 0.6–0.7 nm rms. Roughnesses for the 100- μm profile lengths were in the 0.2–0.4 nm rms range, with 0.3 nm rms being a typical value. These values are inferred from a careful examination of all the profiles.

In Figs. 16 and 17 profiles are shown for one of the smoother and one of the rougher films, both of which were made by ion beam sputter deposition. The profile of the smoother film is indistinguishable from that of a bare substrate, while the profile of the rougher film clearly shows the grain structure of the film.

The autocovariance functions for the same smoother and rougher films, Figs. 18 and 19, have very different characters, especially with regard to the initial shapes of the curves. Note that the autocovariance lengths differ by nearly 10 times. The short autocovariance length for the rougher film is typical of film granularity, while the longer autocovariance length for the smoother film is caused by the substrate roughness, with the film adding no additional structure.

Power spectral density functions for the same two films are shown in Figs. 20 and 21. A vertical arrow marks the spatial frequency corresponding to the autocovariance length of each film. The power spectral density function for the smoother film is indistinguishable from that of an uncoated substrate. It has a maximum contribution from the lowest spatial frequencies (long spatial wavelengths). The highest spatial frequencies are less than 10^{-4} of the maximum lowest spatial frequency. By contrast, the power spectral density function for the rougher film has contributions from a larger range of spatial frequencies with much less decrease for high spatial frequencies (short spatial wavelengths).

The range of spatial frequencies that would produce scattering in the visible spectral region for a He-Ne laser beam, $\lambda = 0.633$ nm, at normal incidence and scattering angles of 0.4° – 90° is shown by the horizontal double ended arrows in Figs. 20 and 21. It is clear that the rougher film should scatter much more than the

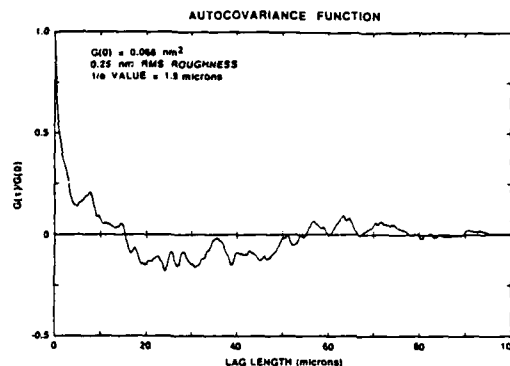


Fig. 18. Autocovariance function for IBSD film #136.

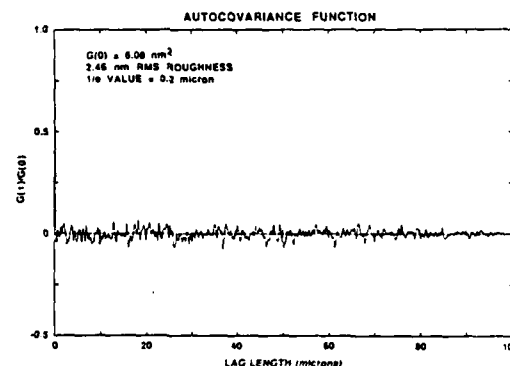


Fig. 19. Autocovariance function for IBSD film #122.

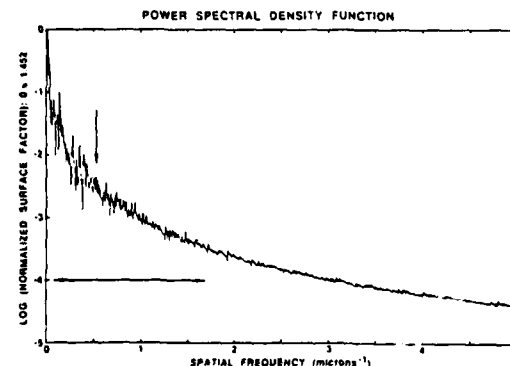


Fig. 20. Power spectral density function for IBSD film #136. The vertical arrow marks the spatial frequency corresponding to the autocovariance length. The horizontal double ended arrow marks the range of spatial frequencies that produce scattering into angles between 0.4° and 90° for a wavelength of 0.633 nm at normal incidence.

smoother one. Studies of angle resolved scattering of the Group A samples have been made by Group A. However, since their He-Ne laser spot size was ~ 4 mm in diameter, scattering from substrate defects dominated. The results of these measurements will be reported in a forthcoming paper.³²

D. Microstructure

The measured contact angles for wetting and film crystallinity as determined from Raman microprobe measurements are given in Table VII. The cosine of the wetting angle is plotted vs rms roughness in Fig. 22. (Films that contained anatase are indicated by the solid circles in the figure.) The cosines of the wetting angles divide approximately into two groups, those which are larger than that of an uncoated fused silica substrate and those which are smaller. (Large cosines correspond to small contact angles.) It is immediately obvious that there is no consistent relation between the method of film preparation and the contact wetting angle. Also, the film roughness is not correlated with the contact wetting angle.

Film crystallinity as measured by the Raman microprobe showed that some of the films contained anatase, but none contained rutile; most were amorphous. In Fig. 23 are shown Raman microprobe spectra for two IAD titania films; one had a large anatase peak and the other had none so is presumed to be amorphous. Only eight of the films in Group B showed any evidence of anatase, ranging from large peaks for E-B film #023 and IAD film #012, to medium peaks for E-B films #038, #202, and #005, and RFS film #145, and small peaks for IAD film #014 and dip-coated film #213b. As expected, the uncoated fused silica substrate showed no evidence of crystallinity.

There may, however, be a relationship between the contact wetting angle and the film crystallinity, as predicted by the Hamaker constant mentioned earlier. Five of the eight anatase-containing films had large contact wetting angles (small cosines); these included all the films whose roughnesses were 0.5 nm rms or greater except for IBSD film #122, which was rough but contained no trace of anatase. On the other hand, four of the seven films that had small contact wetting angles (large cosines) contained no anatase. Exceptions were E-B films #023 and #005 and dip-coated film #213b. Interestingly, half of the anatase-containing films were prepared by E-B evaporation. The relation between contact wetting angle and film crystallinity is by no means conclusive, but it appears that anatase-containing films are likely to have larger contact wetting angles (smaller cosines) than uncoated fused silica.

V. Conclusions

There were large variations in the properties of films produced by each technique. Film refractive index, absorption, roughness, contact angle for wetting, and crystallinity seemed to depend not only on the technique but also on the particular coating chamber and parameters used. However, some general conclusions

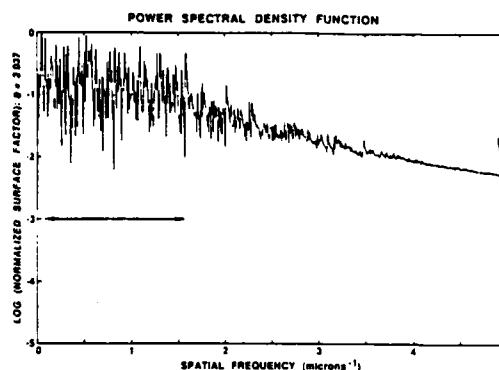


Fig. 21. Power spectral density function for IBSD film #122. The arrows have the same meanings as in Fig. 20.

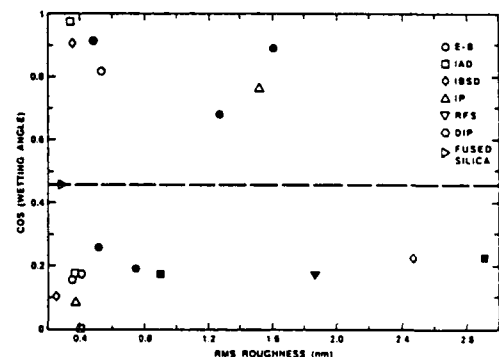


Fig. 22. Cosine of the contact angle for wetting vs rms surface roughness for the films in Group B and a bare fused silica substrate. The solid data points are for films containing anatase (see Table VII).

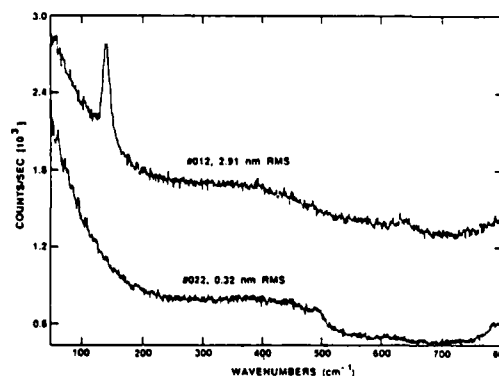


Fig. 23. Raman microprobe spectra for IAD films #012 and #022 in Group B. Note the anatase peak in the upper curve.

Table VII. Roughness, Contact Angle for Wetting, and Crystallinity of Titania Films in Group B

Type	Sample #	Surface Roughness	Contact Angle		Crystallinity
		100 μ m Profile			
		R(nm)	Deg	Cos	Anatase
E-B	097	0.35	81	0.156	
	140	0.41	80	0.174	
	038	0.51	75	0.259	M
	002	0.52	35	0.819	
	202	0.74	79	0.191	M
	023	1.26	47	0.682	L
IAD	005	1.60	27	0.891	M
	022	0.32	13	0.974	
	139	0.36	80	0.174	
	144	0.41	90	0	
	014	0.90	80	0.174	S
IBSD	012	2.91	77	0.223	L
	136	0.25	84	0.104	
	079	0.34	25	0.906	
	122	2.46	77	0.223	
RFS	145	1.86	80	0.174	M
IP	166	0.37	85	0.087	
	115	1.51	40	0.766	
Dip	213b	0.47	24	0.913	S
Uncoated	126	0.28	63	0.454	

Peak Heights: L = Large, M = Medium, S = Small

Roughness measured by J. M. Bennett at University of Alabama in Huntsville, AL

Contact angle for wetting measured by K. H. Guenther and Qibo Zhou at University of Alabama in Huntsville, AL

Film crystallinity measured by Raman microprobe by Boon Loo and David Burns at University of Alabama in Huntsville, AL

can be drawn: The refractive indices of the E-B films as a group were lowest, IAD films had intermediate refractive indices, and the IBSD and IP films had the highest indices (Figs. 8-10). The short wavelength refractive index was only slightly higher than at 550 nm for the E-B films; there were larger differences for the IAD, IBSD, and IP films. There was a partial correlation between film crystallinity and contact wetting angle in that nearly all of the films with large contact wetting angles also contained crystalline anatase (Fig. 22). Also, all but two of the films rougher than 0.6 nm rms contained anatase (Fig. 22).

If one defines the best films by some criterion, for example, those with the highest refractive index, lowest absorption, smallest inhomogeneity, or smoothest surface, there is no one technique that will consistently give this type of film. All techniques produced films with some excellent qualities, but best and worst films were produced by each technique.

Excellent agreement was obtained for values of optical constants and film thickness for the corresponding films measured by Groups A and B, indicating that there were minimum errors in the measurement techniques and a high degree of consistency between pairs of films prepared at the same time. In the few cases where agreement was not obtained between two films in a pair, the films had noticeable color variations across their surfaces, indicating nonuniform optical properties.

Finally, it should be emphasized that all films were provided at the request of the organizers of this study,

and were not company products or in any way representative of the best that a group could do. In some cases the films were the first of their kind produced by a group, and better ones have been made since. Many of the techniques used to produce the titania films are new, and much better films are expected to be produced in the future.

References

1. The acronyms used in this paper may vary from those used elsewhere.
2. P. J. Martin, "Review: Ion-based Methods for Optical Thin Film Deposition," *J. Mater. Sci.* 21, 1-25 (1986).
3. A. Matthews, "Developments in Ionization Assisted Processes," *J. Vac. Sci. Technol. A* 3, 2354-2363 (1985).
4. A. Kalb, "Neutral Ion Beam Sputter Deposition of High-Quality Optical Films," *Opt. News* 12, 13-17 (August 1986).
5. H. K. Pulker, M. Bühler, and R. Hora, "Optical Films Deposited by a Reactive Ion Plating Process," *Proc. Soc. Photo-Opt. Instrum. Eng.* 678, 110-114 (1987).
6. R. P. Howson, K. Suzuki, C. A. Bishop, and M. I. Ridge, "Reactive Ion Plating of TiO₂," *Vacuum* 34, 291-294 (1984).
7. H. Schroeder, "Oxide Layers Deposited from Organic Solutions," in *Physics of Thin Films*, Vol. 5, G. Hass and R. E. Thun, Eds., (Academic, New York, 1969), pp. 87-141.
8. J. P. Lehan, Optical Sciences Center, University of Arizona, private communication.
9. M. Kaspar and R. Pfeifferkorn, "Intermittent Ion Assisted Deposition of Silica and Titania," in *Technical Digest of Fourth Topical Meeting on Optical Interference Coatings* (Optical Society of America, Washington, DC, 1988), paper ThB12.

10. H. K. Pulker, G. Paesold, and E. Ritter, "Refractive Indices of TiO_2 Films Produced by Reactive Evaporation of Various Titanium-Oxygen Phases," *Appl. Opt.* 15, 2986-2991 (1976).
11. K. H. Guenther, "Microstructure of Vapor-Deposited Optical Coatings," *Appl. Opt.* 23, 3806-3816 (1984).
12. K. H. Guenther, H. L. Gruber, and H. K. Pulker, "Morphology and Light Scattering of Dielectric Multilayer Systems," *Thin Solid Films* 34, 363-367 (1976).
13. Karl Heinz Müller, "Monte Carlo Calculation for Structural Modifications in Ion-Assisted Thin Film Deposition Due to Thermal Spikes," *J. Vac. Sci. Technol. A* 4, 184-188 (1986); "Model for Ion-Assisted Thin-Film Densification," *J. Appl. Phys.* 59, 2803-2807 (1986); "Modelling Ion-Assisted Deposition of CeO_2 Films," *Appl. Phys. A* 40, 209-213 (1986).
14. Karl-Heinz Müller, "Ion-Beam-Induced Epitaxial Vapor-Phase Growth: A Molecular-Dynamics Study," *Phys. Rev. B* 35, 7906-7913 (1987).
15. W. T. Pawlewicz, P. M. Martin, D. D. Hays, and I. B. Mann, "Recent Developments in Reactively Sputtered Optical Thin Films," in *Proc. Soc. Photo-Opt. Instrum. Eng.*, R. I. Seddon, Ed., 325, 105-116 (1982); W. T. Pawlewicz, D. D. Hays, and P. M. Martin, "High-Band-Gap Optical Coatings for 0.25 and 1.06 Micron Fusion Lasers," *Thin Solid Films* 73, 169-175 (1980).
16. D. P. Arndt et al., "Multiple Determination of the Optical Constants of Thin-Film Coating Materials," *Appl. Opt.* 23, 3571-3596 (1984).
17. J. P. Borgogno, B. Lazarides, and E. Pelletier, "Automatic Determination of the Optical Constants of Inhomogeneous Thin Films," *Appl. Opt.* 21, 4020-4029 (1982).
18. J. P. Borgogno, B. Lazarides, and P. Roche, "An Improved Method for the Determination of the Extinction Coefficient of Thin Film Materials," *Thin Solid Films* 102, 209-220 (1983).
19. E. Pelletier, P. Roche, and B. Vidal, "Détermination Automatique des Constantes Optiques et de l'Épaisseur de Couches Minces: Application aux Couches Diélectriques," *Nouv. Rev. Opt.* 7, 353-362 (1976).
20. The first R_s in Eq. (4) is the reflectance from the air side, while the second R_s is the reflectance from the inside. However, if k for the film is small, these reflectances are essentially equal.
21. A. S. Valeev, "Determination of the Optical Constants of Weakly Absorbing Thin Films," *Opt. Spectrosc. USSR* 15, 269-274 (1963).
22. A. S. Valeev, "On a Technique for the Determination of the Optical Constants of Thin Weakly Absorbing Layers," *Opt. Spectrosc. USSR* 18, 498-500 (1965).
23. A. Savitzky and M. J. E. Golay, "Smoothing and Differentiation of Data by Simplified Least Squares Procedures," *Anal. Chem.* 36, 1627-1638 (1964).
24. W. B. Jackson, N. M. Amer, A. C. Boccara, and D. Fournier, "Photothermal Deflection Spectroscopy and Detection," *Appl. Opt.* 20, 1333-1344 (1981).
25. A. Bubenzer and P. Koidl, "Exact Expressions for Calculating Thin-Film Absorption Coefficients from Laser Calorimetric Data," *Appl. Opt.* 23, 2886-2891 (1984).
26. Thin film program written by Angela Piegari at ENEA, Rome, Italy, and based on the methods for determining n and k summarized in the paper by G. Emiliani, E. Masetti, and A. Piegari, "Thin film Refractive Index Determination by Different Techniques," *Proc. Soc. Photo-Opt. Instrum. Eng.*, R. Jacobsson, Ed., 652, 153-157 (1986).
27. J. M. Bennett and J. H. Dancy, "Stylus Profiling Instrument for Measuring Statistical Properties of Smooth Optical Surfaces," *Appl. Opt.* 20, 1785-1802 (1981).
28. J. M. Elson and J. M. Bennett, "Relation Between the Angular Dependence of Scattering and the Statistical Properties of Optical Surfaces," *J. Opt. Soc. Am.* 69, 31-47 (1979).
29. M. J. Jaycock and G. D. Parfitt, *Chemistry of Interfaces* (Wiley, New York, 1981), pp. 11-21; data are taken from F. M. Fowkes, "Attractive Forces at Interfaces," *Ind. Eng. Chem.* 56, 40-52 (1964).
30. D. M. Friedrich and G. J. Exarhos, "Raman Microprobe of Laser-Induced Surface Damage Regions in TiO_2 Coatings," in *Laser Induced Damage in Optical Materials: 1985*, NBS Special Publication 746 (National Bureau of Standards, Washington, D.C., 1988), pp. 374-382.
31. L. S. Hsu, R. Solanki, G. J. Collins, and C. Y. She, "Raman Study of Structural Transformations of Titania Coatings Induced by Laser Annealing," *Appl. Phys. Lett.* 45, 1065-1067 (1984).
32. C. Hickey, C. Amra, and E. Pelletier, "Scattering Study of Single Layer Titania Films," in *Technical Digest, Fourth Topical Meeting on Optical Interference Coatings* (Optical Society of America, Washington, DC, 1988).

The authors would like to thank the people who have provided titania films for the study. Their names and organizations are listed in Table I. In addition they would like to thank Boon Loo and David Burns of the Chemistry Department, University of Alabama in Huntsville (UAH) for making the Raman microprobe measurements, and Qibo Zhou of the Physics Department, UAH, for assisting with the contact wetting angle measurements. Also, S. Mohan wishes to thank E. S. Rajagopal, Chairman, Instrumentation and Services Unit, Indian Institute of Science, Bangalore, India, for his keen interest in this work.